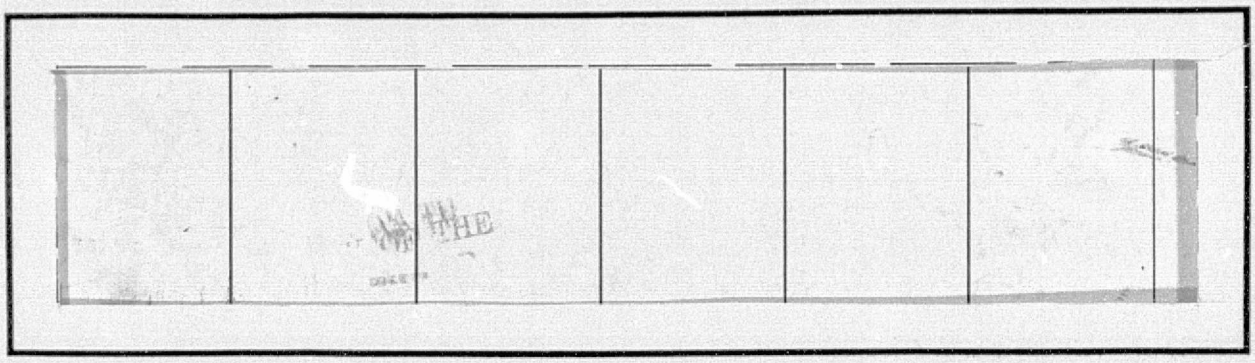

(NASA-CR-147662) CARRIER AND SYMBOL SYNCHRONIZATION SYSTEM PERFORMANCE STUDY (LinCom Corp., Pasadena, Calif.) 98 p HC $5.00 CSCL 17B

N76-22423

Unclas
G3/32 26893

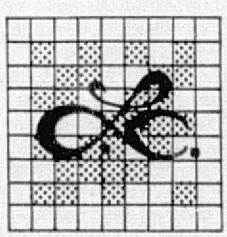

LinCom Corporation
P.O. Box 2793D, Pasadena, Calif. 91105

LinCom

CARRIER AND SYMBOL SYNCHRONIZATION SYSTEM

PERFORMANCE STUDY

Prepared for

LYNDON B. JOHNSON SPACE CENTER
HOUSTON, TEXAS 77058

Technical Monitor: Dr. Bart Batson
Prepared Under Contract No. NAS 9-14730

By

William C. Lindsey
LINCOM CORPORATION
P.O. Box 2793D
PASADENA, CA 91105

April 1976

TR-No. 04-7508-9

LinCom

ACKNOWLEDGEMENT

The author wishes to thank Dr. Bart Batson for his support and for participating in various technical discussions during the contract period.

TABLE OF CONTENTS

TABLE OF CONTENTS (Cont'd)

SUMMARY

This report develops results pertinent to predicting the performance of convolutionally encoded binary phase-shift keyed communication links. The details of the development are provided in four sections. These sections are concerned with developing the bit error probability performance degradations due to PN despreading by a time-shared delay locked loop, the Costas demodulation process, symbol synchronization effects and cycle slipping phenomena in the Costas loop. In addition, Costas cycle slipping probabilities are studied as functions of Doppler count time and signal-to-noise conditions. The effect of cycle slipping in the symbol synchronizer is also studied as a function of channel Doppler and other frequency uncertainties.

Section one develops the model of a suppressed carrier tracking, spread spectrum receiver/transponder in which the received signal is a convolutional/Manchester encoded binary data stream that is spread by a PN code to produce a binary phase-shift keyed (BPSK) carrier. The combined signal-to-noise degradations of the PN despreader's time-shared delay locked loop and the Costas phase-locked loop are developed as functions of the various system parameters and channel conditions. In addition, the theory of cycle slipping in the Costas loop is developed in terms of the channel Doppler dynamics, the additive noise, the minimum squaring loss, the PN code tracking loop jitter and the duration of the Doppler count normalized by the link data rate. Cycle slipping probabilities are developed as functions of the energy-per-bit to noise ratio, the number of cycle slips, the Doppler count time normalized by the link data rate and the receiver's static phase error. Various cycle slipping probabilities are

graphically demonstrated as a function of the Doppler count time.

Section two develops the bit error probability expression that results from the noisy reference loss due to jitter in the PN despreader's time-shared delay-locked loop and the noisy reference generated by the Costas demodulator. For the K=7 rate one-third convolutional code, bit error probability curves are graphically displayed as functions of the data rate, static phase error and energy-per-bit to noise ratio. Link performance degradations are easily assessed from the curves; in addition, any known losses due to filtering of the signals in the receiver can be easily added to the loss indicated by the curves presented.

Section three of this report is concerned with symbol synchronization in the Network Signal Processor when Manchester coding is used. New and fundamental results pertaining to symbol synchronization for Manchester coded messages are derived. The symbol synchronizer structures are found to be functions of the signal-to-noise ratio and data transition density. The minimum rms symbol sync jitter is determined, computed and comparisons are made for various phase detector characteristics. A general theory for cycle slipping in symbol synchronizers is given; it is shown that under most cases of interest, the effect of slipping in the symbol synchronizer does not give rise to a significant performance degradation. This section is also used to study the effects of synchronizer stress (due to clock uncertainties and channel Doppler) on bit error probability performance.

Section four of this report evaluates the degradations on bit error probability performance due to the noisy clock reference created by the symbol synchronizer. Particular graphical results are presented for the special case of a K=7 rate one-third convolutional code. The effects of data transition density

on symbol synchronizer/decoder performance is also studied and graphical results for cases of greatest interest are presented.

1.0 SUPPRESSED CARRIER TRACKING FOR SPREAD SPECTRUM RECEIVERS OF MANCHESTER CODED MODULATION

1.1 Introduction

Various communication systems transmit information in the form $s(t) = \sqrt{2S}\, m(t)s_{PN}(t)\sin[\omega_0 t + \theta(t)]$ where $s_{PN}(t)$ is a PN modulation and $m(t)$ is a linear modulation (coded or uncoded) which possesses no dc component in its power spectrum. Since no residual spectral component exists at the carrier frequency ω_0, it is not possible to use the conventional phase-locked loop for establishing the required coherent reference.

A number of methods have been proposed for generating a reference carrier from the received waveform which contains a suppressed carrier signal component. Of these, the three most popular are the squaring loop method (Refs. 1-5), the Costas loop method (Refs. 1, 2, 4-6), which is theoretically equivalent to the squaring loop, and the decision-directed feedback loop (Refs. 1, 2, 7-9) which first estimates the modulation, and then uses this estimate to eliminate the modulation from the carrier, leaving, as nearly as possible, an unmodulated sinusoid which can be tracked with a phase-locked loop. Each of these methods has advantages and disadvantages (practical or otherwise) with respect to the other two. What ultimately determines which method is used in a particular application is a tradeoff between the requirements on performance capability and the ease and cost of implementation.

As is well-known from previously published documents (Refs. 10-12) suppressed carrier modulation is employed on both the TDRSS-to-Orbiter (Forward) and Orbiter-to-TDRSS (Return) S-band links. In the case of the forward link, the convolutionally encoded, time-division multiplexed (TDM) data sequence is

converted from NRZ-L to Bi-phase-L format, modulo-2 added to a PN NRZ-L code sequence, and the resulting spread-spectrum sequence used to biphase modulate the transmitted carrier. After transmission through the TDRSS, the Orbiter receiver first despreads the signal by acquiring and tracking the PN code. Following this procedure, the baseband data symbol sequence is restored by demodulating the suppressed carrier signal with a Costas loop. In the return link, similar carrier modulation and demodulation processes take place with the exception that the signal is neither PN spread nor despread.

It is clear from the above that in order to assess the degrading effects of the carrier regeneration process on the overall system performance (including the average error probability performance of the data decoder), a thorough understanding of the acquisition and tracking performance of Costas loops and their optimum design for use in the Shuttle relay link environment is required.

1.2 Performance Analysis of the Costas Loop in the Suppressed Carrier Mode - Effect of Spread Spectrum Modulation

1.2.1 Motivation

The tracking performance of a Costas loop in response to a biphase modulated suppressed carrier input is well-documented in the literature (Refs. 1, 2, 4-6). All of these analysis have assumed that the in-phase and quadrature arm filters have sufficiently wide bandwidths so as to pass the data modulation undistorted. In practice, the bandwidths of these filters are more commonly chosen on the order of the data rate and thus the above assumption is strictly speaking invalid. In Refs. 13 and 14, the effect of arm filter distortion has been studied in detail,

graphically demonstrated, and compared with the results given in the literature which have neglected this important effect. In fact, careful control of the distortion term in any design gives rise to the highest noise immunity achievable with passive arm filters. Even these analyses, however, have not included the degrading effect of a spread spectrum modulation on the signal being tracked.

It is the purpose of this section to augment the previous work on Costas loops by including the effect of a PN spread spectrum modulation on tracking performance. The approach will parallel the development taken in Ref. 13 and thus much of the detail given there will be omitted in the presentation here. Finally, the results obtained will be adapted to cover the case where the Manchester coded data is also convolutionally encoded.

1.2.2 Costas Loop Model and Analysis

Consider the transponder illustrated in Fig. 1-1 where the Costas loop portion is enclosed within the dashed outline. Since our main interest here is in the performance of the Costas loop itself, it is sufficient for us to model the signal at its input and concentrate on how the loop processes this signal. Referring to Fig. 1-1, if the received signal $x_1(t)$ at point ① is modeled as

$$x_1(t) = \sqrt{2S}\, s_{PN}(t)m(t) \sin \Phi(t) + n_i(t) \tag{1}$$

then, using straightforward trigonometric manipulations, one finds that the signal at the input to the Costas loop (point ④) is given by

$$x_4(t) = K_e s_{PN}(t+\tau_e)\{\sqrt{2S}\, s_{PN}(t)m(t)\sin\left[\Phi(t) - \frac{M+1}{M}\Phi(t)\right] + n_4(t)\} \tag{2}$$

In Eq. (1), $\Phi(t) \triangleq \omega_0 t + \theta(t)$ with ω_0 the radian carrier frequency

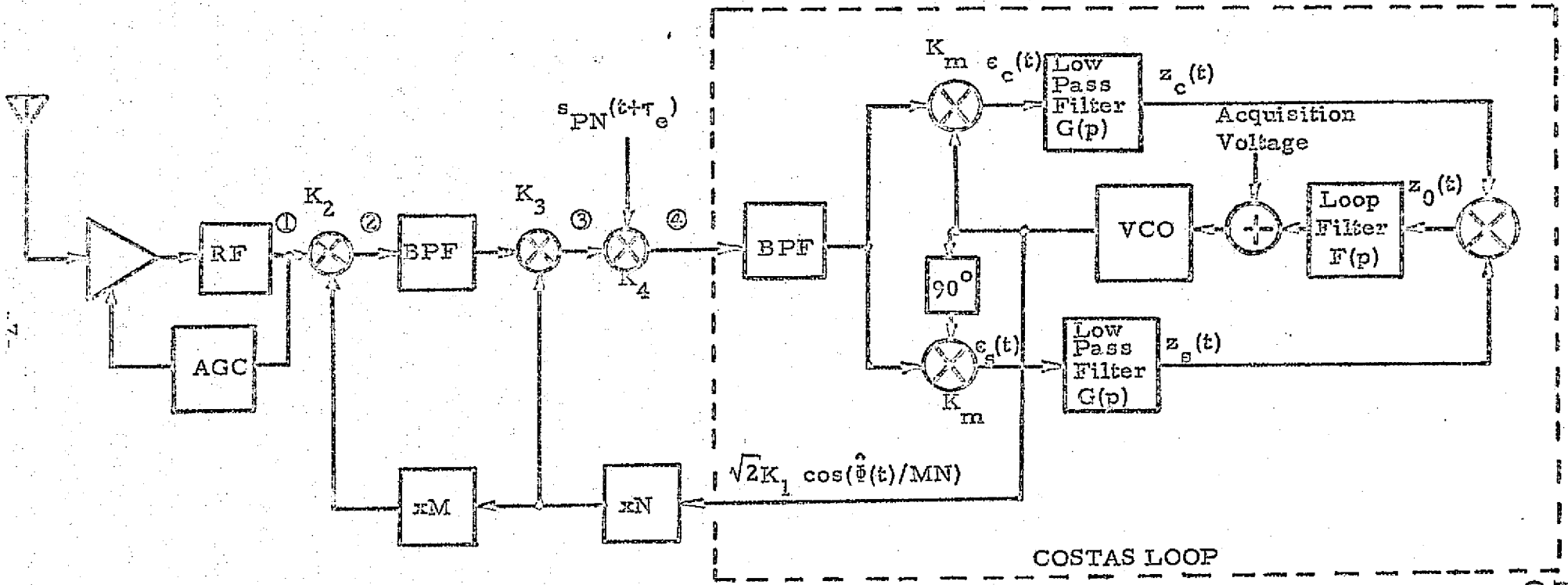

FIGURE 1-1. TRANSPONDER/COSTAS LOOP BLOCK DIAGRAM.

and $\theta(t) \triangleq \Omega_0 t + \theta_0$ the input phase to be estimated, $m(t)$ is the data modulation (a ± 1 digital waveform), $s_{PN}(t)$ is the received PN modulation, and $n_i(t)$ is the additive channel noise which can be expressed in the form of a narrowband process about the actual frequency of the input observed data, i.e.,

$$n_i(t) = \sqrt{2}\{N_c(t)\cos\bar{\Phi}(t) - N_s(t)\sin\bar{\Phi}(t)\} \tag{3}$$

where $N_c(t)$ and $N_s(t)$ are approximately statistically independent, stationary, white Gaussian noise processes with single-sided noise spectral density N_0 w/Hz (see Ref. 2) and two-sided bandwidth $B_0 < \omega_0/2\pi$. In Eq. (2), $s_{PN}(t+\tau_e)$ is the PN reference signal derived from the PN tracking loop, $K_e = K_1^2 K_2 K_3 K_4/2$ is an equivalent loop gain, and

$$n_4(t) = \sqrt{2}\left\{N_c(t)\cos\left[\bar{\Phi}(t) - \frac{M+1}{M}\hat{\bar{\Phi}}(t)\right] - N_s(t)\sin\left[\bar{\Phi}(t) - \frac{M+1}{M}\hat{\bar{\Phi}}(t)\right]\right\} \tag{4}$$

Also assumed in Eq. (2) is that the bandpass filter which precedes the Costas loop is sufficiently wide as to pass the data modulation $m(t)$ undistorted. Denoting the in-phase and quadrature detector (multiplier) gains by K_m, then the output $\epsilon_c(t)$ of the quadrature phase detector is (ignoring second harmonic terms)

$$\epsilon_c(t) = K_m x_4(t)\sqrt{2}K_1 \cos\frac{\hat{\bar{\Phi}}(t)}{MN} = K_e K_1 K_m\left[\sqrt{S}R_{PN}(\tau_e)m(t) - N_s'(t)\right]\sin\varphi(t)$$
$$+ K_e K_1 K_m N_c'(t)\cos\varphi(t) \tag{5}$$

while the in-phase arm phase detector output is

$$\epsilon_s(t) = K_m x_4(t)\sqrt{2}K_1 \sin\frac{\hat{\bar{\Phi}}(t)}{MN} = K_e K_1 K_m\left[\sqrt{S}R_{PN}(\tau_e)m(t) - N_s'(t)\right]\cos\varphi(t)$$
$$- K_e K_1 K_m N_c'(t)\sin\varphi(t) \tag{6}$$

where $\varphi(t) \triangleq \theta(t) - \frac{(M+1)N+1}{MN}\hat{\theta}(t)$ is the loop phase error, $R_{PN}(\tau_e) \triangleq s_{PN}(t)s_{PN}(t+\tau_e)$ is the autocorrelation function of the PN process which is approximately given by

$$R_{PN}(\tau_e) = \begin{cases} 1 - \dfrac{|\tau_e|}{\Delta}\,; & |\tau_e| \le \Delta \\ 0\,; & \text{elsewhere} \end{cases} \tag{7}$$

where Δ denotes the PN chip interval, and $N_c'(t)$ and $N_s'(t)$ are equivalent noise processes defined by

$$\begin{aligned} N_c'(t) &= s_{PN}(t+\tau_e)N_c(t) \\ N_s'(t) &= s_{PN}(t+\tau_e)N_s(t) \end{aligned} \tag{8}$$

In writing Eqs. (5) and (6), we have again assumed that the data modulation is passed undistorted by the bandpass filter following point ④ . Furthermore, we have assumed (and less justifiably) that this filter has no effect on the PN autocorrelation function. In practice, the autocorrelation function of (7) is somewhat spread by this filter and furthermore, the noise processes in (8) should reflect the filtering effect on the PN demodulation signal $s_{PN}(t+\tau_e)$. Without producing undue complexity into the analysis, we shall, to a first order approximation, ignore these effects.

After low-pass filtering with the in-phase and quadrature-phase arm filters, the phase detector output signals become, respectively,

$$z_c(t) = K_e K_1 K_m \Big[\sqrt{S}\,R_{PN}(\tau_e)\overbrace{G(p)m(t)}^{\hat{m}(t)} - \overbrace{G(p)N_s'(t)}^{N_s''(t)}\Big]\sin\varphi(t) + K_e K_1 K_m \overbrace{\big[G(p)N_c'(t)\big]}^{N_c''(t)}\cos\varphi(t) \tag{9}$$

$$z_s(t) = K_e K_1 K_m \left[\sqrt{S}\, R_{PN}(\tau_e)\overbrace{G(p)m(t)}^{\hat{m}(t)} - \overbrace{G(p)N_s'(t)}^{N_s''(t)}\right]\cos\varphi(t)$$

$$- K_e K_1 K_m \overbrace{\left[G(p)N_c'(t)\right]}^{N_c''(t)}\sin\varphi(t) \qquad (10)$$

Here the signal $\hat{m}(t)$ denotes the signal emerging from passage of the data modulation $m(t)$ through the low-pass arm filter $G(p)$, and likewise $N_c''(t)$ and $N_s''(t)$ are the equivalently filtered versions of $N_c'(t)$ and $N_s'(t)$, respectively. Multiplying the two low-pass filter outputs (assuming this multiplier has unit gain) gives the dynamic error signal

$$z_0(t) = z_c(t)z_s(t) = \frac{K_e^2 K_1^2 K_m^2}{2}\left\{\left[\sqrt{S}\, R_{PN}(\tau_e)\hat{m}(t) - N_s''(t)\right]^2 - N_c''^2(t)\right\}\sin 2\varphi(t)$$

$$+ K_e^2 K_1^2 K_m^2 N_c''(t)\left[\sqrt{S}\, R_{PN}(\tau_e)\hat{m}(t) - N_s''(t)\right]\cos 2\varphi(t) \qquad (11)$$

The instantaneous frequency of the VCO output is related to $z_0(t)$ by

$$\frac{d\hat{\phi}(t)}{dt} = K_V\left[F(p)z_0(t)\right] + \omega_0 \qquad (12)$$

and hence the stochastic integro-differential equation of operation of the Costas loop becomes

$$2\frac{d\varphi(t)}{dt} = 2\Omega_0 - KF(p)\left\{SR_{PN}^2(\tau_e)\hat{m}^2(t)\sin 2\varphi(t) + v_2\left[t, 2\varphi(t)\right]\right\} \qquad (13)$$

where $K \triangleq K_e^2 K_1^2 K_m^2 K_V$, and

$$v_2\left[t, 2\varphi(t)\right] \triangleq \left[-N_c''^2(t) + N_s''^2(t) - 2\sqrt{S}\, R_{PN}(\tau_e)\hat{m}(t)N_s''(t)\right]\sin 2\varphi(t)$$

$$+ \left[2\sqrt{S}\, R_{PN}(\tau_e)\hat{m}(t)N_c''(t) - 2N_c''(t)N_s''(t)\right]\cos 2\varphi(t) \qquad (14)$$

In arriving at (14), we have made the practical assumption that

the data rate $\mathcal{R}_s \triangleq 1/T_s$ is large relative to the equivalent loop bandwidth W_L, and thus $\hat{m}^2(t)$ can be replaced by its mean-squared value, i.e.,

$$\overline{\hat{m}^2(t)} \triangleq \int_{-\infty}^{\infty} S_m(f)\,|G(j2\pi f)|^2 df \tag{15}$$

with $S_m(f)$ denoting the power spectral density of the data modulation $m(t)$.

1.3 Steady-State Tracking Performance

Using Fokker-Planck techniques, the steady-state probability density function (p.d.f.) $p(2\phi)$ of the modulo 2π reduced phase error 2ϕ can be determined from (13). Assuming a loop filter of the form

$$F(s) = \frac{1+s\tau_2}{1+s\tau_1} \quad ; \qquad F_1 = \frac{\tau_2}{\tau_1} \tag{16}$$

then, (Ref. 1, Chap. 2 and Ref. 2, Chaps. 9, 10)

$$p(2\phi) = C_0 \exp(\beta 2\phi + \alpha \cos 2\phi) \int_{2\phi}^{2\phi+2\pi} \exp(-\beta 2x - \alpha \cos 2x)dx \tag{17}$$

where C_0 is a normalization constant and

$$\alpha = \left(\frac{r+1}{r}\right)\rho' - \frac{1-F_1}{r\sigma_G^2}$$

$$\beta = \left(\frac{r+1}{r}\right)^2 \frac{\rho'}{2W_L}\left[2\Omega_0 - SR_{PN}^2(\tau_e)\overline{\hat{m}^2(t)}K(1-F_1)\overline{\sin 2\phi}\right] + \alpha\,\overline{\sin 2\phi} \tag{18}$$

with

r = second order loop damping parameter $= SR_{PN}^2(\tau_e)\overline{\hat{m}^2(t)}KF_1\tau_2$
$= 4\zeta^2$

ζ = loop damping

ρ' = effective signal-to-noise ratio in the loop bandwidth = $(\rho/4)\mathscr{L}_L$

ρ = equivalent signal-to-noise ratio in the loop bandwidth of second-order PLL = $2SR_{PN}^2(\tau_e)/N_0W_L$

$\sigma_G^2 = \overline{\sin^2 2\phi} - (\overline{\sin 2\phi})^2$

$$= \text{loop squaring loss} \triangleq \frac{4SN_0(\overline{\hat{m}^2(t)})^2R_{PN}^2(\tau_e)}{N_{sq}}$$

$$N_{sq} \triangleq 2\int_{-\infty}^{\infty} R_{v_2}(\tau)d\tau \tag{19}$$

and

$$R_{v_2}(\tau) \triangleq \overline{v_2(t, 2\phi)v_2(t+\tau, 2\phi)} = 4[SR_{PN}^2(\tau_e)R_{\hat{m}}(\tau)R_{N_c''}(\tau)+R_{N_c''}^2(\tau)] \tag{20}$$

where

$$R_{N_c''}(\tau) \triangleq \overline{N_c''(t)N_c''(t+\tau)} = \frac{N_0}{2}\int_{-\infty}^{\infty} |G(j2\pi f)|^2 e^{j2\pi f\tau}df \tag{21}$$

and

$$R_{\hat{m}}(\tau) = \overline{\hat{m}(t)\hat{m}(t+\tau)} = \int_{-\infty}^{\infty} S_m(f)|G(j2\pi f)|^2 e^{j2\pi f\tau}df \tag{22}$$

In arriving at (20) we have made use of the previous assumption that the arm filters are narrowband relative to the input bandpass (IF) filter. The probability density function in (17) will be useful in what follows.

The squaring loss $\mathscr{L}_L$ can be derived in terms of basic system parameters. Substituting (21) and (22) into (20) and using the definition of $\mathscr{L}_L$ in (19) gives, after considerable manipulation, the squaring loss formula

$$\rho_L = \frac{D_m}{K_D + K_L \dfrac{B_i/R_s}{2R_s' D_m}} \tag{23}$$

where we have used $D_m \triangleq \hat{m}^2(t)$ to denote the modulation distortion factor, $R_s' = SR_{PN}^2(\tau_e)T_s/N_0 = R_s R_{PN}^2(\tau_e)$ is the effective data (symbol) signal-to-noise ratio, B_i denotes the two-sided noise bandwidth of the arm filter $G(j2\pi f)$, i.e.,

$$B_i \triangleq \int_{-\infty}^{\infty} |G(j2\pi f)|^2 df \tag{24}$$

K_L is a constant dependent only on the filter type and is defined by

$$K_L \triangleq \frac{\int_{-\infty}^{\infty} |G(j2\pi f)|^4 df}{\int_{-\infty}^{\infty} |G(j- \quad |^2 df} \tag{25}$$

and K_D is a constant dependent on both the baseband data power spectrum and the filter type, i.e.

$$K_D \triangleq \frac{\int_{-\infty}^{\infty} S_m(f)|G(j2\pi f)|^4 df}{\int_{-\infty}^{\infty} S_m(f)|G(j2\pi f)|^2 df} \tag{26}$$

Typical values of K_L for well-known filter types may be found in Table 2-1 of Ref. 1, Chap. 2. For example, $K_L = 1$ for an ideal low-pass filter while $K_L = (2n-1)/2n$ for an n-pole Butterworth filter. Since, via Eqs. (15) and (26), the modulation distortion factor D_m and the constant K_D respectively depend on the baseband data power spectrum $S_m(f)$, the format of the baseband data encoding must be specified before these quantities can be

computed. The case of interest here is when the modulation m(t) is a Manchester coding of equiprobable, independent transmitted symbols. The power spectral density $S_m(f)$ for such a data modulation is, Ref. 1, Chap. 2,

$$\frac{S_m(f)}{T_s} = \frac{\sin^4(\pi f T_s/2)}{(\pi f T_s/2)^2} \tag{27}$$

Recalling that an n-pole Butterworth filter is characterized by the transfer function

$$|G(j2\pi f)|^2 = \frac{1}{1+(f/f_c)^{2n}} \tag{28}$$

where f_c, the 3 dB bandwidth, is related to the two-sided noise bandwidth B_i of the filter by

$$f_c = \frac{nB_i}{\pi} \sin\left(\frac{\pi}{2n}\right) \tag{29}$$

then, substituting (27) and (28) into (15), (25), and (26), the modulation distortion factor D_m and constants K_L and K_D can be computed by numerical integration as functions of the ratio B_i/R_s. Using these results, Fig. 1-2 illustrates the squaring loss ρ_L vs B_i/R_s with R_s' as a parameter for a two-pole Butterworth filter, i.e., n = 2. We observe that for a fixed R_s' there exists an optimum noise bandwidth B_i for the arm filters in the sense of minimizing the squaring loss. These values of optimum arm filter bandwidth occur in the vicinity of the Nyquist bandwidth.

In designing carrier tracking loops, the most commonly used measure of performance is mean-squared tracking jitter. This quantity is ordinarily defined as the variance of the probability density function of the loop's modulo 2π reduced error

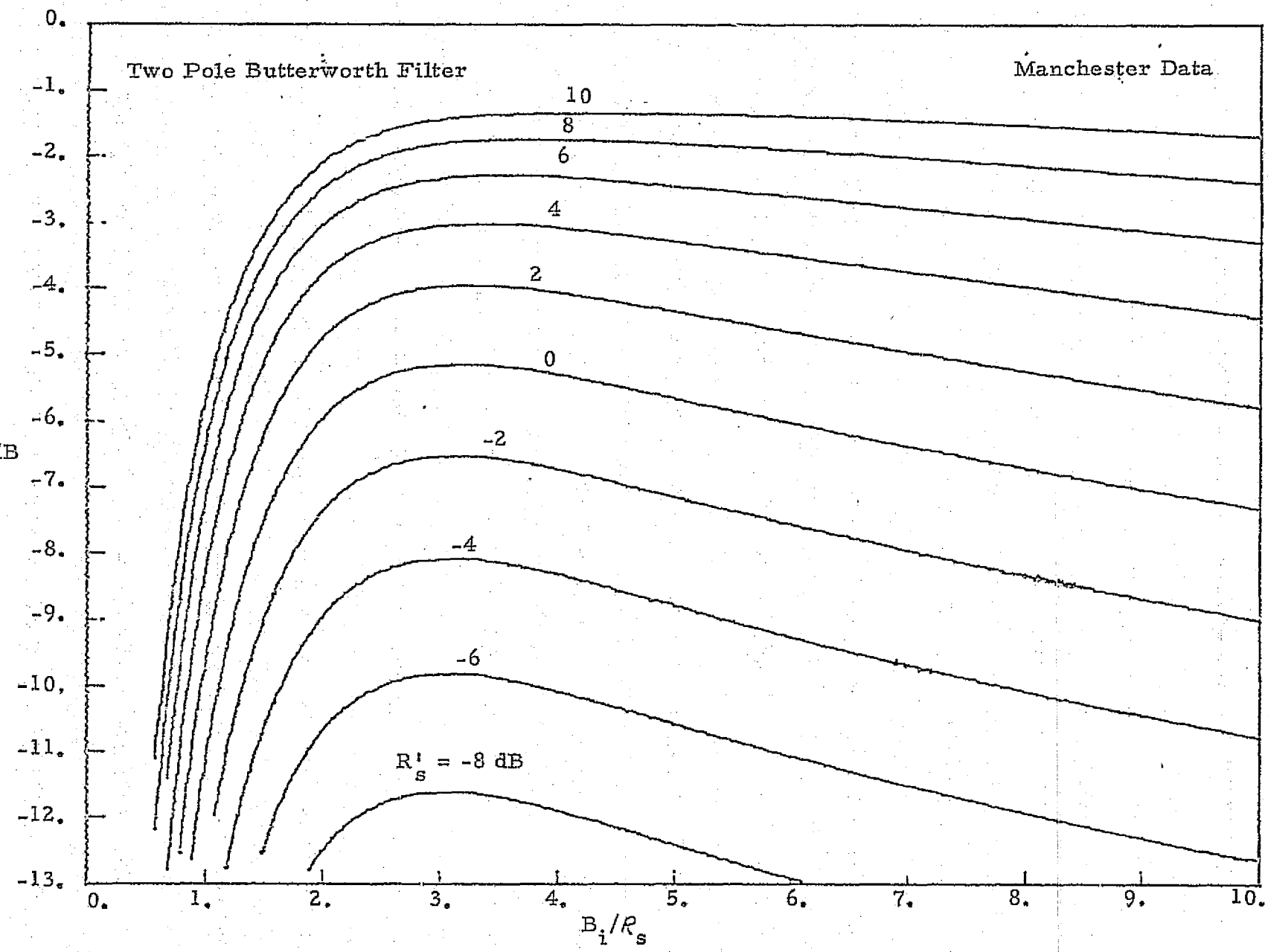

Fig. 1-2. Squaring Loss vs B_i/R_s with R_s' as a Parameter.

and for large loop signal-to-noise ratios becomes equal to the reciprocal of the effective loop signal-to-noise ratio. In the case of interest here, the tracking performance of the carrier-tracking loop depends, in addition, upon the timing error in the PN tracking loop which itself has a statistical characterization. Thus, the mean-squared tracking jitter for the Costas loop of Fig. 1-1 is given by

$$\sigma_{2\phi}^2 = \int_{-\pi}^{\pi}\int_{-1}^{1} (2\phi)^2 p(2\phi) p_\tau(\tau_e/\Delta) d(2\phi) d(\tau_e/\Delta) \tag{30}$$

where $p(2\phi)$ is given by (17) and $p_\tau(\tau_e/\Delta)$ is the probability density function of the normalized timing error τ_e/Δ in the PN tracking loop. Although $p_\tau(\tau_e/\Delta)$, in general, depends upon the specific PN tracking loop implementation, e.g., a noncoherent delay-locked loop or τ-dither loop, for large PN loop signal-to-noise ratios, $p_\tau(\tau_e/\Delta)$ is approximately Gaussian distributed, i.e.

$$p_\tau(\tau_e/\Delta) = \frac{1}{\sqrt{2\pi\sigma_\tau^2}} \exp\left[-\frac{(\tau_e/\Delta)^2}{2\sigma_\tau^2}\right] \tag{31}$$

and is thus characterized by a single parameter σ_τ, the standard deviation of τ_e/Δ. Furthermore, for large Costas loop signal-to-noise ratios,

$$\sigma_{2\phi}^2 \cong \frac{1}{\overline{\rho'}} \tag{32}$$

where

$$\overline{\rho'} = \int \rho' p_\tau(\tau_e/\Delta) d(\tau_e/\Delta) \tag{33}$$

Substituting (7), (19), (23) and (31) into (33) results in an expression for the <u>average effective signal-to-noise ratio</u> in the Costas loop

bandwidth, viz.

$$\overline{\rho'} = 2\int_0^1 \left(\frac{2S}{N_0 W_L}\right)\frac{(1-\tau_n)^2}{4}\left[\frac{D_m}{K_D+K_L\,\dfrac{B_i/R_s}{2\left(\dfrac{2S}{N_0 W_L}\right)\delta_s(1-\tau_n)^2 D_m}}\right]$$

$$\times\frac{1}{\sqrt{2\pi\sigma_\tau^2}}\exp\left[-\frac{\tau_n^2}{2\sigma_\tau^2}\right]d\tau_n \qquad (34)$$

where we have introduced the notation $\tau_n \triangleq \tau_e/\Delta$ and recognized the fact that the symbol signal-to-noise ratio R_s can be written as

$$R_s = \left(\frac{2S}{N_0 W_L}\right)\delta_s \,. \qquad (35)$$

with $\delta_s \triangleq \dfrac{2R_s}{W_L}$ the ratio of the symbol rate to single-sided Costas loop bandwidth. The value of B_i/R_s to be used in (34) is that which minimizes $\mathscr{L}_L$ (as in Fig. 1-2) for a given R_s. Since $R_s' = R_s$ when $\tau_e = 0$, these optimum values of B_i/R_s can be determined from Fig. 1-2 and remain constant over the integration on τ_n in (34). The values of D_m and K_D to be used in (34) are also evaluated at these optimum values of B_i/R_s. Figs. 1-3 and 1-4 plot ρ' vs $2S/N_0W_L$ for δ_s fixed and σ_τ a parameter. The dotted curve in each of these figures corresponds to the case of no squaring loss or PN degradation, i.e., $\rho' = (2S/N_0W_L)/4$. Thus, the distance between this dotted curve and the curve labeled $\sigma_\tau = 0$ represents the signal-to-noise ratio degradation due solely to the Costas loop squaring loss. The remaining curves represent the additional degradation due to imperfect PN tracking. These curves are very useful in assessing the combined performance of

the PN despreader and the Costas loop.

1.4 Characterization of the Cycle-Slipping Probabilities

In this section we shall characterize the probability that the 2ϕ process in the Costas loop slips one or more cycles in an interval T seconds.* To do this, we shall assume that the cycle slips which tend to increase and decrease 2φ by 2π form independent Poisson processes with rates of occurrence N_+ and N_- respectively. Then the probability that a net number, say N = n, of cycle slips occur in T seconds is given by (Ref. 2, Chap. 9)

$$P(N=n) = \left(\frac{N_+}{N_-}\right)^{\frac{n}{2}} \exp(-\bar{S}T) I_n(2T\sqrt{N_+ N_-}) \tag{36}$$

for $n = 0, \pm 1, \pm 2, \ldots$ where $\bar{S} \triangleq N_+ + N_-$ is the total number of cycles slipped per unit time independent of direction and $I_n(x)$ is the modified Bessel function of order n and argument x. The result (36) is shown by forming the convolution of the difference of two independent Poisson processes. The fact that the p.d.f. for cycle-slipping can be approximated by a Poisson process has been observed experimentally.

To rewrite Eq. (36) in terms of the system parameters previously defined we note from Ref. 2 that

$$\begin{aligned}
\frac{N_+}{N_-} &= \exp(2\pi\beta) \\
N_\pm &= \frac{W_L}{2\pi^2\rho'} \left[\frac{\exp(\pm\pi\beta)}{|I_{j\beta}(\rho')|^2}\right] \\
\bar{S} &= \frac{W_L}{\rho'} \left[\frac{\cosh \pi\beta}{\pi^2 |I_{j\beta}(\rho')|^2}\right]
\end{aligned} \tag{37}$$

*We shall for simplicity omit the effect of PN degradation in these calculations. Also a first-order loop will be assumed.

Thus, from (37) we get

$$\sqrt{N_+ N_-} = \frac{W_L}{2\pi^2 \rho' \left| I_{j\beta}(\rho') \right|^2} \tag{38}$$

Substituting (37) and (38) into (36) and making use of the definition of δ_s following (35) gives the desired result

$$\begin{aligned} P(N=n) &= \exp\left[n\pi\beta - \left(\frac{2\bar{S}}{W_L \delta_s} \right)\left(\frac{T}{T_s} \right) \right] I_n\left(\frac{2\left(\frac{T}{T_s} \right)}{\rho' \pi^2 \delta_s \left| I_{j\beta}(\rho') \right|^2} \right) \\ &= \exp\left[n\pi\beta - \frac{2 \cosh \pi\beta}{\rho' \pi^2 \delta_s \left| I_{j\beta}(\rho') \right|^2} \left(\frac{T}{T_s} \right) \right] I_n\left(\frac{2\left(\frac{T}{T_s} \right)}{\rho' \pi^2 \delta_s \left| I_{j\beta}(\rho') \right|^2} \right) \end{aligned} \tag{39}$$

Various methods for evaluating $\left| I_{j\beta}(\rho') \right|^2$ numerically are given in Appendices II and IV of Chap. 9 in Ref. 2. For example,

$$\left| I_{j\beta}(\rho') \right|^2 = \frac{1}{\pi \exp(-\beta\pi)} \int_0^{\pi} \exp(-2\beta z) I_0(2\rho' \sin z) dz \tag{40}$$

For a first-order loop, operating with steady-state phase error ϕ_{ss}, we have that

$$\beta = \rho' \sin \phi_{ss} \tag{41}$$

Also, from (19) the effective loop signal-to-noise ratio ρ' can be expressed in terms of the symbol signal-to-noise ratio $R_s = ST_s/N_0$ by

$$\rho' = \frac{R_s \delta_s}{4} \mathcal{L}_L \tag{42}$$

or for convolutionally-encoded data of rate $1/\nu$

$$\rho' = \frac{R_b \delta_s}{4\nu} \alpha_L' \tag{43}$$

Thus, substituting (41) and (43) into (39), one obtains an expression for the probability of N cycle slips in T seconds as a function of δ_s, T/T_s, R_s (or R_b), and ϕ_{ss}. Figs. 1-5 to 1-10 plot P(N=n) vs T/T_s for δ_s and ϕ_{ss} fixed and R_b as a parameter. Values of n = 1 and n = 2 are chosen as representative of the physical situation since the probability of three or more cycle slips is insignificant relative to the other two probabilities. Also, the rate 1/3 Shuttle code is assumed and R_b is allowed to range over the values -1 dB to 4 dB. The value of α_L' used in all cases is the optimum as determined from Fig. 1-2.

Fig. 1-3. Average Effective Signal-to-Noise Ratio in Costas Loop Bandwidth vs. $2S/N_0W_L$ with PN Loop rms Sync Error σ_τ as a Parameter.

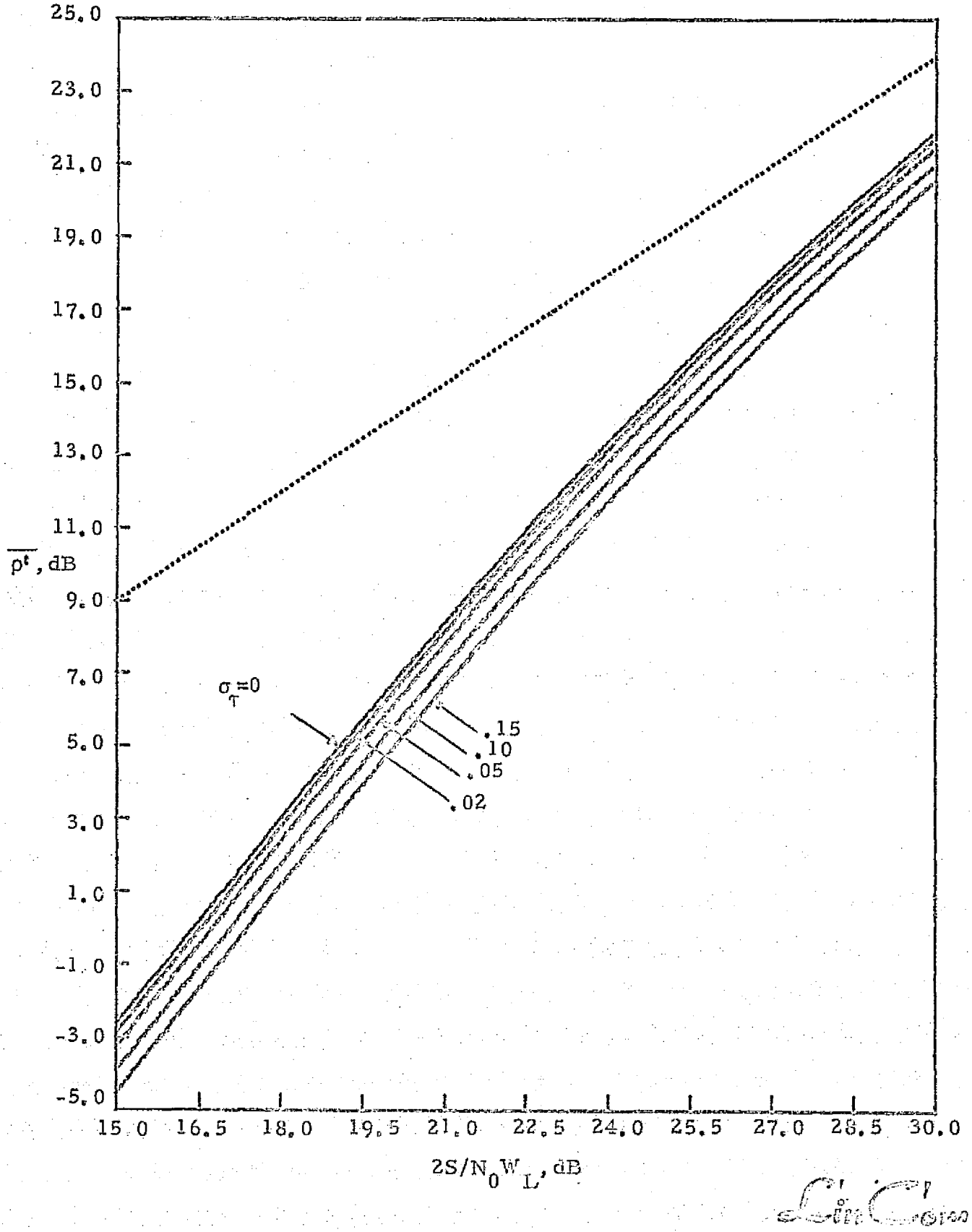

Fig. 1-4. Average Effective Signal-to-Noise Ratio in Costas Loop Bandwidth vs $2S/N_0/W_L$ with PN Loop rms Sync Error σ_T as a Parameter.

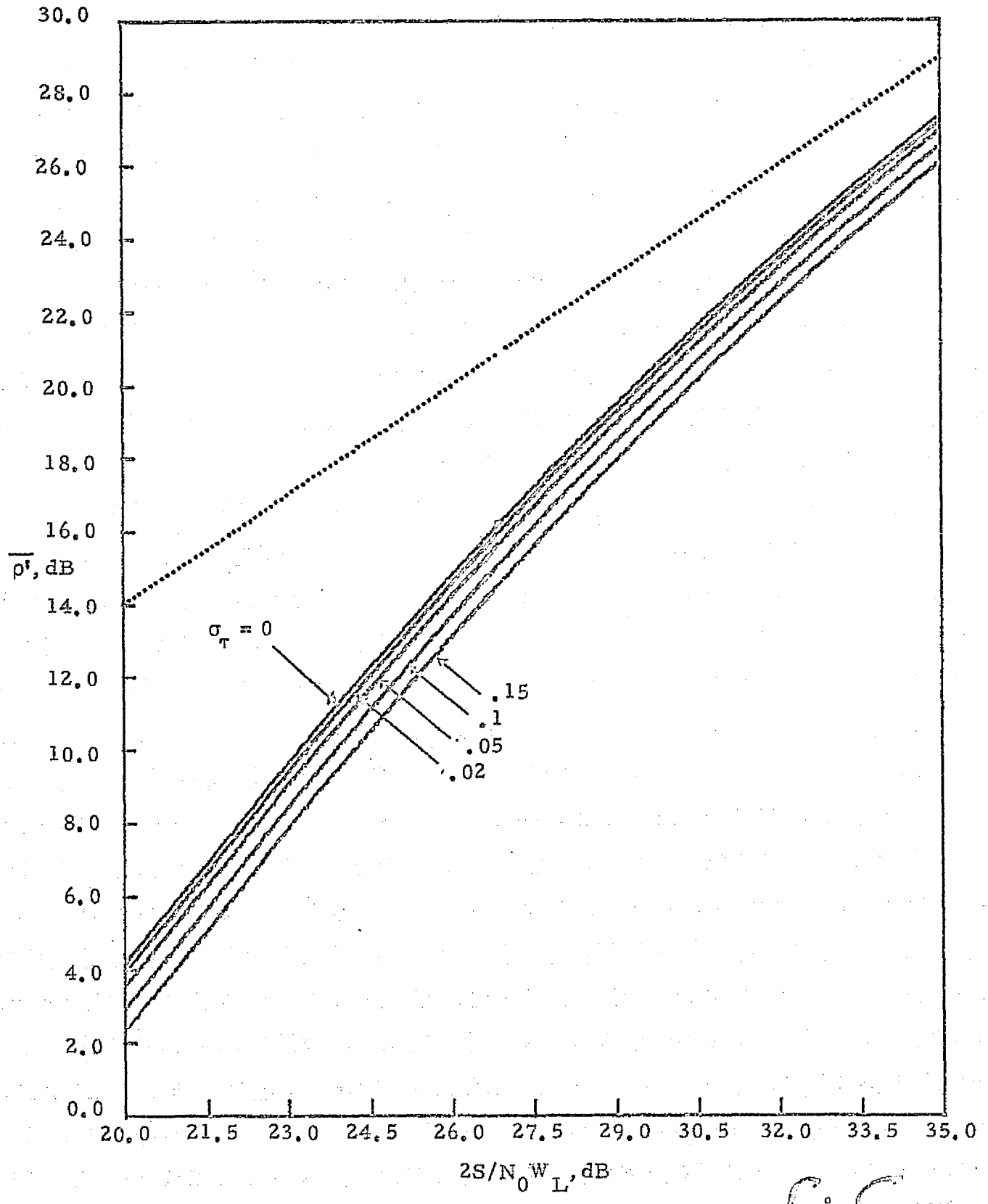

LinCom

Fig. 1-5. Cycle Slipping Probabilities vs Normalized Time with Energy-Per-Bit to Noise Ratio a Parameter.

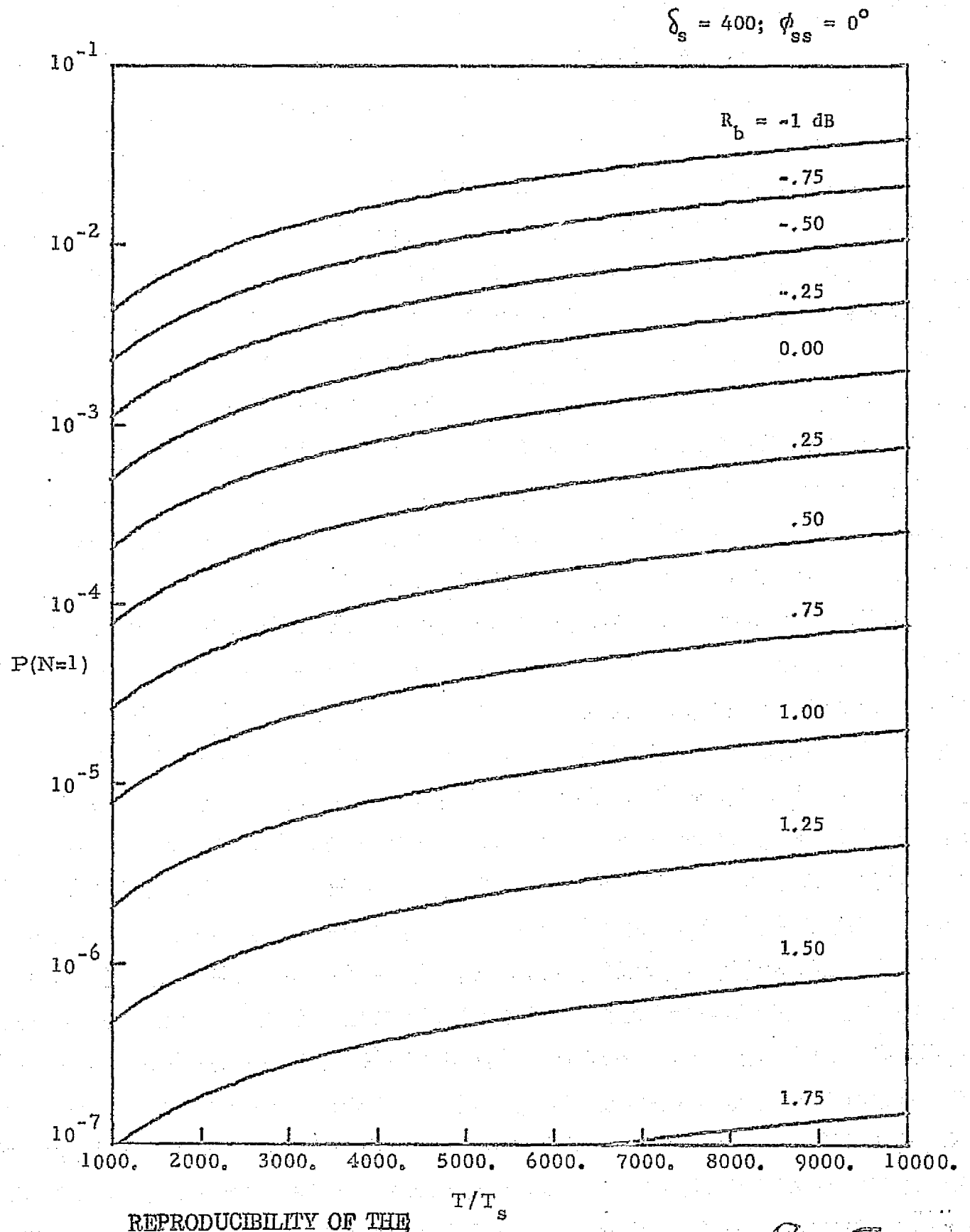

Fig. 1-6. Cycle Slipping Probabilities vs Normalized Time with Energy-Per-Bit to Noise Ratio a Parameter.

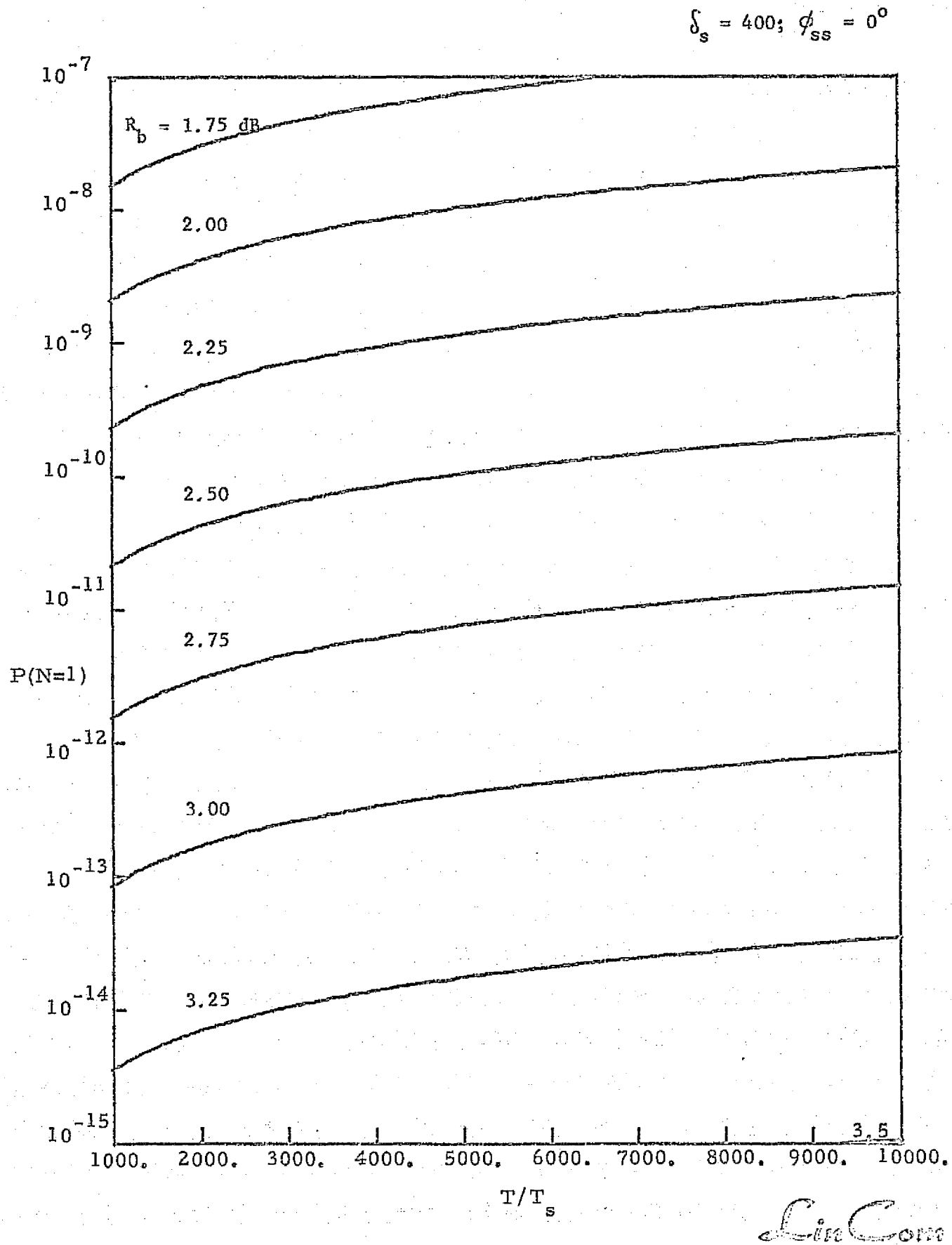

Fig. 1-7. Cycle Slipping Probabilities vs Normalized Time with Energy-Per-Bit to Noise Ratio a Parameter.

$\delta_s = 400$; $\phi_{ss} = 0^o$

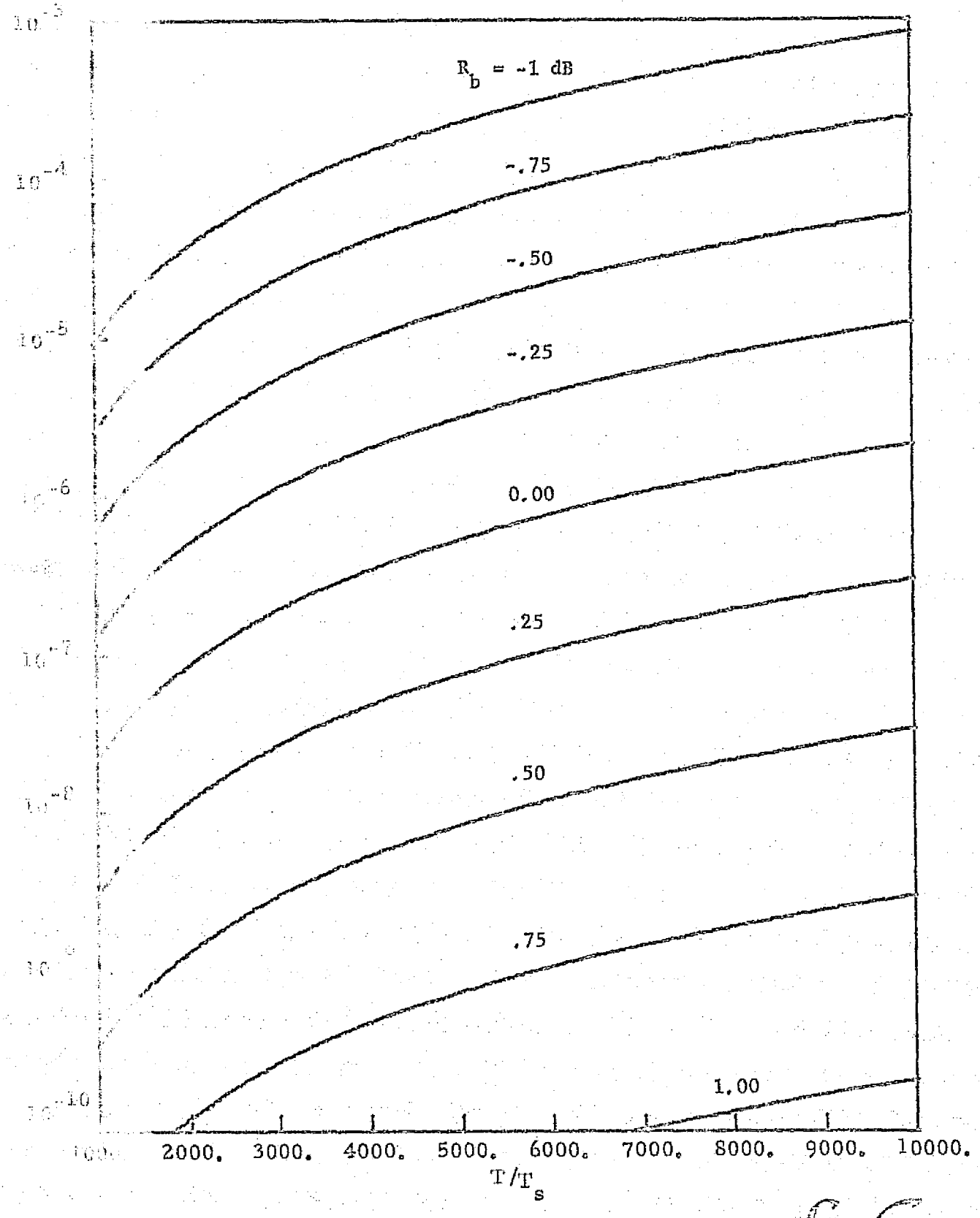

Fig. 1-8. Cycle Slipping Probabilities vs Normalized Time with Energy-Per-Bit to Noise Ratio a Parameter.

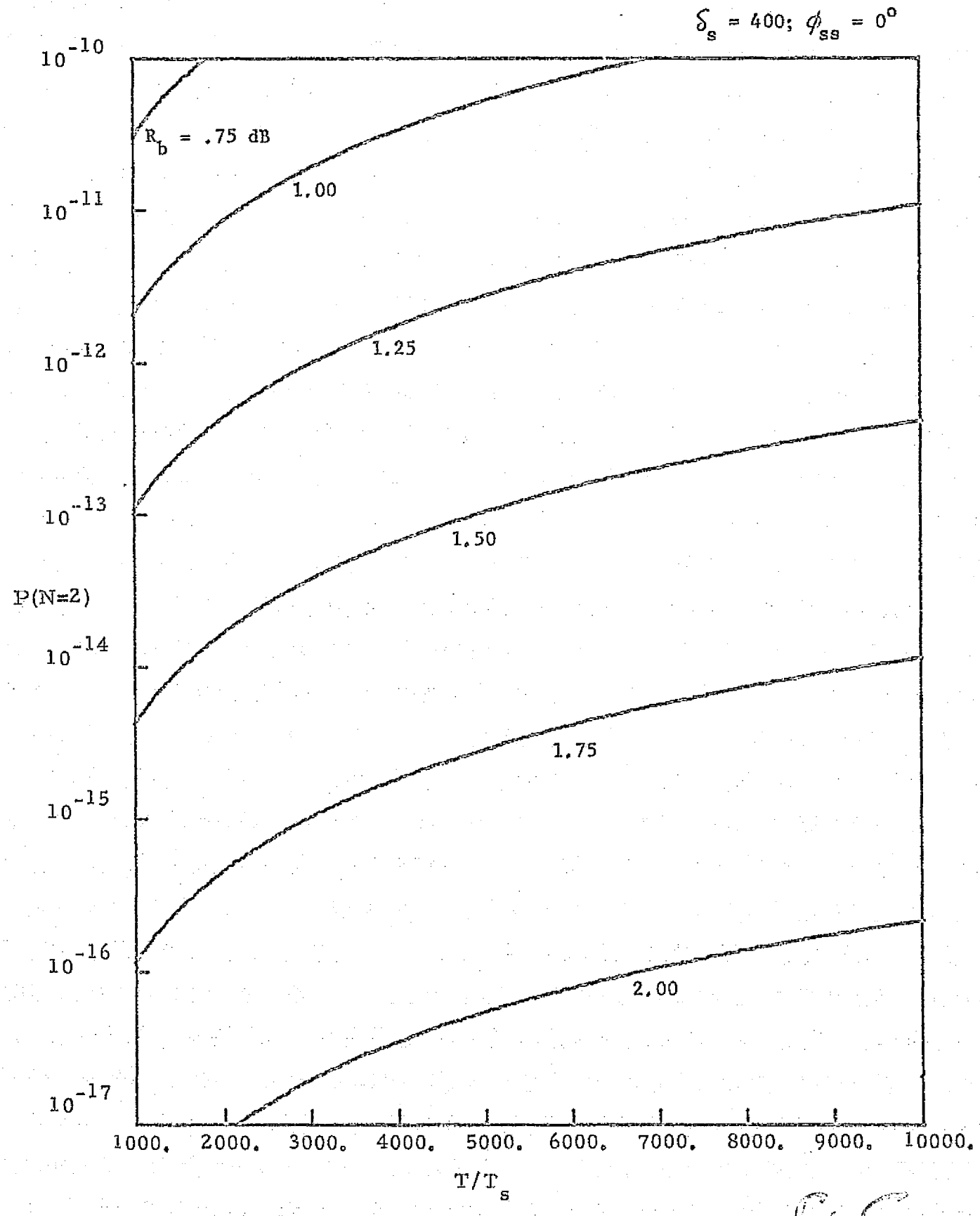

Fig. 1-9. Cycle Slipping Probabilities vs Normalized Time with Energy-Per-Bit to Noise Ratio a Parameter.

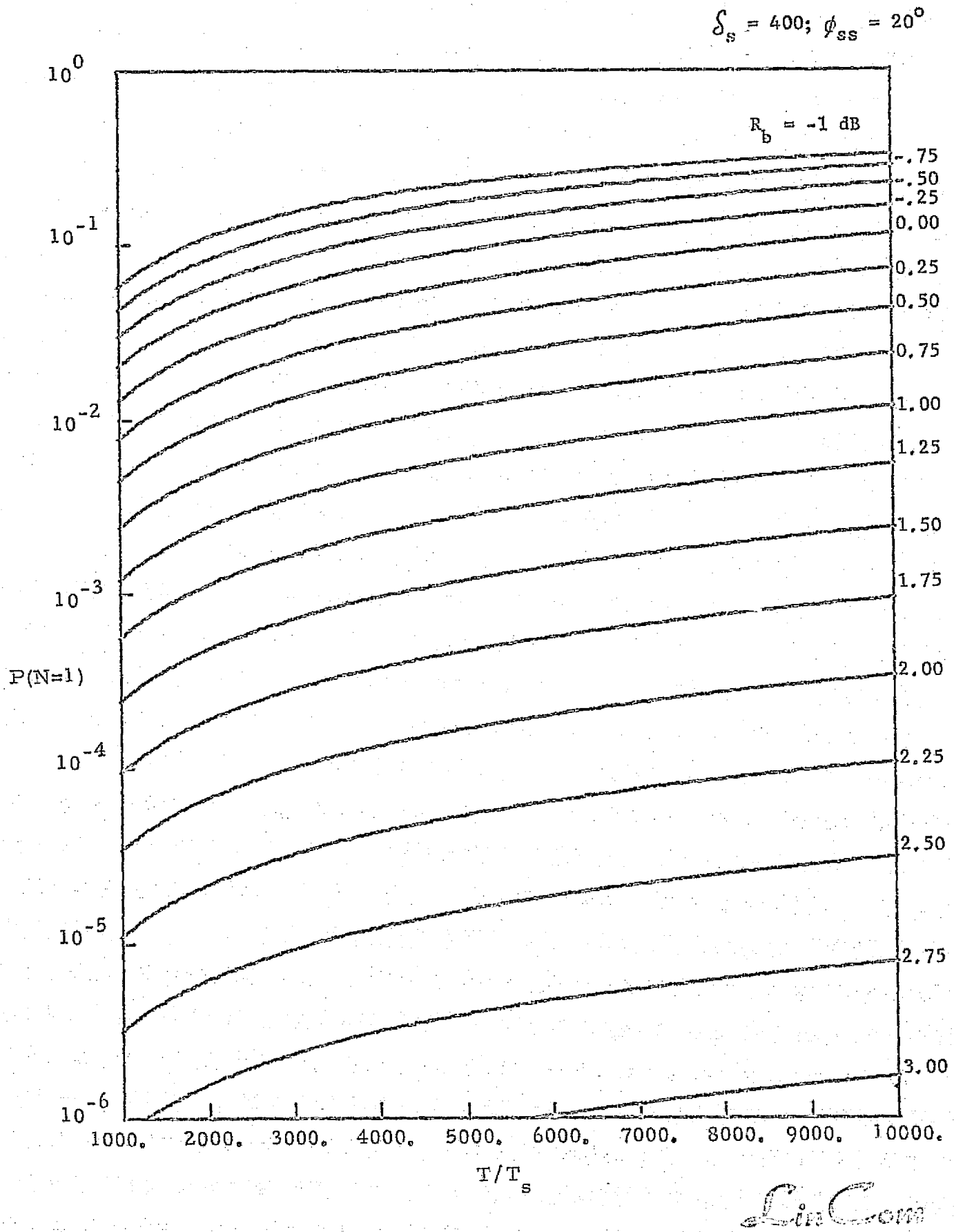

Fig. 1-10. Cycle Slipping Probabilities vs Normalized Time with Energy-Per-Bit to Noise Ratio a Parameter.

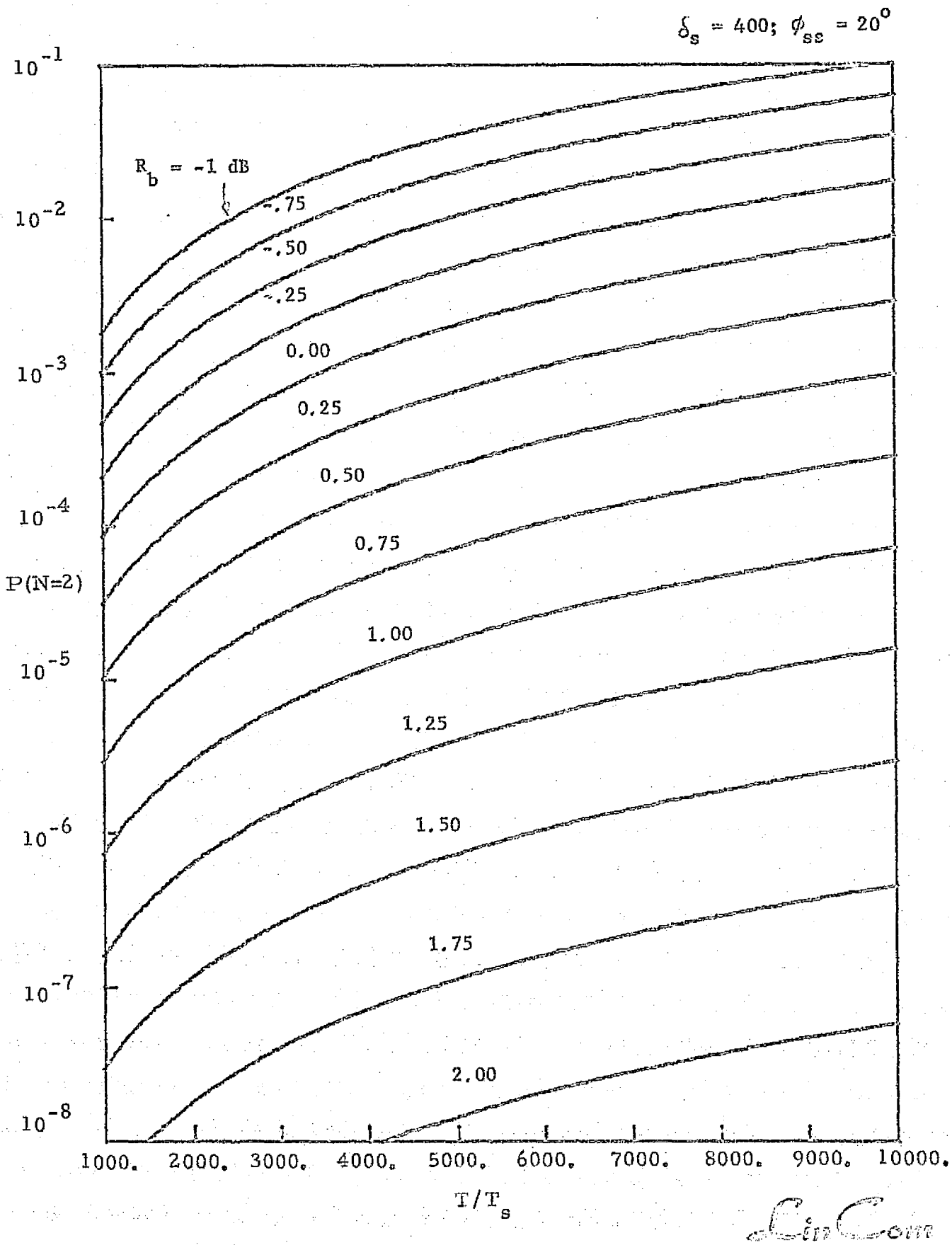

References for Section 1.0

1. Lindsey, W. C. and Simon, M. K., Telecommunication Systems Engineering, Prentice-Hall, Inc., Englewood Cliffs, New Jersey, 1973.

2. Lindsey, W. C., Synchronization Systems in Communication and Control, Prentice-Hall, Inc., Englewood Cliffs, New Jersey, 1972.

3. Van Trees, H., "Optimum Power Division in Coherent Communication Systems," M.I.T. Lincoln Lab., Lexington, Mass., Technical Report 301, February, 1963.

4. Didday, R. L., and Lindsey, W. C., "Subcarrier Tracking Methods and Communication System Design," IEEE Transactions on Communication Technology, Vol. COM-16, No. 4 (Aug., 1968), 541-550.

5. Lindsey, W. C., and Simon, M. K., "Nonlinear Analysis of Suppressed Carrier Tracking Loops in the Presence of Frequency Detuning," Proceedings of the IEEE, Vol. 58, No. 9 (Sept. 1970), 1302-1321.

6. Costas, J. P., "Synchronous Communications, Proceedings of IRE, Vol. 44 (Dec., 1956), 1713-1718.

7. Natali, F. D., and Walbesser, W. J., "Phase-Locked Loop Detection of Binary PSK Signals Utilizing Decision Feedback," IEEE Transactions on Aerospace and Electronic Systems, Vol. AES-5, No. 1 (Jan., 1969), 83-90.

8. Lindsey, W. C., and Simon, M. K., "Data-Aided Carrier Tracking Loops," IEEE Transactions on Communication Technology, Vol. COM-19, No. 2, (April, 1971), 157-168.

9. Proakis, J. G., Drouilhet, P. R., Jr., and Price, R., "Performance of Coherent Detection Systems Using Decision-Directed Channel Measurements," IEEE Transactions on Communication Systems, Vol. CS-12, No. 1 (March, 1964), 54-63.

10. Batson, B. H., and Moorehead, R. W., "A Digital Communications System for Manned Spaceflight Applications," ICC Conference Record, 1973, pp. 37-1 - 37-9.

11. JSC/GSFC Space Shuttle Communications and Tracking Interface Control Document, Appendix B, ICD-2-0D004, NASA Lyndon B. Johnson Space Center, Houston, Texas, January, 1975.

12. TDRSS User's Guide, Revision 2, Goddard Space Flight Center, Greenbelt, Maryland, May, 1975.

13. Lindsey, W. C., "Design and Performance of Costas Receivers Containing Bandpass Limiters," under Contract No. NAS 9-13467 to Axiomatic Corp., Marina del Rey, Calif., Axiomatix Report No. R7502-2, Feb. 18, 1975.

14. Lindsey, W. C., "Optimum Performance of Costas Type Receivers," under Contract No. NAS 9-13467 to Axiomatix Corp., Marina del Rey, Calif., Axiomatix Report No. R7502-1, Feb. 18, 1975.

2.0 AVERAGE ERROR PROBABILITY PERFORMANCE OF CONVOLUTIONALLY CODED SYSTEMS IN THE PRESENCE OF IMPERFECT CARRIER SYNC

2.1 Introduction

Having thus characterized two sources of imperfect synchronization that degrade system performance what remains is to evaluate their effect on the average error probability performance of the data decoder which in the case of the Shuttle forward and return S-band relay links is a maximum-likelihood (Viterbi) decoder of a rate one-third, constraint length seven convolutional code. A general solution of this problem is indeed quite difficult; however, depending on the relation among particular system operating parameters, e.g., symbol rate, decoder memory, loop bandwidths, etc., there exist approaches which yield veritable results in the face of the underlying assumptions and approximations made.

One approach which has been taken by several authors (Refs. 1, 2) with regard to evaluating performance degradation due to imperfect carrier synchronization is as follows: (a) determine (by simulation studies) the ideal bit error probability performance curve for the particular convolutional code under consideration, (b) curve fit (using perhaps a least squares approach) a mathematical function to the simulation data, (c) degrade the signal-to-noise ratio in this function by the cosine squared of the carrier synchronization phase error, and (d) average the resulting function over the p.d.f. of the phase error as determined from the analyses performed on the carrier synchronization loop. Inherent in this approach, is the assumption that the loop phase error is approximately constant over the number of symbols required to arrive at a single bit decision, i.e., the Viterbi decoder memory length in symbols. Typically, this memory

runs on the order of five or six constraint lengths for which a constraint length seven code is about forty symbols. Thus a symbol rate of 216 Ksps would require that the two-sided carrier tracking loop bandwidth, W_L, be much less (e.g., a factor of 100 or more) than 216/40 = 5.4 KHz.

We begin by finding a suitable curve fit model for the Shuttle K = 7, rate 1/3 convolutional code. This code, which is the "best" rate 1/3, constraint length 7 convolutional code (Ref. 3), is characterized by the generator matrix.

$$\underset{\sim}{G} = \begin{bmatrix} 1 & 1 & 1 & 1 & 0 & 0 & 1 \\ 1 & 1 & 0 & 0 & 1 & 0 & 1 \\ 1 & 0 & 1 & 1 & 0 & 1 & 1 \end{bmatrix} \tag{1}$$

and is the identical code used by the LINKABIT LV7015LR Viterbi decoder which employs 3-bit soft quantization of the received data. Using previously published simulation results (Ref. 4) we find that over the range of bit signal-to-noise ratios from -1 dB to 4 dB (corresponding to a range of bit error probabilities from approximately 2×10^{-1} to 10^{-5}), a second-order polynomial fit is quite accurate, i.e.

$$\log_{10} P_b = a_1(10 \log_{10} R_b)^2 + a_2(10 \log_{10} R_b) + a_3 \tag{2}$$

where the constants a_1, a_2, and a_3 are chosen to satisfy three data points on the simulated curve. In particular, simultaneous solution of the three resulting linear equations gives

$$\begin{aligned} a_1 &= -.1206 \\ a_2 &= -.5 \\ a_3 &= -1.0706 \end{aligned} \tag{3}$$

Using this curve fit model, numerical results can be obtained for the noisy reference effect of the Costas loop on the bit error probability performance of this particular code. The results will be plotted with the ratio of bit rate to loop bandwidth held constant and static phase error (caused by Doppler offset) as a parameter. In all cases, the Costas loop is optimized in the sense of minimizing the loop's squaring loss (or equivalently, its mean-squared jitter) by proper choice for the arm filter bandwidth relative to the symbol rate. A two-pole Butterworth is chosen for the arm filters, representing a reasonable compromise between filter complexity and modulation distortion.

2.2 An Analytical Evaluation of Performance Degradation Due to a Noisy Carrier Sync Reference

Based upon the comments made in the introduction, we can immediately evaluate the average bit error probability performance in the presence of a noisy carrier sync reference from the following numerical integration:

$$P_b = 2\int_{-\frac{\pi}{2}}^{\frac{\pi}{2}} P_b(R_b \cos^2\phi)\, p(2\phi)\, d\phi \tag{4}$$

where from (2) and (3)

$$P_b(R_b \cos^2\phi) = 10^{-.1206(10\log_{10} R_b \cos^2\phi)^2 - .5(10\log_{10} R_b \cos^2\phi) - 1.0706} \tag{5}$$

and $p(2\phi)$ is the p.d.f. of the suppressed carrier-tracking loop phase error. Implicit in (4) is the fact that the 180° phase ambiguity, which is characteristic of all suppressed-carrier tracking loops, has been perfectly resolved. Techniques for

accomplishing this resolution are discussed in the section on average symbol transition density of convolutional codes.

When a Costas loop is employed for establishing the required carrier sync reference, then the p.d.f. $p(2\phi)$ is given by

$$p(2\phi) = C_1 \exp[\rho' \cos 2\phi + \beta(2\phi)] \int_{\phi}^{\phi+\pi} \exp[-\rho' \cos 2y - \beta(2y)]dy; \quad |\phi| \leq \pi \tag{6}$$

where C_1 is a normalization constant such that

$$\int_{-\pi}^{\pi} p(2\phi)d\phi = 2\int_{-\frac{\pi}{2}}^{\frac{\pi}{2}} p(2\phi)d\phi = 1 \tag{7}$$

and

$$\rho' = \frac{\rho \mathscr{L}_L}{4} \; ; \quad \rho \triangleq \frac{2S}{N_0 W_L}$$
$$\beta = \rho' \sin \phi_{ss} \tag{8}$$

In (8), the parameter $\mathscr{L}_L$ is the loop's squaring loss, W_L is its two-sided noise bandwidth, and ϕ_{ss} is the static phase error caused by Doppler offset. Defining the ratio of symbol rate to single-sided loop bandwidth by

$$\delta_s = \frac{2R_b}{W_L} \tag{9}$$

then

$$\rho = \frac{R_b \delta_s}{\nu} \tag{10}$$

where $1/\nu$ is the rate of the code.

Figures 2-1 and 2-2 represent plots of bit error probability vs energy per bit to noise ratio. These results were

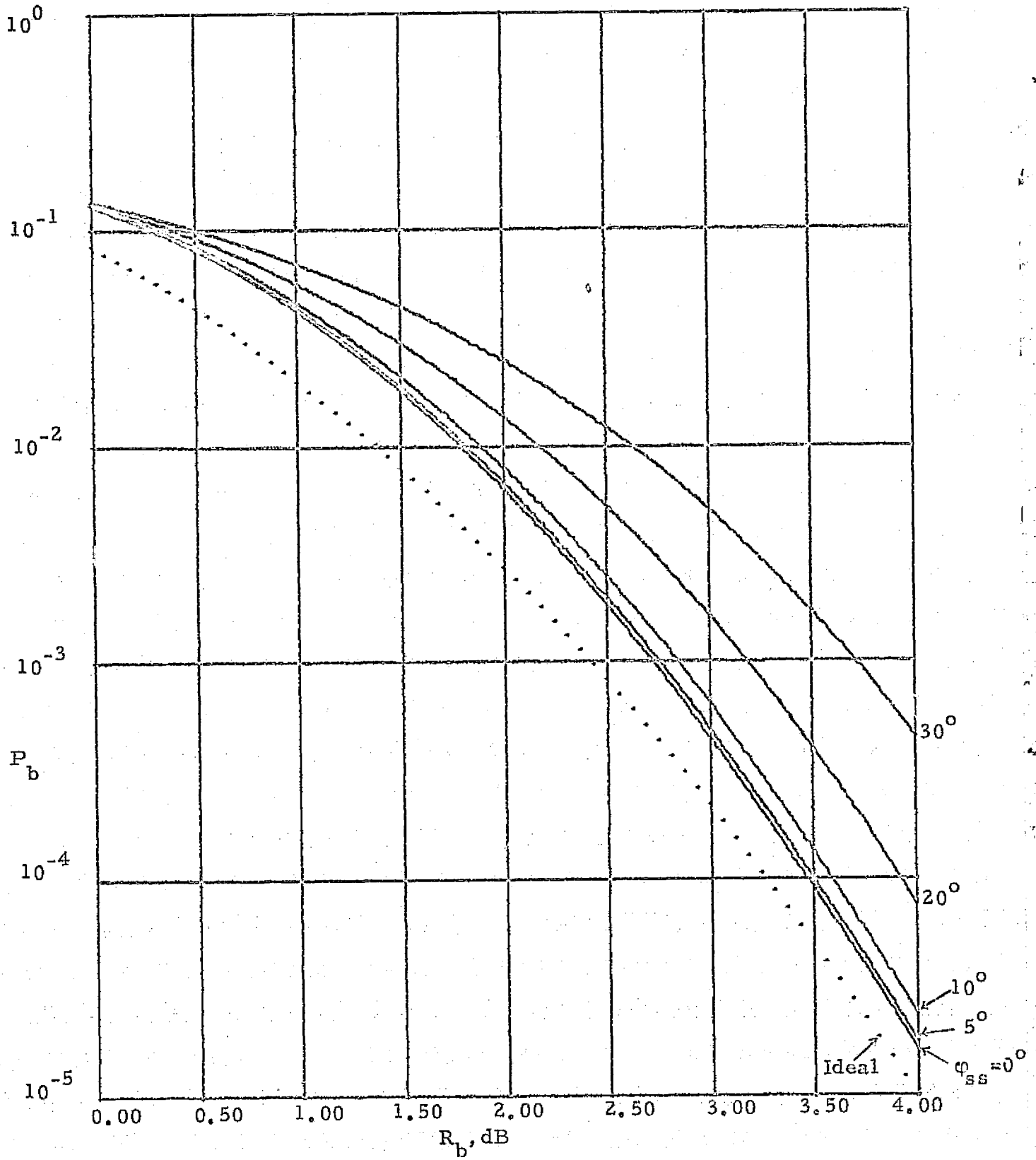

Fig. 2-1. Bit Error Probability Performance of K=7, Rate 1/3 Shuttle Code with Loop Static Phase Error a Parameter; $\delta_s = 216$.

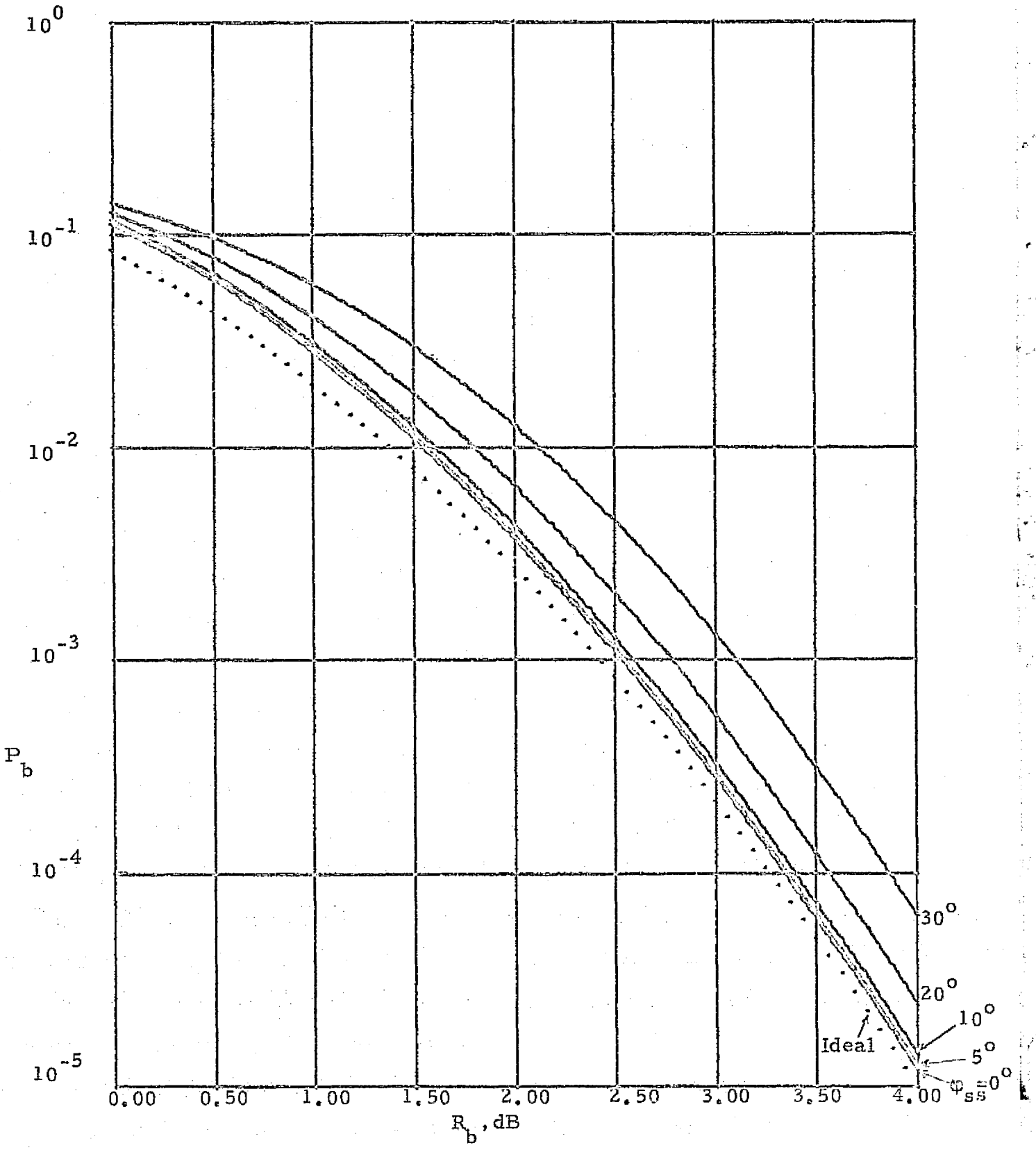

Fig. 2-2. Bit Error Probability Performance of K=7, Rate 1/3 Shuttle Code with Loop Static Phase Error as a Parameter; δ_s = 432.

obtained via numerical integration of (4) using (5) and (6). These curves are illustrated for the Shuttle K = 7 and $\nu = 3$ convolutional code. For $\delta_s = 432$ or 216, notice the degrading effects due to the static phase error. In addition, it should be noted that other degradations due to filters in the signal path can easily be incorporated and Figures 2-1 and 2-2 used to indicate the total loss due to the noisy carrier reference, when the various filters in the receiver are assumed to be present.

References for Section 2.0

1. Heller, J. A., and Jacobs, I. M., "Viterbi Decoding for Satellite and Space Communication," IEEE Transactions on Communication Technology, Vol. COM-19, No. 5, October 1971, pp. 835-848.

2. Merrill, H. M., and Thompson, G. D., Jr., "Design of Communication Systems Using Short-Constraint-Length Convolutional Codes," 1972 National Telecommunications Conference Record, Houston, Texas, pp. 13A-1 - 13A-6.

3. Odenwalder, J. P., "Optimal Decoding of Convolutional Codes," PhD Dissertation, University of California at Los Angeles, 1970.

4. Heller, J. A., Odenwalder, J. P., and Viterbi, A. J., "Coded Spread Spectrum Transmission System Design Study," Final Report on Contract No. NAS9-13733, National Aeronautics and Space Administration, Lyndon B. Johnson Space Center, Houston, Texas, May, 1974.

3.0 SYMBOL SYNCHRONIZATION OF MANCHESTER CODED DATA

3.1 Introduction

The technical literature abounds with information relating to the problem of establishing symbol synchronization in binary baseband digital communication systems transmitting NRZ-L data (Refs. 1-15). By comparison, very little has been said (Refs. 16-18) regarding the extraction of symbol sync from Bi-phase-L (Manchester coded) data. In many applications (e.g. Shuttle relay links), however, the advantage of an increased average transition density (a factor of three for random data) offered by Manchester coding overshadows its potential disadvantages such as the introduction of a half-symbol ambiguity requiring resolution and the approximately doubled bandwidth occupancy. Thus, in these instances, the problem of providing symbol synchronization in the receivers of such systems requires special attention.

3.2 Maximum A Posteriori (MAP) Estimation of Symbol Sync

Regardless of the data format, the question of what is the "optimum" symbol synchronizer is a natural one to ask. The answer to this question, of course, depends highly upon the criterion of optimality one selects. The maximum a posteriori (MAP) estimation criterion represents one approach to the problem. Although this approach unfortunately avoids a direct attack on the important problems associated with symbol sync acquisition time, acquisition range, and maximum probability of acquisition, it does, however, afford a great deal of insight into arriving at closed loop synchronizer configurations whose high and low-signal-to-noise ratio approximations are physically and practically

realizable, and yield good, if not the best, tracking performance. In fact, we shall demonstrate that, under certain practical conditions, the rules governing the design of the symbol synchronizer motivated by the MAP estimation approach are indeed identical to those which minimize its mean-squared symbol sync jitter.

A derivation of the MAP estimator of symbol sync is given in Ref. 1 where an arbitrary time-limited symbol pulse waveshape $p_s(t)$ of energy $E_s = ST_s$ and equiprobable symbols are assumed. Furthermore, the derivation assumed that the symbol length T_s is known (and remains constant over the observation interval), and that a stored replica of the transmitted signal waveshape is available at the receiver.

To apply this body of theory to the case of Manchester coded symbols, we define the pulse shape $p_s(t)$ by

$$p_s(t) = \begin{cases} \sqrt{S}\,; & 0 \le t \le T_s/2 \\ -\sqrt{S}\,; & T_s/2 \le t \le T_s \end{cases} \tag{1}$$

Also, to allow for average symbol transition densities other than one-half, we can assume a data stream of independent symbols with a priori probabilities p and q = 1-p and modify the derivation accordingly.* Without belaboring the details, one can show that, analogous to Eq. (9-14) of Ref. 1, the MAP estimate of ε--that is, $\hat{\varepsilon}$--is the value of ε that maximizes

$$\Lambda(y,\varepsilon) \triangleq \ln f(y,\varepsilon) = \sum_{k=0}^{K} \ln \left\{ p \exp\left[\frac{2}{N_0}\int_{T_k(\varepsilon)} y_k(t)p_s[t-(k-1)T_s-\varepsilon]dt\right] + q \exp\left[-\frac{2}{N_0}\int_{T_k(\varepsilon)} y_k(t)p_s[t-(k-1)T_s-\varepsilon]dt\right]\right\} \tag{2}$$

*Many other possibilities exist for statistically modeling the data stream; however, the MAP estimate solution becomes quite complex for any model other than the one assumed above.

where

$$y(t) = \sum_{k=0}^{K} a_k p_s[t-(k-1)T_s-\epsilon] + n(t); \quad 0 \le t \le kT_s \tag{3}$$

is the received symbol data stream in noise over the observation interval ($0 \le t \le kT_s$), a_k is the polarity (± 1) of the k^{th} transmitted symbol, and $T_k(\epsilon)$ is the k^{th} subinterval defined by $(k-1)T_s+\epsilon \le t \le kT_s+\epsilon$. Furthermore, the additive noise, $n(t)$ is assumed to be white Gaussian with single-sided noise spectral density N_0.

Alternately, the MAP estimator is that value of ϵ which satisfies

$$\left.\frac{\partial \Lambda(y,\epsilon)}{\partial \epsilon}\right|_{\epsilon=\hat{\epsilon}} = \sum_{k=0}^{K} \frac{2}{N_0}\left\{\int_{T_k(\epsilon)} y(t)\,\frac{\partial p_s[t-(k-1)T_s-\hat{\epsilon}]}{\partial \hat{\epsilon}}\,dt + y(kT_s+\hat{\epsilon})p_s(T_s) - y[(k-1)T_s+\hat{\epsilon}]p_s(0)\right\}$$

$$\times \frac{p\exp\left\{\frac{2}{N_0}\int_{T_k(\hat{\epsilon})} y(t)p_s[t-(k-1)T_s-\hat{\epsilon}]dt\right\} - q\exp\left\{-\frac{2}{N_0}\int_{T_k(\hat{\epsilon})} y(t)p_s[t-(k-1)T_s-\hat{\epsilon}]dt\right\}}{p\exp\left\{\frac{2}{N_0}\int_{T_k(\hat{\epsilon})} y(t)p_s[t-(k-1)T_s-\hat{\epsilon}]dt\right\} + q\exp\left\{-\frac{2}{N_0}\int_{T_k(\hat{\epsilon})} y(t)p_s[t-(k-1)T_s-\hat{\epsilon}]dt\right\}}$$

$$= 0 \tag{4}$$

For any estimate of ϵ other than the MAP estimate, the function $\partial\Lambda(y,\epsilon)/\partial\epsilon$ will be either positive or negative depending on whether $\epsilon < \hat{\epsilon}$ or $\epsilon > \hat{\epsilon}$ and hence can be used to provide search direction. A simple example of a closed-loop symbol synchronizer that incorporates $\partial\Lambda(y,\epsilon)/\partial\epsilon$ as an error signal is illustrated in Fig. 3-1, where for simplicity we have assumed $p_s(0) = p_s(T) = 0$.

For large E_s/N_0, the following approximation can be made:

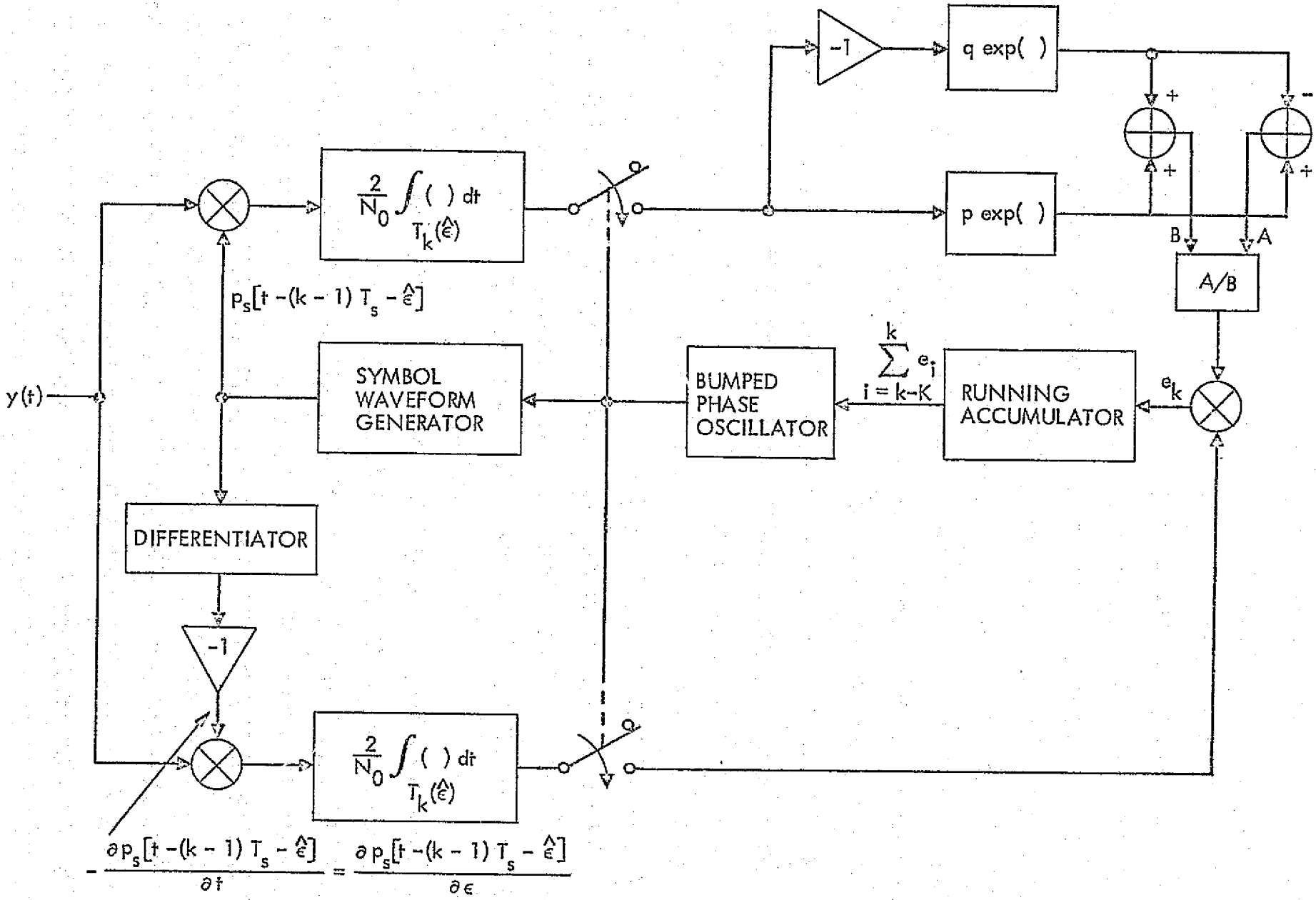

Fig. 3-1. A Closed Loop Symbol Synchronizer Motivated By the MAP Estimation Approach.

$$\frac{p\exp\left\{\frac{2}{N_0}\int_{T_k(\hat{\epsilon})} y(t)p_s[t-(k-1)T_s-\hat{\epsilon}]dt\right\}-q\exp\left\{-\frac{2}{N_0}\int_{T_k(\hat{\epsilon})} y(t)p_s[t-(k-1)T_s-\hat{\epsilon}]\,dt\right\}}{p\exp\left\{\frac{2}{N_0}\int_{T_k(\hat{\epsilon})} y(t)p_s[t-(k-1)T_s-\hat{\epsilon}]dt\right\}+q\exp\left\{-\frac{2}{N_0}\int_{T_k(\hat{\epsilon})} y(t)p_s[t-(k-1)T_s-\hat{\epsilon}]\,dt\right\}}$$

$$\cong \operatorname{sgn}\left\{\frac{2}{N_0}\int_{T_k(\hat{\epsilon})} y(t)p_s[t-(k-1)T_s-\hat{\epsilon}]dt\right\} \qquad (5)$$

where sgn( ) is the signum function. Likewise, for small E_s/N_0, we have

$$\frac{p\exp\left\{\frac{2}{N_0}\int_{T_k(\hat{\epsilon})} y(t)p_s[t-(k-1)T_s-\hat{\epsilon}]dt\right\}-q\exp\left\{-\frac{2}{N_0}\int_{T_k(\hat{\epsilon})} y(t)p_s[t-(k-1)T_s-\hat{\epsilon}]dt\right\}}{p\exp\left\{\frac{2}{N_0}\int_{T_k(\hat{\epsilon})} y(t)p_s[t-(k-1)T_s-\hat{\epsilon}]dt\right\}+q\exp\left\{-\frac{2}{N_0}\int_{T_k(\hat{\epsilon})} y(t)p_s[t-(k-1)T_s-\hat{\epsilon}]dt\right\}}$$

$$\cong (p-q) + 4pq\left[\frac{2}{N_0}\int_{T_k(\hat{\epsilon})} y(t)p_s[t-(k-1)T_s-\hat{\epsilon}]dt\right] \qquad (6)$$

Using (5) and (6) in Fig. 3-1, gives the equivalent high and low E_s/N_0 closed-loop configurations illustrated in Fig. 3-2.

For the Manchester pulse of (1), the output of the minus one amplifier following the differentiator in Figs. 3-1 or 3-2 is illustrated in Fig. 3-3. The strength η of the impulses at the edges of the symbol pulse is, in general, a random variable and depends upon the polarity of the preceding and succeeding symbol pulses. For example, in the k^{th} symbol interval, $\eta = 1$ if $a_{k-1} = a_k = a_{k+1}$, and $\eta = 0$ if $a_{k-1} \neq a_k$ and $a_{k+1} \neq a_k$. Since the probability of a data symbol transition is $p_t = 2pq$ and the probability of no transition is $1-p_t$, then the average value of η, namely $\overline{\eta}$, is given by

$$\overline{\eta} = 0 \times p_t + 1 \times (1-p_t) = 1 - p_t \qquad (7)$$

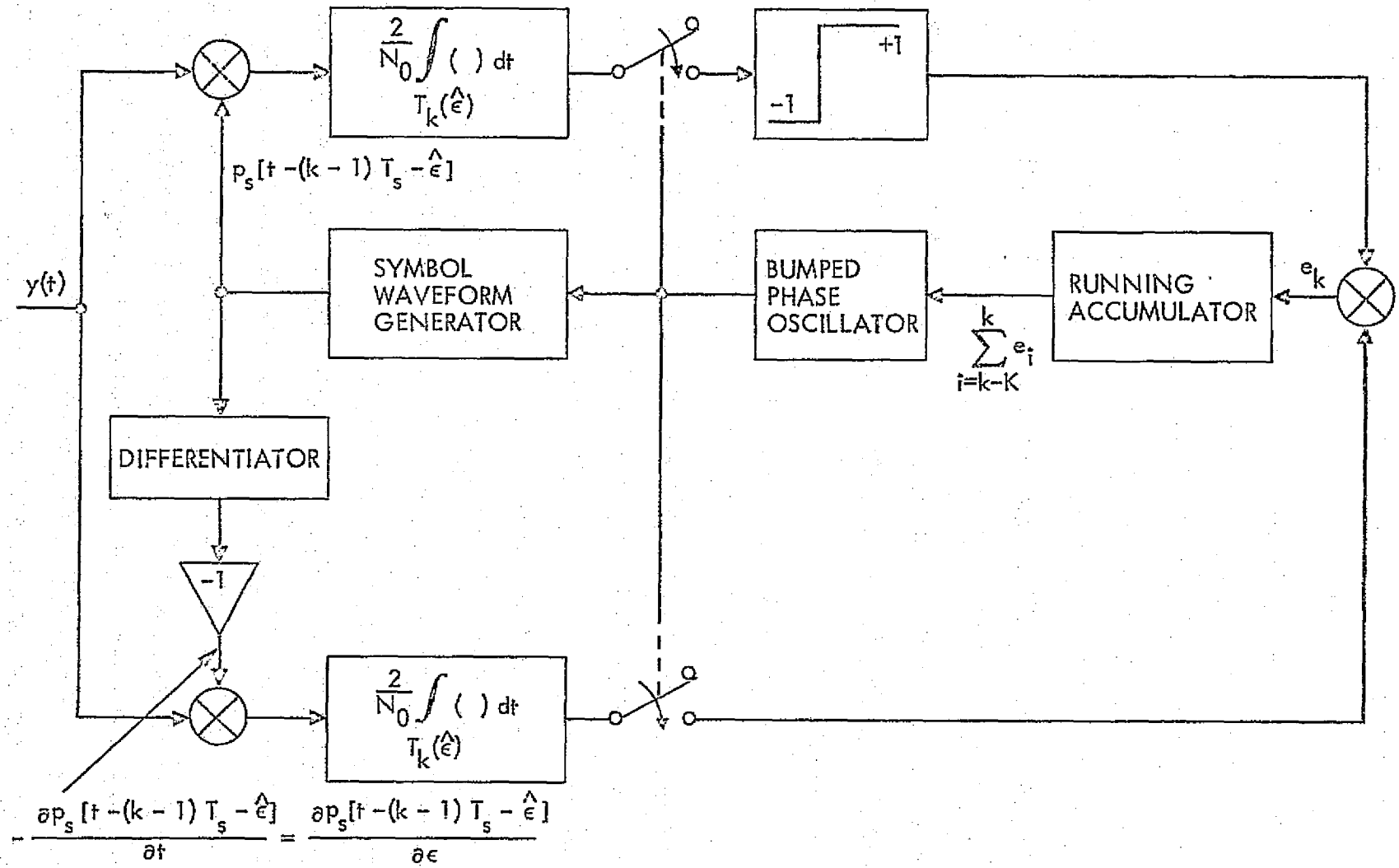

Fig. 3-2a. Large Signal-to-Noise Ratio Approximation of Fig. 1.

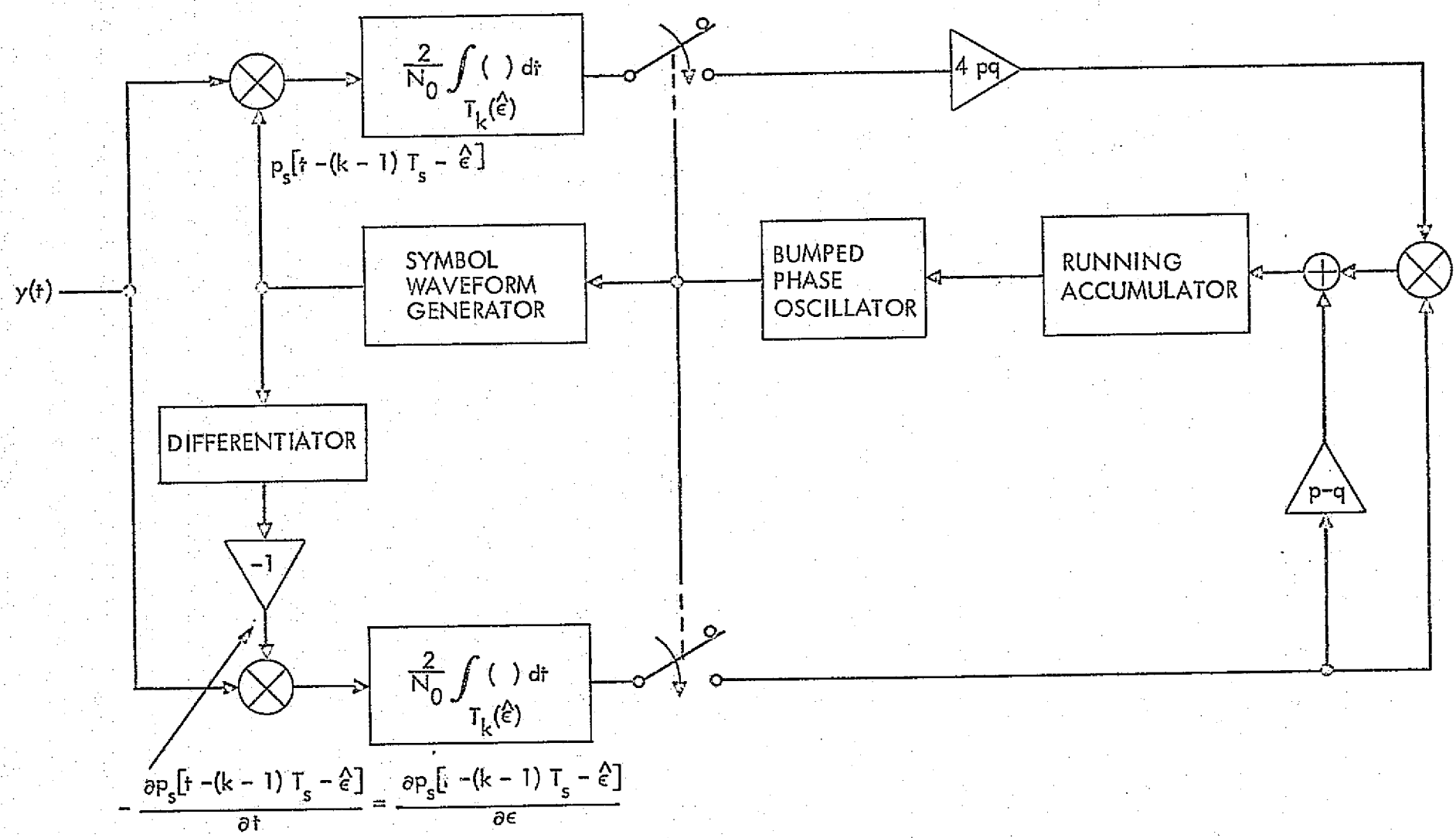

Fig. 3-2b. Small Signal-to-Noise Ratio Approximation of Fig. 1.

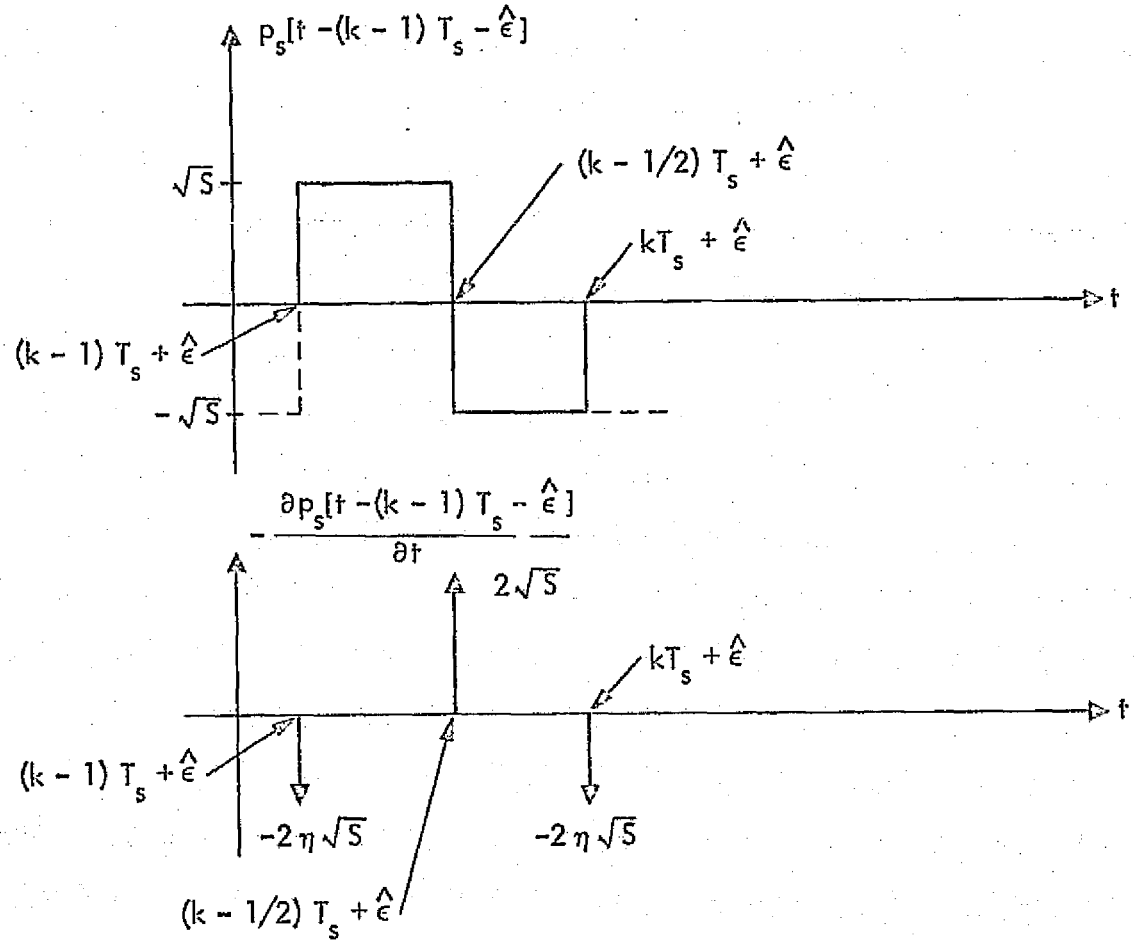

Fig. 3-3. Manchester Symbol Pulse Shape and Its Derivative.

Note that Eq. (7) is valid independent of the value of E_s/N_0.

In practice, the impulse functions discussed above would be approximated by finite width pulses. With regard to the impulses at the edges of the symbol pulse, there are two natural ways of making this approximation each of which leads to a different closed loop symbol synchronizer configuration. In one case, the cross-correlation reference signal at the lower phase detector in Fig. 3-1 or 2 might appear as the waveform illustrated in Fig. 3-4a. This reference signal has the effect of gating the integrate-and-dump on for $\xi T_s/2$ sec at the beginning and end of the symbol interval and twice as long at the mid-symbol position. According to MAP estimation theory, the fractional "window width," ξ, should be chosen as small as possible. From a practical standpoint, however, we shall soon see that other considerations are involved in the selection of its value. In the second case, the same cross-correlation reference signal would appear as in Fig. 3-4b. Here, the edge gates overlap two adjacent symbols.

Regardless of which impulse function approximation is adopted, in a practical symbol synchronizer implementation, the running accumulator could be replaced by a digital filter whose memory is chosen relative to the value of K (Ref. 6). Whereas, the input to the bumped phase oscillator was a linear combination of the previous K+1 outputs of the multiplier, we now have an accumulation of the infinite past of these quantities each weighted by the impulse response of the digital filter. By adjusting the memory of this filter, the input to the bumped phase oscillator can be made to essentially reflect only the previous K+1 multiplier outputs. Since in practice the signal epoch will never remain constant in time, a weighted sum of the data that accentuates the recent symbols and attenuates the others should be more appropriate than a

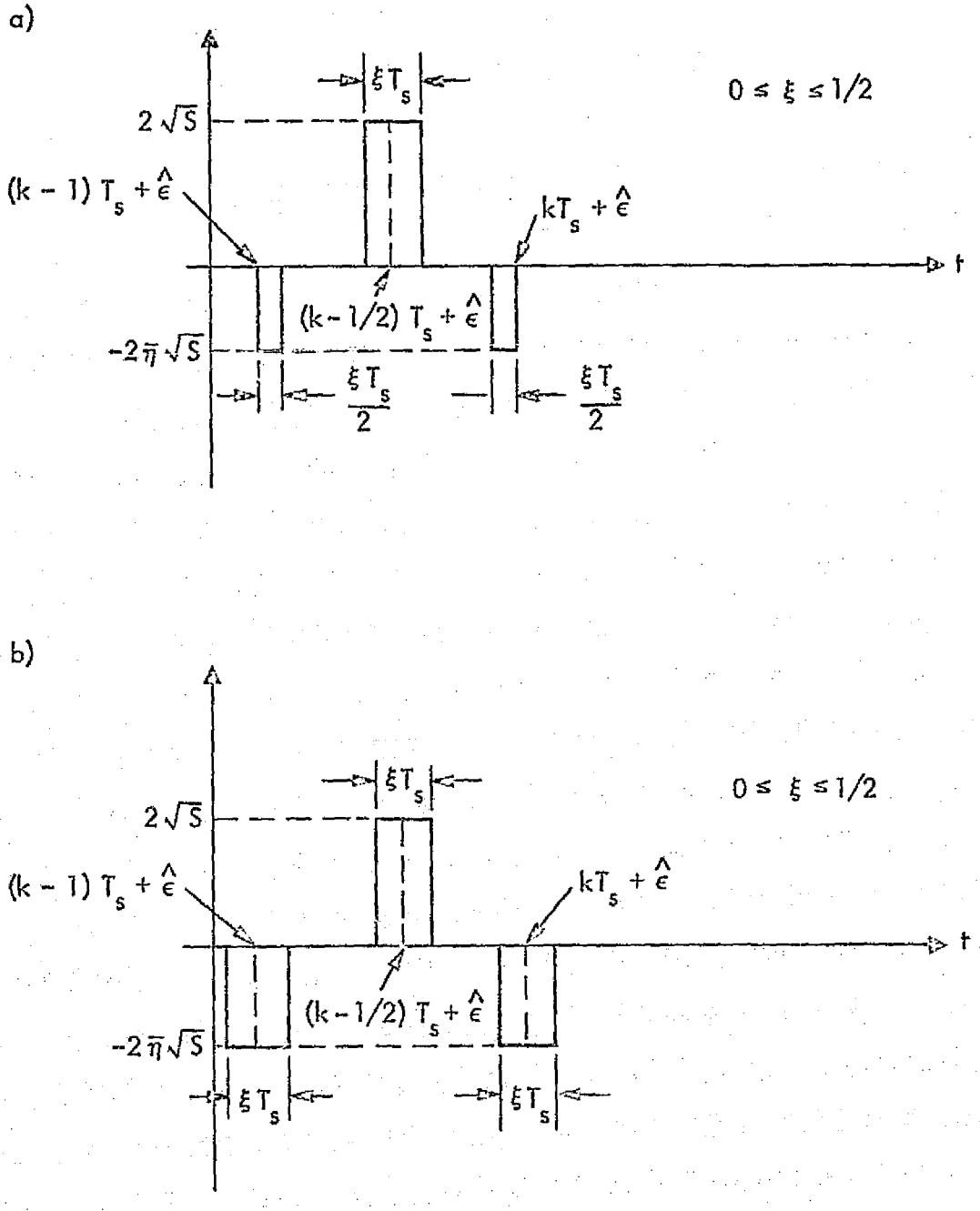

Fig. 3-4. Practical Approximations to the Derivative of the Manchester Symbol Pulse.

pure linear combination; thus, the motivation for using a digital filter.

3.3 Steady-State Performance of Symbol Synchronizer Implementations Motivated by the MAP Estimation Approach

On the basis of the foregoing information, we propose to study the steady-state tracking performance of the symbol synchronizer implementations in Fig. 3-5. Those in Figs. 3-5a and 3-5b are based on the approximation of Fig. 3-4a while those in Figs. 3-5c and 3-5d make use of the approximation of Fig. 3-4b. The techniques which will be employed in carrying out this study are analogous to those given in Ref. 1 where they are used to characterize the performance of symbol synchronizers with NRZ inputs. Namely, under the assumptions that the input timing offset ϵ is essentially constant over a large number of symbols and that the loop response is very slow with respect to a symbol interval ($W_L T_s \ll 1$ where W_L is the two-sided loop bandwidth), the symbol synchronizers of Fig. 3-4 can be modeled as the continuous phase-locked loop given in Fig. 3-6. Developing the equivalence between Fig. 3-5 and Fig. 3-6 relies on finding 1) the average loop S-curve $g(\lambda)$ as a function of the normalized timing $\lambda = (\epsilon - \hat{\epsilon})/T_s$ and 2) the two-sided spectral density $S(\omega, \lambda)$ of the equivalent additive noise $n_\lambda(t)$. Once having determined these quantities, the steady-state performance can be found by application of the Fokker-Planck equation.

The approach taken in finding $g(\lambda)$ and $S(\omega, \lambda)$ follows that given in Refs. 1, 7, and 10. In particular, if one replaces the samplers in Fig. 3-5 by sample-and-hold circuits, then the input to the digital filter becomes the continuous staircase-type waveform e(t) defined by

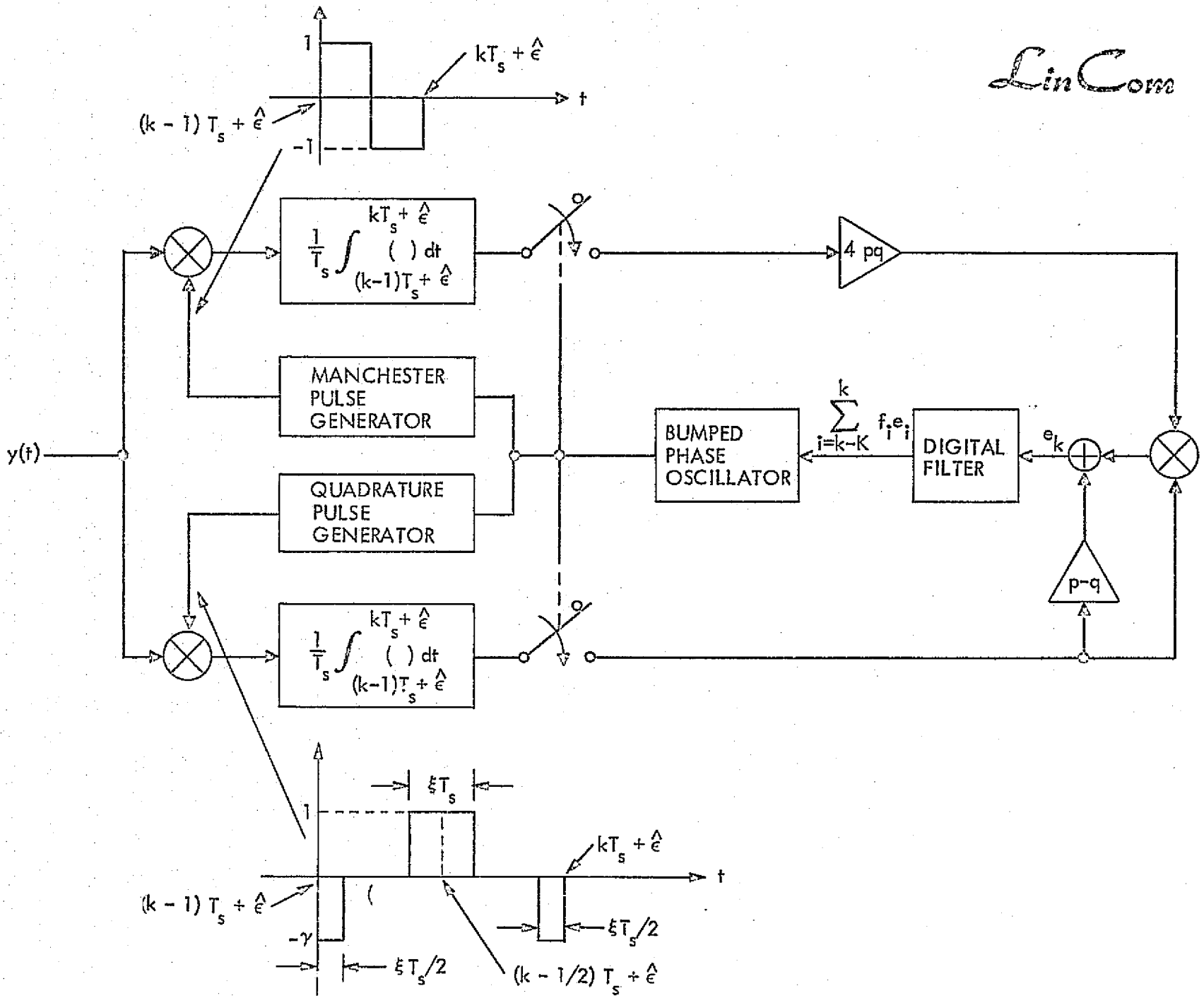

Fig. 3-5a. Symbol Synchronizer for Manchester Coded Data (Large Signal-to-Noise Ratio).

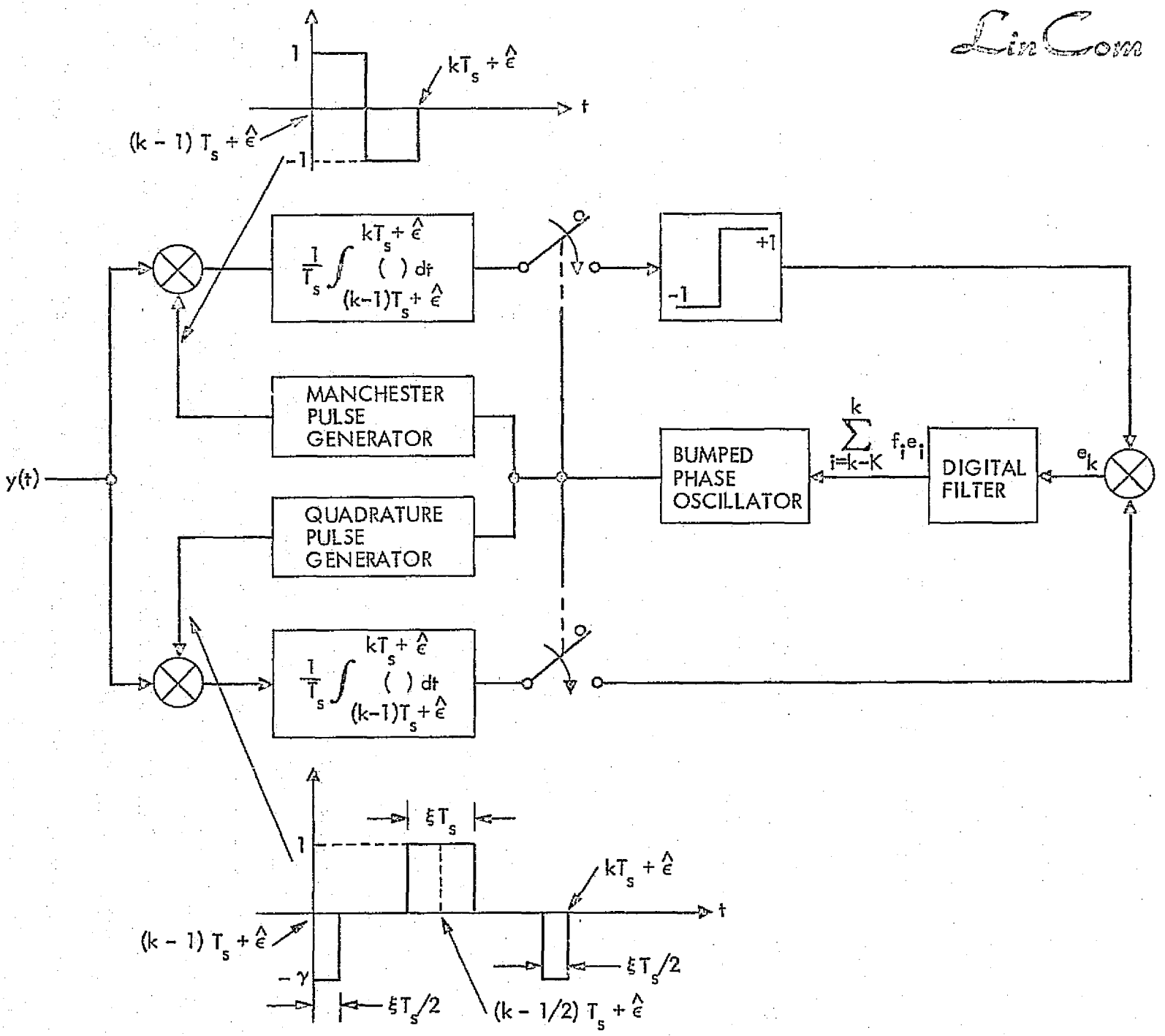

Fig. 3-5b. Symbol Synchronizer for Manchester Coded Data (Small Signal-to-Noise Ratio).

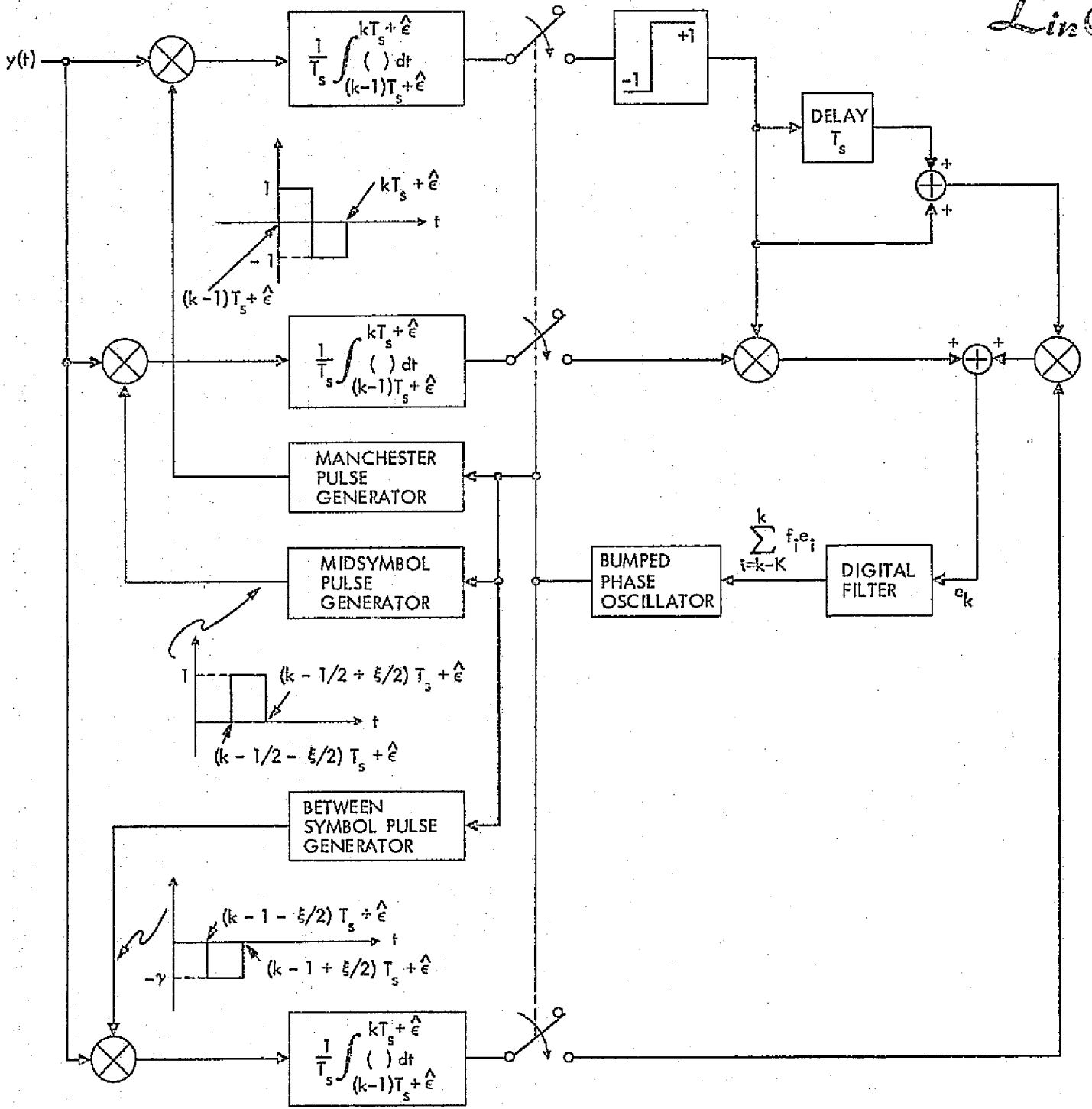

Fig. 3-5c. Symbol Synchronizer for Manchester Coded Data (Large Signal-to-Noise Ratio).

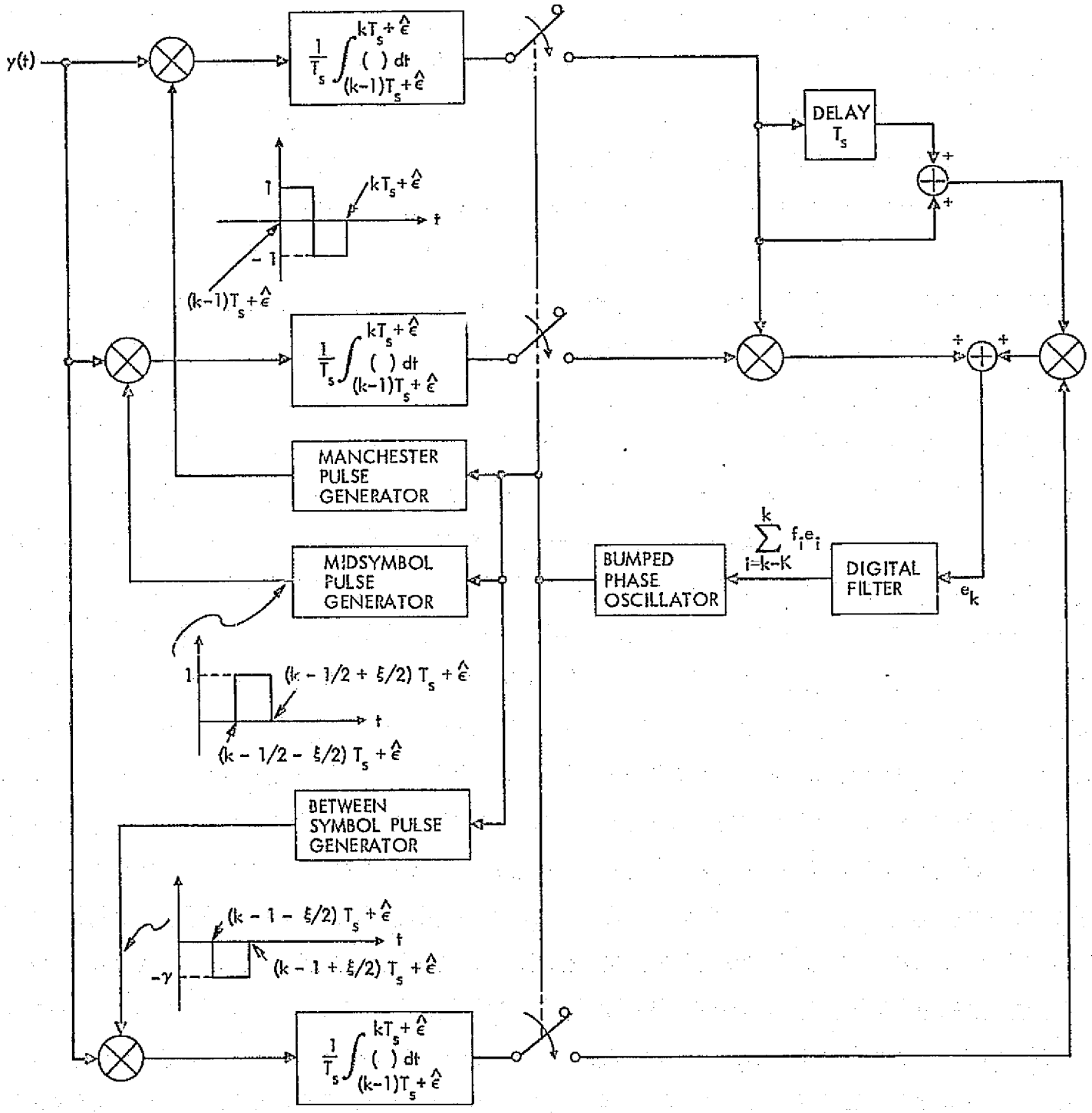

Fig. 3-5d. Symbol Synchronizer for Manchester Coded Data (Small Signal-to-Noise Ratio).

$$e(t) = e_k \qquad kT+\hat{\epsilon} \le t \le (k+1)T + \hat{\epsilon} \tag{8}$$

whose statistical mean conditioned on fixed λ is $g(\lambda)$ and whose power spectral density conditioned on fixed λ is $S(\omega, \lambda)$. Mathematically speaking,

$$g(\lambda) \triangleq E_{n,s}\{e(t)|\lambda\} = E_{n,s}\{e_k|\lambda\}$$

$$n_\lambda(t) \triangleq e(t) - g(\lambda)$$

$$S(\omega, \lambda) \triangleq \mathcal{F}\{\langle R(t, \tau;\lambda)\rangle\}\ ;\ R(t, \tau;\lambda) = E_{n,s}\{n_\lambda(t)n_\lambda(t+\tau)|\lambda\} \tag{9}$$

where $E_{n,s}$ represents the conditional expectation on λ both with respect to the noise and the signal (symbol sequence), the symbol $\mathcal{F}$ denotes the Fourier transform operation, and the symbol $\langle\ \rangle$ denotes time average. Furthermore, to evaluate the autocorrelation $\langle R(t, \tau;\lambda)\rangle$, it is sufficient to determine the discrete function $R_0(m, \lambda)$; $m = 0, \pm1, \pm2, \ldots$ defined by

$$R_0(m, \lambda) = E_{n,s}\{e_k e_{k+m}|\lambda\} - g^2(\lambda) \tag{10}$$

Then, since $n_\lambda(t)$ is conditionally cyclostationary (i.e. its autocorrelation function $R(t, \tau;\lambda)$ is, for fixed τ and λ, periodic in t with period T_s, we have

$$\langle R(t, \tau;\lambda)\rangle = R_0(m, \lambda) + \frac{R_0(m+1, \lambda)-R_0(m, \lambda)}{T_s}(\tau - mT_s); \tag{11}$$

$$mT_s \le \tau \le (m+1)T_s$$
$$m = 0, \pm1, \pm2, \ldots$$

The autocorrelation function $R_0(m, \lambda)$ has the following properties:

(1) $R_0(m, \lambda)$ has nonzero value only at $m = 0, \pm1$. This is a consequence of the independence assumption made regarding the data symbols.

(2) $R_0(m, \lambda) = R_0(-m, \lambda)$.

Thus, Eq. (9) combined with (10) simplifies to

$$S(\omega, \lambda) = 2\int_0^{2T_s} \langle R(t, \tau; \lambda) \rangle \cos \omega\tau d\tau$$

$$= 2\int_0^{T_s} \left[R_0(0, \lambda) + \frac{R_0(1, \lambda) - R_0(0, \lambda)}{T_s} \tau \right] \cos \omega\tau d\tau$$

$$+ 2\int_{T_s}^{2T_s} \left[R_0(1, \lambda) - \frac{R_0(1, \lambda)}{T_s} (\tau - T_s) \right] \cos \omega\tau d\tau \qquad (12)$$

Since, as before, it is assumed that $W_L T_s \ll 1$, it is sufficient then to consider only the value of $S(\omega, \lambda)$ at zero frequency--that is, $S(0, \lambda)$--and assume a flat spectrum of this value for all ω of interest. From (12), we get

$$S(0, \lambda) = T_s [R_0(0, \lambda) + 2R_0(1, \lambda)] \qquad (13)$$

Furthermore, since in any practical system little data degradation due to imperfect symbol sync can be tolerated, then extreme accuracy is required in establishing symbol synchronization. Since this implies very large loop signal-to-noise ratios, then the value of $S(0, \lambda)$ is essentially the noise spectral density seen by the loop at $\lambda = 0$, viz., $S(0, 0)$, see Ref. 1, Ch. 9.

3.4 Application of the Fokker-Planck Technique to Obtain Performance

The stochastic differential equation which describes the loop illustrated in Fig. 3-6 is

$$\dot{\lambda} = -K_v F(p) [g(\lambda) + n_\lambda(t)] \qquad (14)$$

where p is the Heaviside operation and the dot denotes differentiation with respect to time. In writing the above, we have assumed

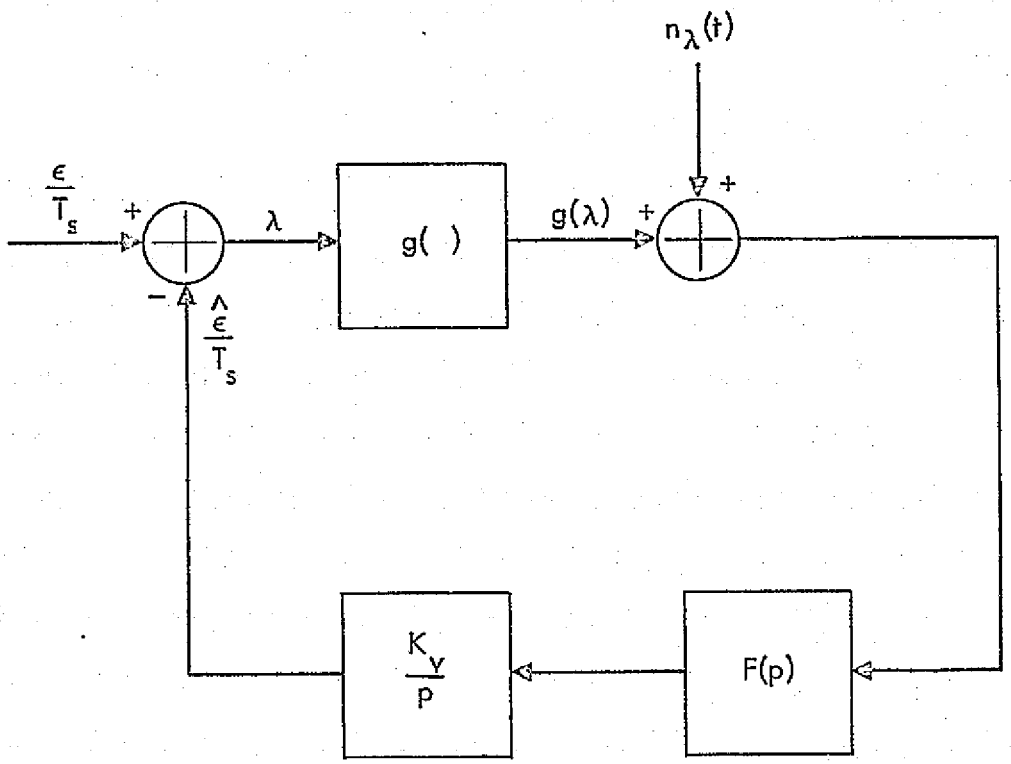

Fig. 3-6. Equivalent Mathematical Model of a Phase-Locked Loop with Arbitrary Periodic Nonlinearity.

zero static timing error which is consistent with our previous assumption that $\dot{\varepsilon}(t) \cong 0$.

In dealing with equations of the above form one can, at best, hope to find the probability distribution of $\lambda(t)$, viz., $p(\lambda, t)$ from which the mean-squared timing jitter $\sigma_\lambda^2(t)$ can be calculated. Under the assumptions previously made regarding the equivalent additive noise process $n_\lambda(t)$, the solution for $p(\lambda, t)$ can be found via the Fokker-Planck method. In particular, for the first-order loop case, i.e. $F(p) = 1$, $\lambda(t)$ is a first-order Markov process whose probability density function satisfies the diffusion equation; Ref. 1,*

$$\frac{\partial p(\lambda_0, t)}{\partial t} + \frac{\partial}{\partial \lambda_0}\left[K_1(\lambda_0, t)p(\lambda_0, t)\right] = \tfrac{1}{2}\frac{\partial^2}{\partial \lambda_0^2}\left[K_2(\lambda_0, t)p(\lambda_0, t)\right] \quad (15)$$

where $K_1(\lambda_0, t)$ and $K_2(\lambda_0, t)$ are defined by the conditional expectations

$$K_1(\lambda_0, t) = \lim_{\Delta t \to 0} \frac{1}{\Delta t} E\{[\lambda(t+\Delta t) - \lambda(t)] \,|\, \lambda(t) = \lambda_0\} \quad (16)$$

$$K_2(\lambda_0, t) = \lim_{\Delta t \to 0} \frac{1}{\Delta t} E\{[\lambda(t+\Delta t) - \lambda(t)]^2 \,|\, \lambda(t) = \lambda_0\} \quad (17)$$

Of interest is the case where $p(\lambda, t)$ converges to with time to a stationary probability density function independent of the initial condition, which can be used to evaluate the steady-state behavior of the symbol synchronizer. Denoting

$$p(\lambda) = \lim_{t \to \infty} p(\lambda, t) \quad (18)$$

*In terms of the time discrete symbol synchronizer configurations of Fig. 3-5, the first-order loop assumption is equivalent to assuming a digital filter with unity weighting coefficients.

we obtain from (15) the stationary equation

$$\frac{\lambda}{d\lambda}\left[K_1(\lambda)p(\lambda)\right] = \tfrac{1}{2}\frac{d^2}{d\lambda^2}\left[K_2(\lambda)p(\lambda)\right] \tag{19}$$

where from (9), (13), and (14), we obtain

$$K_1(\lambda) = -K_v g(\lambda)$$

$$K_2(\lambda) = K_v^2 S(0,\lambda) \cong K_v^2 S(0,0) \tag{20}$$

Substituting (20) into (19), and solving, gives the probability density function

$$p(\lambda) = C_1 \exp\left[-\frac{2\int g(\lambda)d\lambda}{K_v S(0,0)}\right] ; \quad 0 \le \lambda \le \tfrac{1}{2}$$

$$p(-\lambda) = p(\lambda) \tag{21}$$

where C_1 is a normalization constant chosen such that

$$\int_{-\frac{1}{2}}^{\frac{1}{2}} p(\lambda)d\lambda = 1 \tag{22}$$

Now for large group signal-to-noise ratios, $g(\lambda)$ can be approximated by

$$g(\lambda) = \begin{cases} \sqrt{S}\,K_g\lambda & \text{(Fig. 3-5a)} \quad (23a) \\ STK_g\lambda & \text{(Fig. 3-5b)} \quad (23b) \\ \sqrt{S}\,K_g\lambda & \text{(Fig. 3-5c)} \quad (23c) \\ STK_g\lambda & \text{(Fig. 3-5d)} \quad (23d) \end{cases}$$

where K_g is the slope of the normalized S-curve, $g_n(\lambda)$, at the origin. Then defining the ratio of symbol rate $R_s = 1/T_s$ to

single-sided loop bandwidth $W_L/2$ by

$$\delta_s = \frac{2R_s}{W_L} \tag{24}$$

we have for large $R_s\delta_s$ (but necessarily large R_s) that

$$\sigma_\lambda^2 \triangleq \int_{-\frac{1}{2}}^{\frac{1}{2}} \lambda^2 p(\lambda)d\lambda = \begin{cases} \dfrac{2S(0,0)/N_0}{R_s\delta_s K_g^2} & \text{(Fig. 3-5a)} \quad (25a) \\ \dfrac{2S(0,0)/N_0^2T}{R_s^2\delta_s K_g^2} & \text{(Fig. 3-5b)} \quad (25b) \\ \dfrac{2S(0,0)/N_0}{R_s\delta_s K_g^2} & \text{(Fig. 3-5c)} \quad (25c) \\ \dfrac{2S(0,0)/N_0^2T}{R_s^2\delta_s K_g^2} & \text{(Fig. 3-5d)} \quad (25d) \end{cases}$$

The value of symbol edge gate amplitude γ (see Fig. 3-5) may now be selected to minimize σ_λ^2. Differentiating (25) with respect to γ and equating to zero gives

$$\gamma_{opt} = \begin{cases} 1-2pq & \text{(Fig. 3-5a)} \quad (26a) \\ 1-2pq & \text{(Fig. 3-5b)} \quad (26b) \\ \dfrac{2(1-2pq)-\xi(2pq)\sqrt{(R_s)/\pi}\exp(-R_s)/\operatorname{erf}\sqrt{R_s}}{1+\xi R_s(2pq)\left[1-\operatorname{erf}^2\sqrt{R_s}\right]-2\xi(2pq)\sqrt{\frac{R_s}{\pi}}\exp(-R_s)\operatorname{erf}\sqrt{R_s}-\frac{\xi}{2\pi}\exp^2(-R_s)} & \text{(Fig. 3-5c)} \quad (26c) \\ \dfrac{2(1+2R_s)\left[(1-2pq)-\frac{1}{4}\xi(2pq)\right]}{1+4(1-2pq)R_s-\frac{1}{4}\xi\left[1+4(2pq)R_s\right]} & \text{(Fig. 3-5d)} \quad (26d) \end{cases}$$

Note that the value of γ which minimizes σ_λ^2 for Fig. 3-5a and Fig. 3-5b is independent of R_s and is identical to the value of $\overline{\eta}$ [see Eq. (7)] suggested by the MAP estimation theory. The values of γ_{opt} for Figs. 3-5c and 3-5d are, in general, functions of R_s, ξ and $2pq$. Fig. 3-7 illustrates γ_{opt} of Eq. (26c) vs R_s for fixed ξ and $p_t \triangleq 2pq$ as a parameter. Keeping in mind that Fig. 3-5c is intended for use at large signal-to-noise ratios, we note from Fig. 3-7 that over a wide range of R_s, γ_{opt} can well be approximated by its value at $R_s = \infty$, i.e.

$$\gamma_{opt}\Big|_{R_s=\infty} = 2(1-2pq) \tag{27}$$

Again, note the similarity with the result predicted by the MAP estimation theory. Fig. 3-8 is a similar plot to Fig. 3-7 for γ_{opt} as given by (26d). Here we see that over a similar range of small signal-to-noise ratios, γ_{opt} is well approximated by its value at $R_s = 0$, i.e.

$$\gamma_{opt}\Big|_{R_s=0} = \frac{2\left[(1-2pq)-\frac{1}{4}\xi(2pq)\right]}{1-\frac{\xi}{4}} \tag{28}$$

From (25) and (26) we see that a comparison of the various symbol synchronizer configurations on the basis of minimum mean-squared timing jitter $\sigma_{\lambda_{min}}^2$ can be achieved by studying the behavior of the two ratios

$$\frac{(\sigma_{\lambda_{min}}^2)_a}{(\sigma_{\lambda_{min}}^2)_c} = \frac{r_H(\xi, R_s, 2pq)}{1+(1-2pq)^2} \tag{29}$$

and

$$\frac{(\sigma_{\lambda_{min}}^2)_b}{(\sigma_{\lambda_{min}}^2)_d} = \frac{r_L(\xi, R_s, 2pq)}{1+(1-2pq)^2} \tag{30}$$

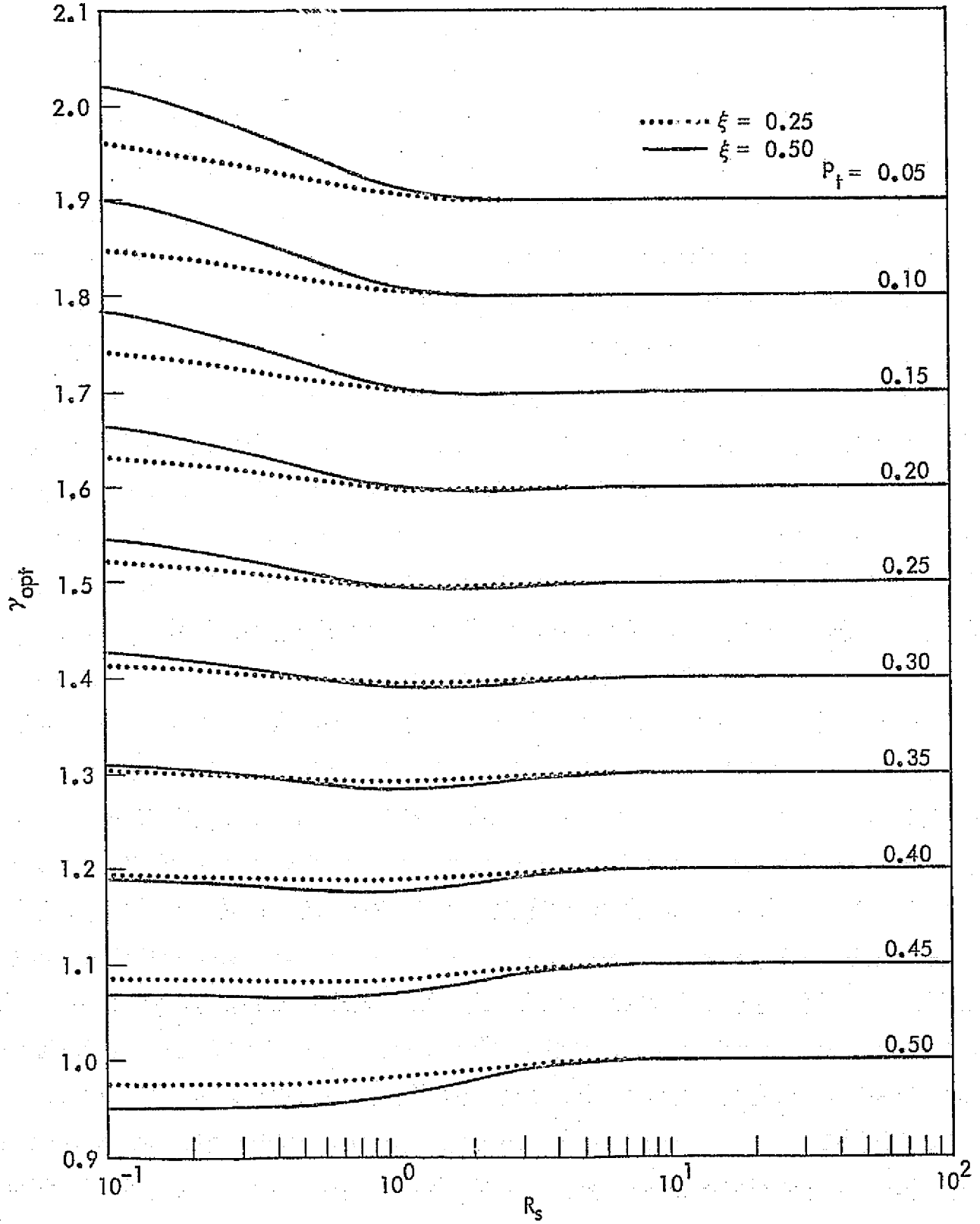

Fig. 3-7. Optimum γ vs R_s for ξ Fixed and Transition Density as a Parameter (Large Signal-to-Noise Ratio Case).

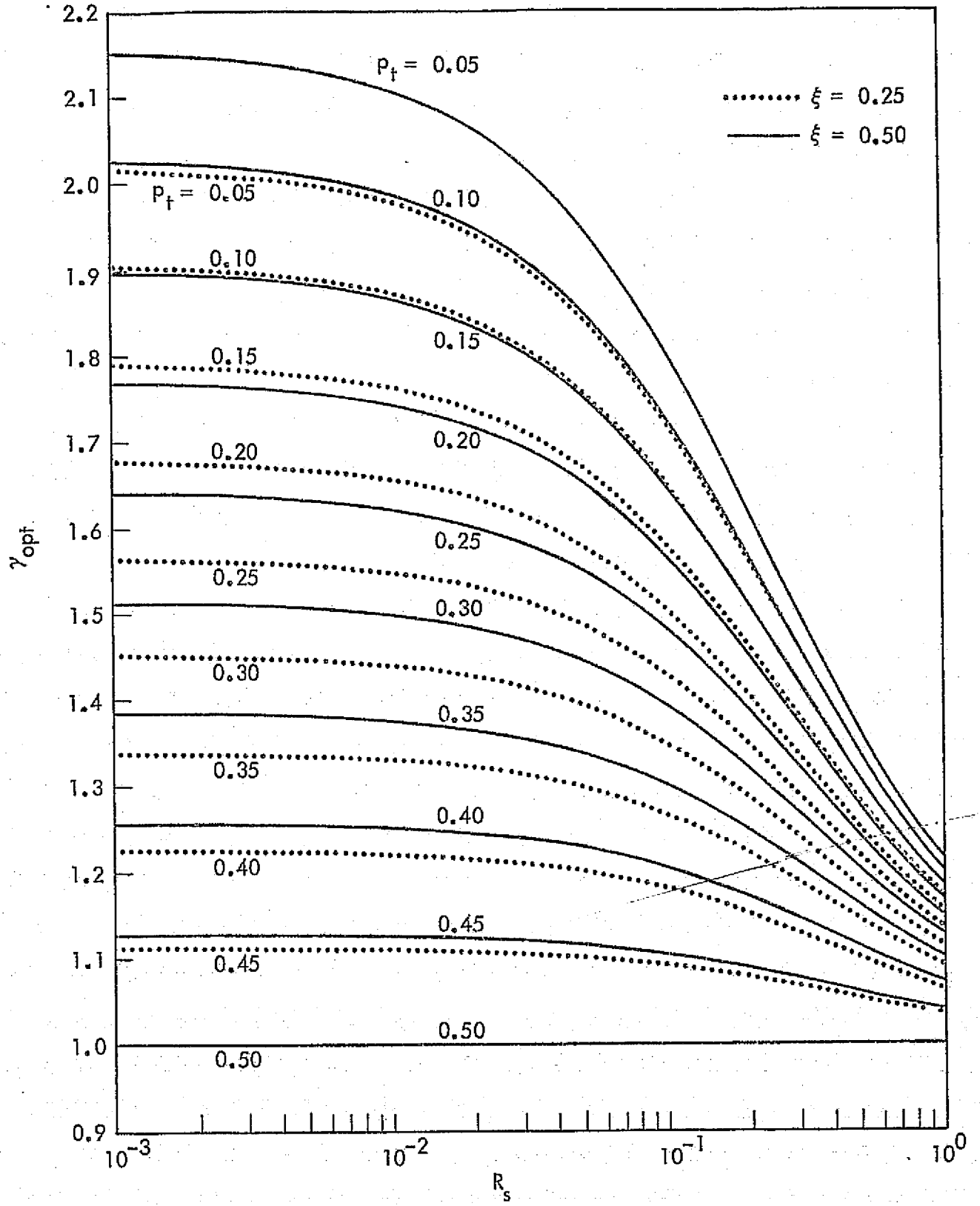

Fig. 3-8. Optimum γ vs. R_s for ξ Fixed and Transition Density as a Parameter (Small Signal-to-Noise Ratio Case).

where

$$r_H(\xi, R_s, 2pq) \triangleq 1 + \frac{\left[(1-2pq)\operatorname{erf}\sqrt{R_s} - \frac{1}{2}\xi(2pq)\sqrt{\frac{R_s}{\pi}}\exp(-R_s)\right]^2}{\operatorname{erf}^2\sqrt{R_s}\left\{\frac{1}{2}+\frac{1}{2}\xi R_s(2pq)\left[1-\operatorname{erf}^2\sqrt{R_s}\right]+\xi(2pq)\sqrt{\frac{R_s}{\pi}}\exp(-R_s)\operatorname{erf}\sqrt{R_s} - \frac{\xi}{4\pi}\exp^2(-R_s)\right\}} \tag{31a}$$

$$r_L(\xi, R_s, 2pq) \triangleq 1 + \frac{2(1+2R_s)\left[(1-2pq) - \frac{1}{4}\xi(2pq)\right]^2}{1 + 4(1-2pq)R_s + \frac{1}{4}\xi\left[1 + 4(2pq)R_s\right]} \tag{31b}$$

Figs. 3-9 and 3-10 illustrate these two ratios (in dB) as a function of R_s with ξ fixed and $p_t = 2pq$ as a parameter. We observe from Fig. 3-9 that over a large range of values for R_s, ξ, and p_t, the minimum mean-squared timing jitter associated with the synchronizer implementation of Fig. 3-5a is larger than that associated with Fig. 3-5c. In fact, over a wide range of large signal-to-noise ratios, the ratio given in (29) can be approximated by

$$\frac{(\sigma^2_{\lambda_{min}})_a}{(\sigma^2_{\lambda_{min}})_c} \cong \frac{1 + 2(1-2pq)^2}{1 + (1-2pq)^2} \tag{32}$$

Similarly, from Fig. 3-10, we observe that over the range of parameter values considered, the symbol synchronizer configuration of Fig. 3-5d outperforms that of Fig. 3-5b.

To complete the picture, we compare the mean-squared jitter performance of Fig. 3-5a with Fig. 3-5b and Fig. 3-5c with Fig. 3-5d so as to determine their relative behavior in the region between small and large signal-to-noise ratios. The motivation behind such a comparison is the fact that in this region of medium signal-to-noise ratios, the appropriate nonlinearity to be used at the output of the in-phase arm integrate-and-dump circuit as

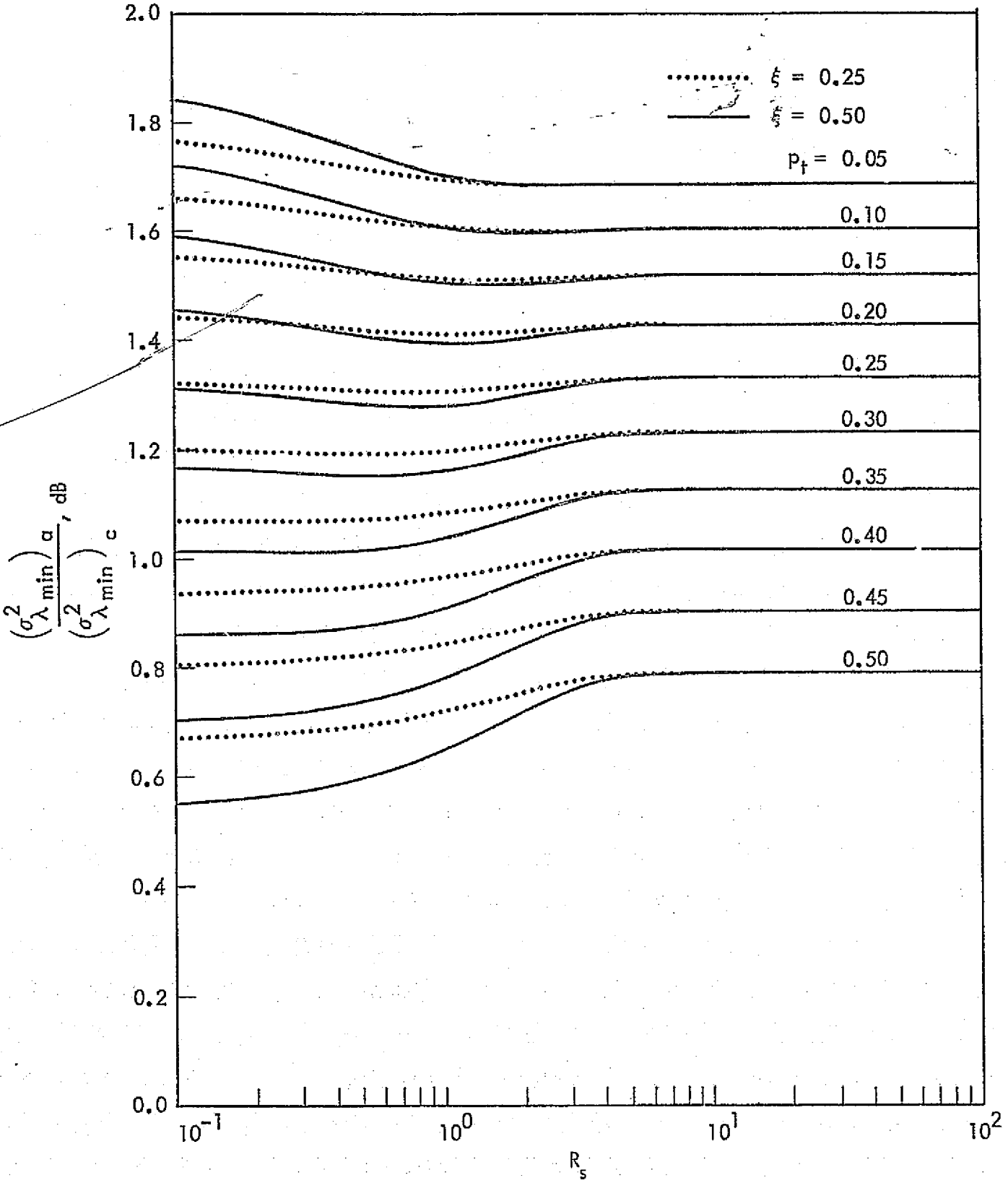

Fig. 3-9. A Comparison of the Mean-Squared Timing Jitter Performance of Figs. 3-5a and 3-5c.

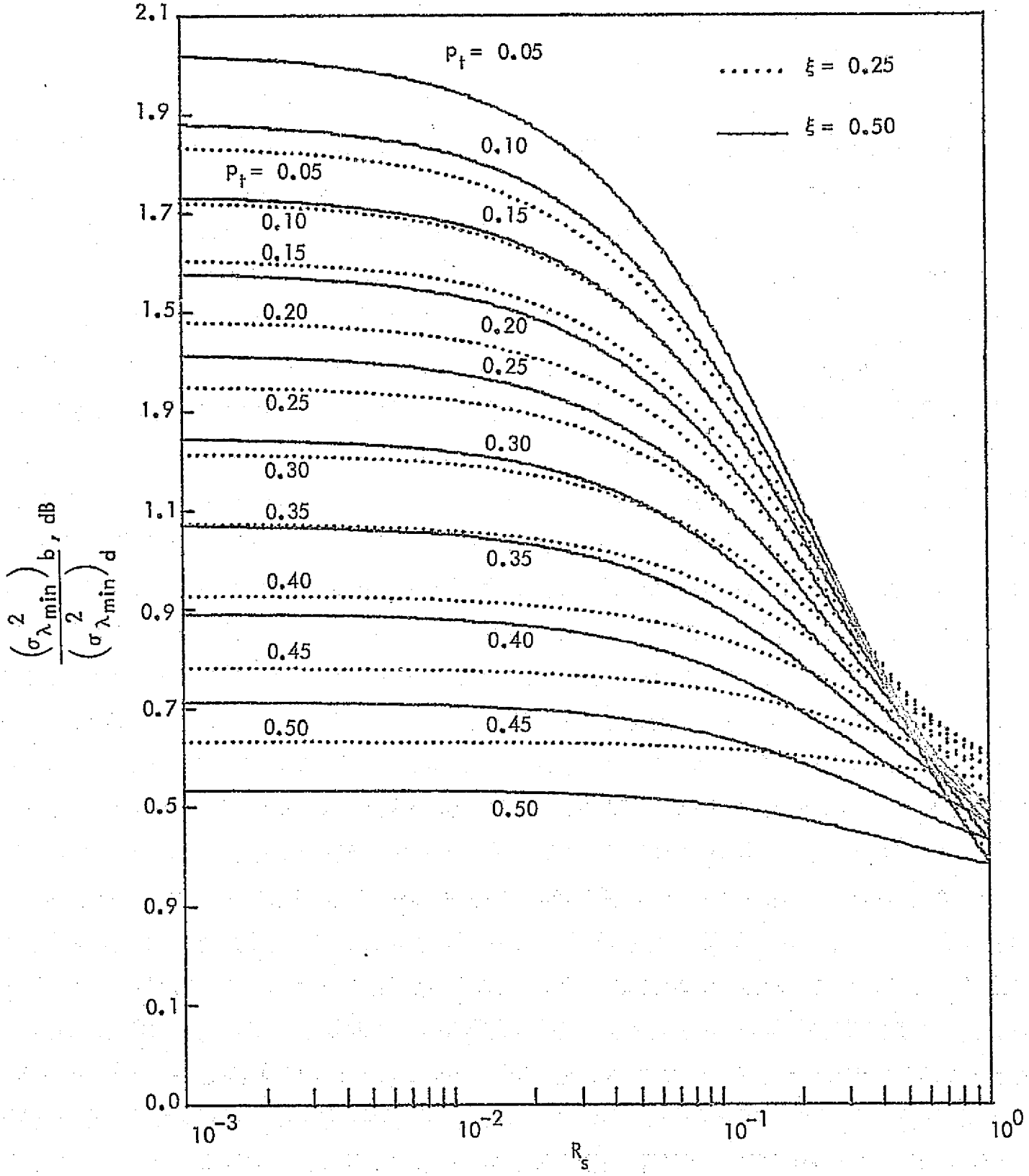

Fig. 3-10. A Comparison of the Mean-Squared Timing Jitter Performance of Figs. 3-5b and 3-5d.

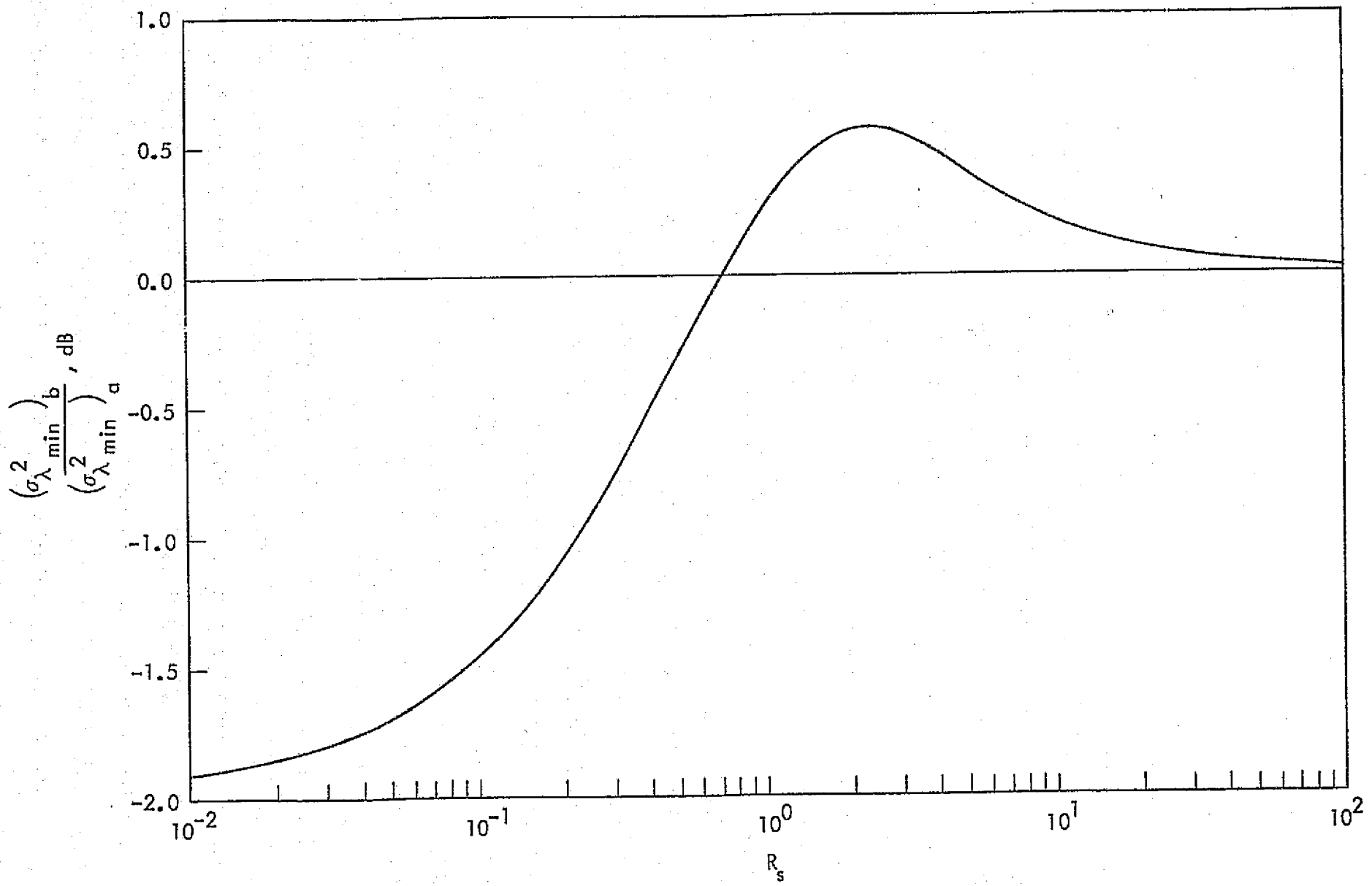

Fig. 3-11. A Comparison of the Mean-Squared Timing Jitter Performance of Figs. 3-5a and 3-5b.

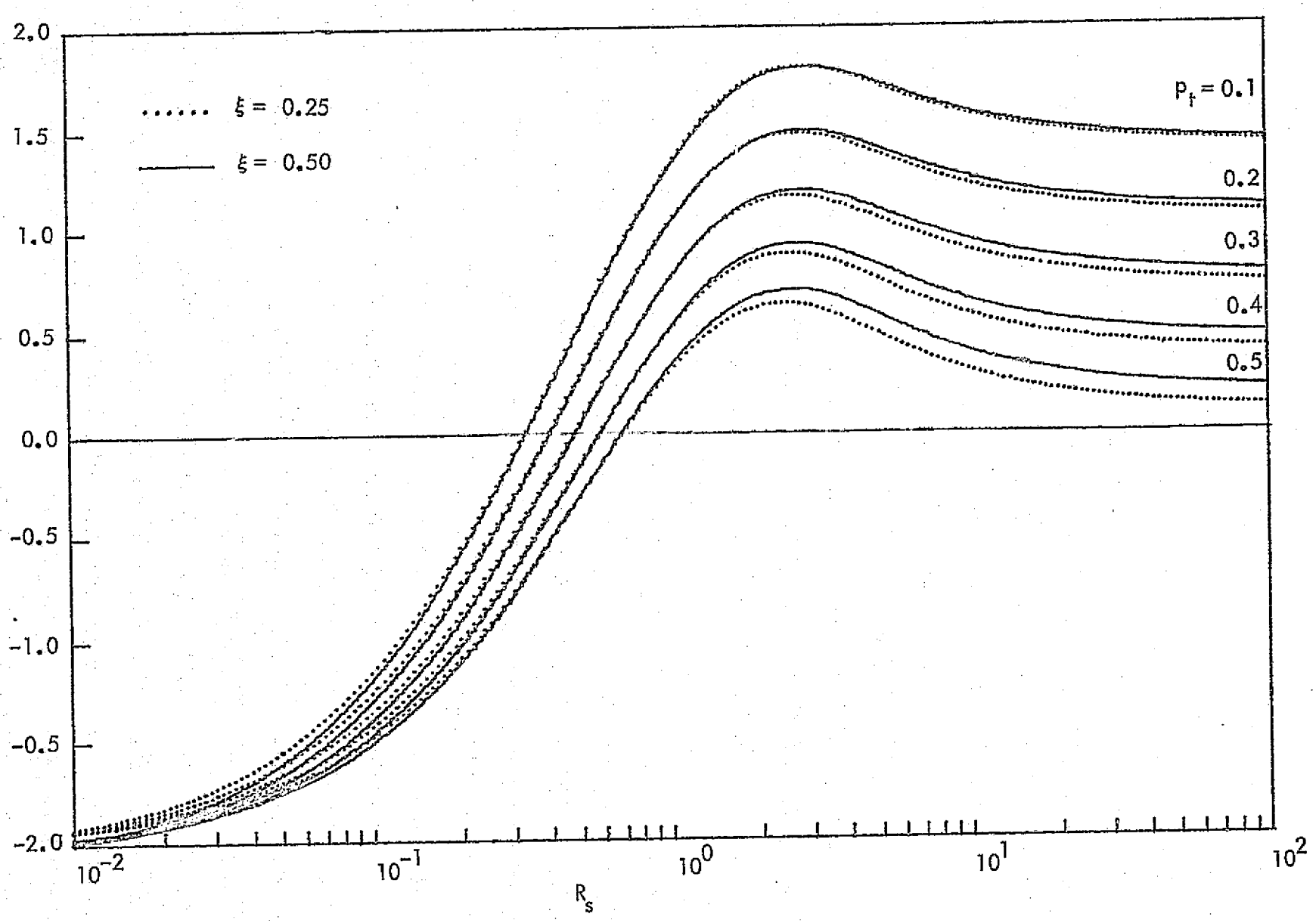

Fig. 3-12. A Comparison of the Mean-Squared Timing Jitter Performance of Figs. 3-5c and 3-5d.

suggested by the MAP estimation theory is neither the signum nor the linear function [see Eq. (4)]. Thus, it is not immediately evident which implementation is preferable in this in-between signal-to-noise ratio region. Figs. 3-11 and 3-12 illustrate, respectively, the ratios $(\sigma^2_{\lambda_{min}})_b/(\sigma^2_{\lambda_{min}})_a$ and $(\sigma^2_{\lambda_{min}})_d/(\sigma^2_{\lambda_{min}})_c$ vs. R_s with ξ and p_t as parameters.

3.5 Further Numerical Results

The S-curves (phase detector characteristics) for the four symbol synchronizer implementations of Fig. 3-5 are illustrated in Figs. 3-13 to 3-16 respectively for $p_t = .5$, various values of window width ξ, and R_s as a parameter. We observe from these illustrations that over a certain range of signal-to-noise ratios, the various loops exhibit a stable lock point which is one half symbol ($\lambda = .5$) away from the desired lock point at $\lambda = 0$. Although, this midsymbol lock point is less probable than the one at $\lambda = 0$, an attempt should be made to resolve it whenever possible. For sufficiently large signal-to-noise ratios, viz., greater than 10 dB, the midsymbol lock point vanishes for the synchronizer implementations of Figs. 3-5a and 3-5c. On the other hand, the S-curves for Figs. 3-5b and 3-5d are (for $p_t = .5$) independent of R_s. For smaller and smaller transition densities, p_t, the S-curves become more and more symmetrical and in the limit of zero transition density, i.e. a square-wave data waveform, the S-curves are periodic with period equal to 1/2, and thus, the midsymbol and desired lock points are equiprobable. Therefore, some form of ambiguity resolution circuit will be required with the use of these phase detectors.

3.6 Cycle Slipping Performance

Up until now, we have treated the normalized timing error process, $\lambda(t)$, in the symbol synchronizer as a stationary

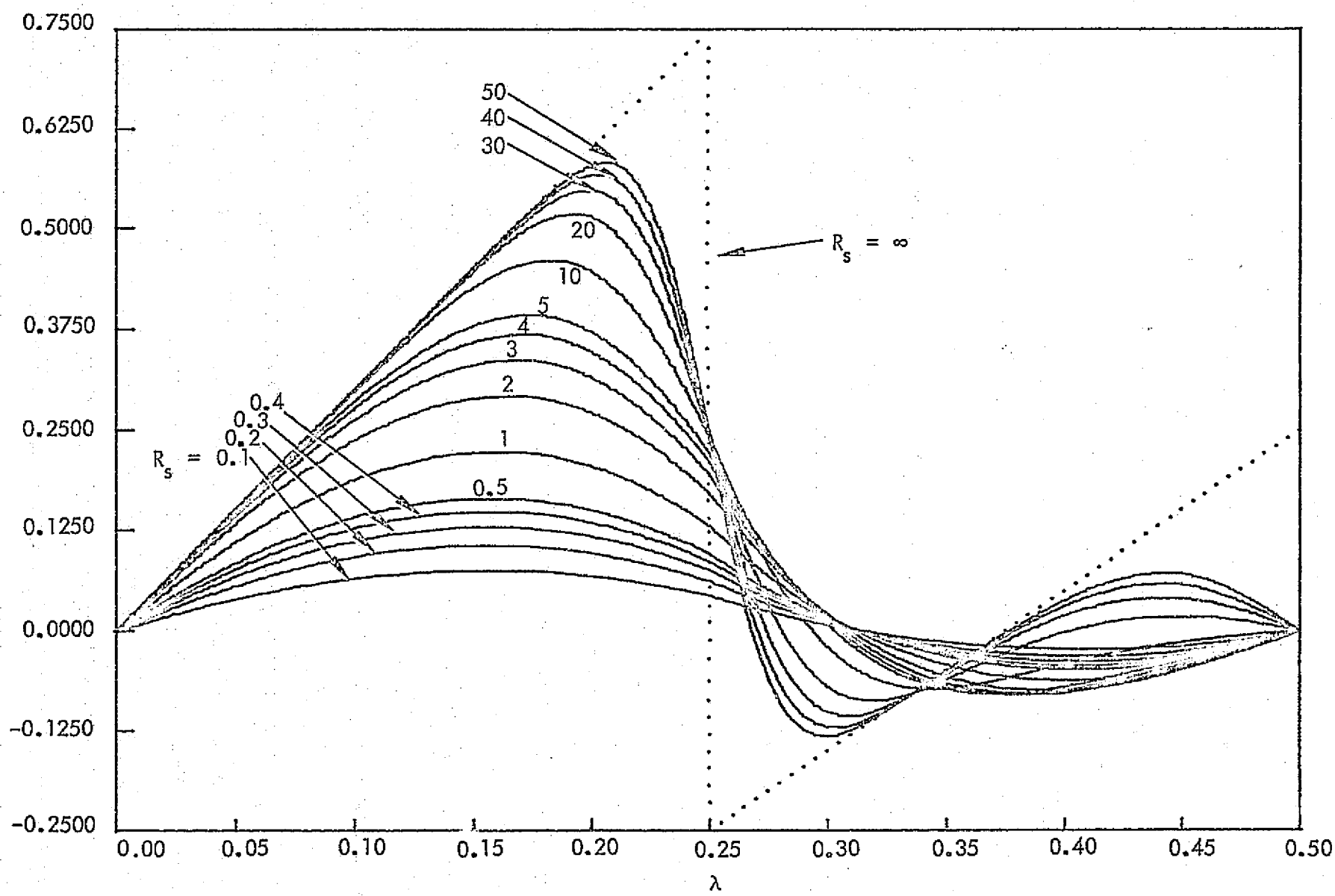

Fig. 3-13a. S-Curves for Symbol Synchronizer of Fig. 3-5a; $p_t = .5$, $\xi = .5$, $\gamma = \gamma_{opt}$.

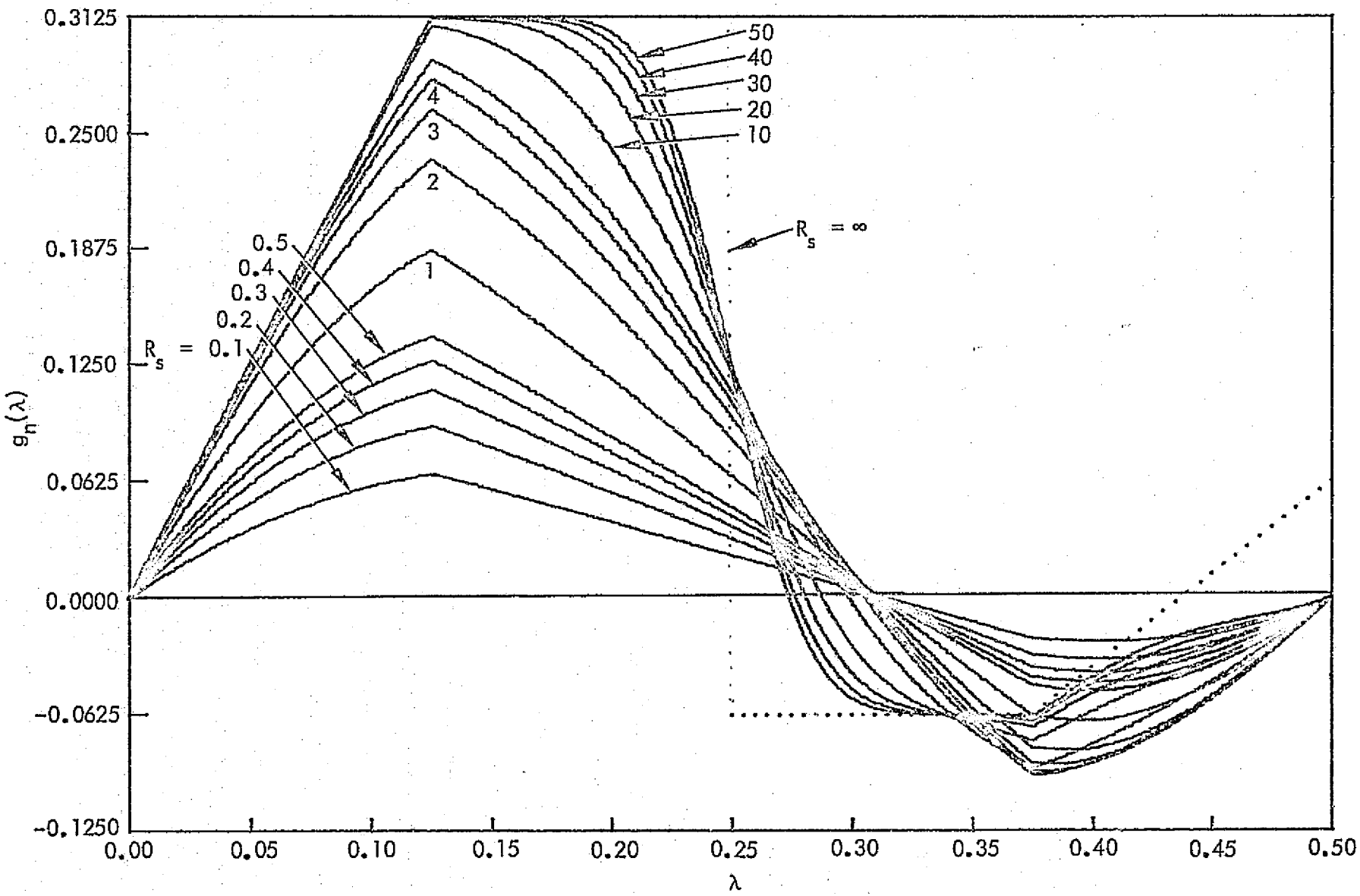

Fig. 3-13b. S-Curves for Symbol Synchronizer of Fig. 3-5a; $p_t = .5$, $\xi = .25$, $\gamma = \gamma_{opt}$.

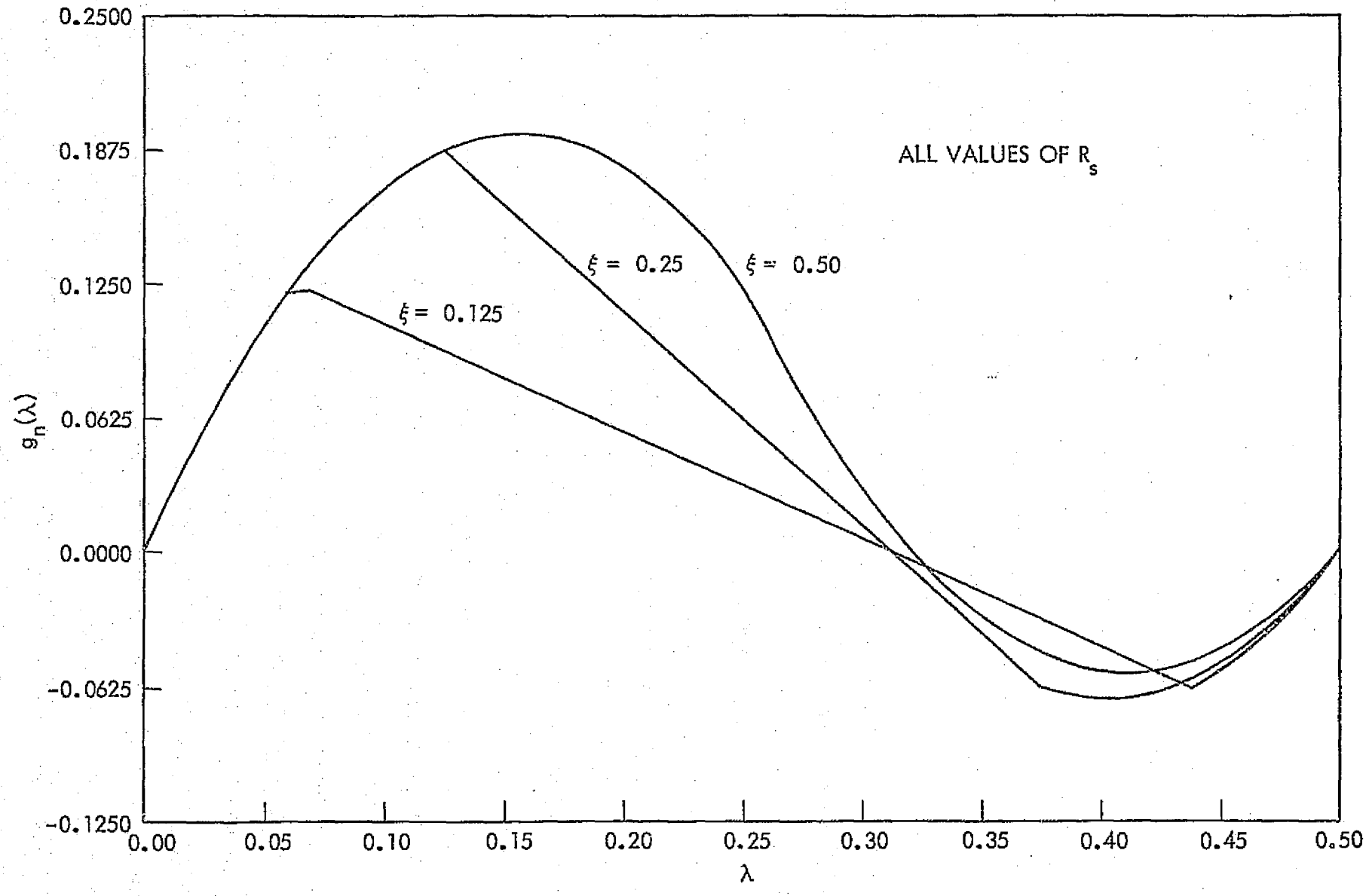

Fig. 3-14. S-Curves for Symbol Synchronizer of Fig. 3-5b; $p_t = .5, \xi = .125, .25, .50$, $\gamma = \gamma_{opt}$.

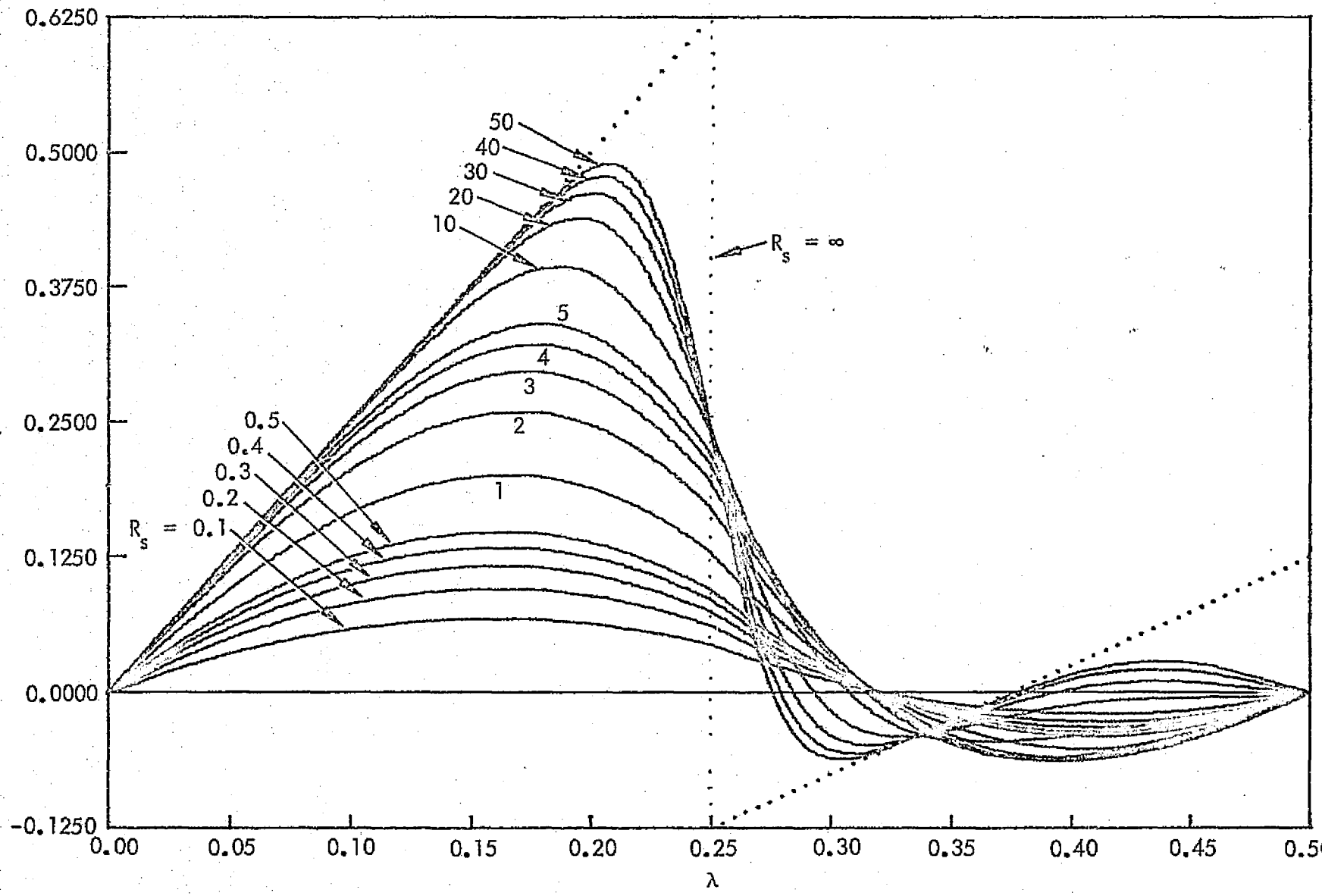

Fig. 3-15a. S-Curves for Symbol Synchronizer of Fig. 3-5c; $p_t = .5$, $\xi = .5$, $\gamma = \gamma_{opt}$.

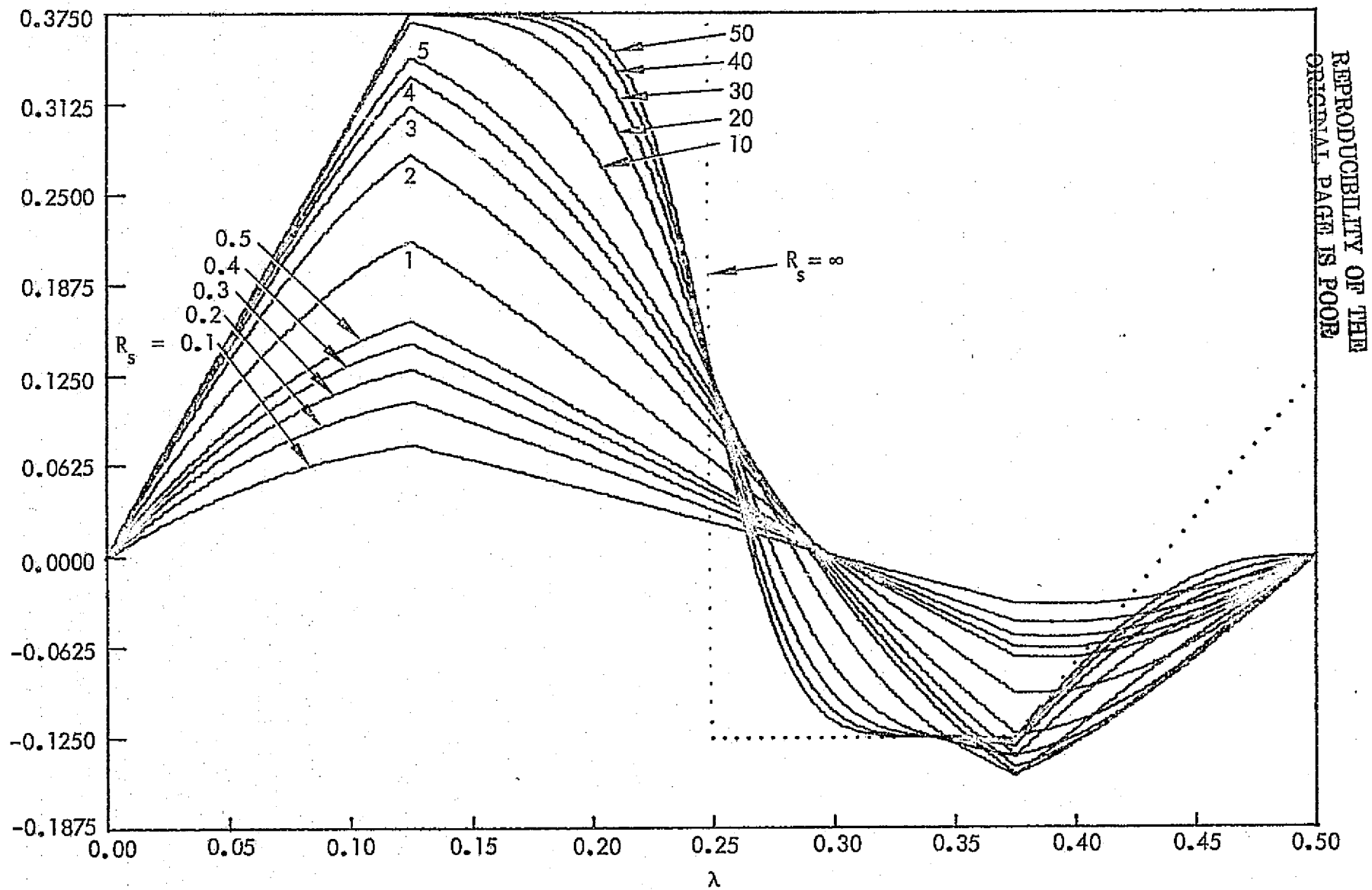

Fig. 3-15b. S-Curves for Symbol Synchronizer of Fig. 3-5c; $p_t = .5$, $\xi = .25$, $\gamma = \gamma_{opt}$.

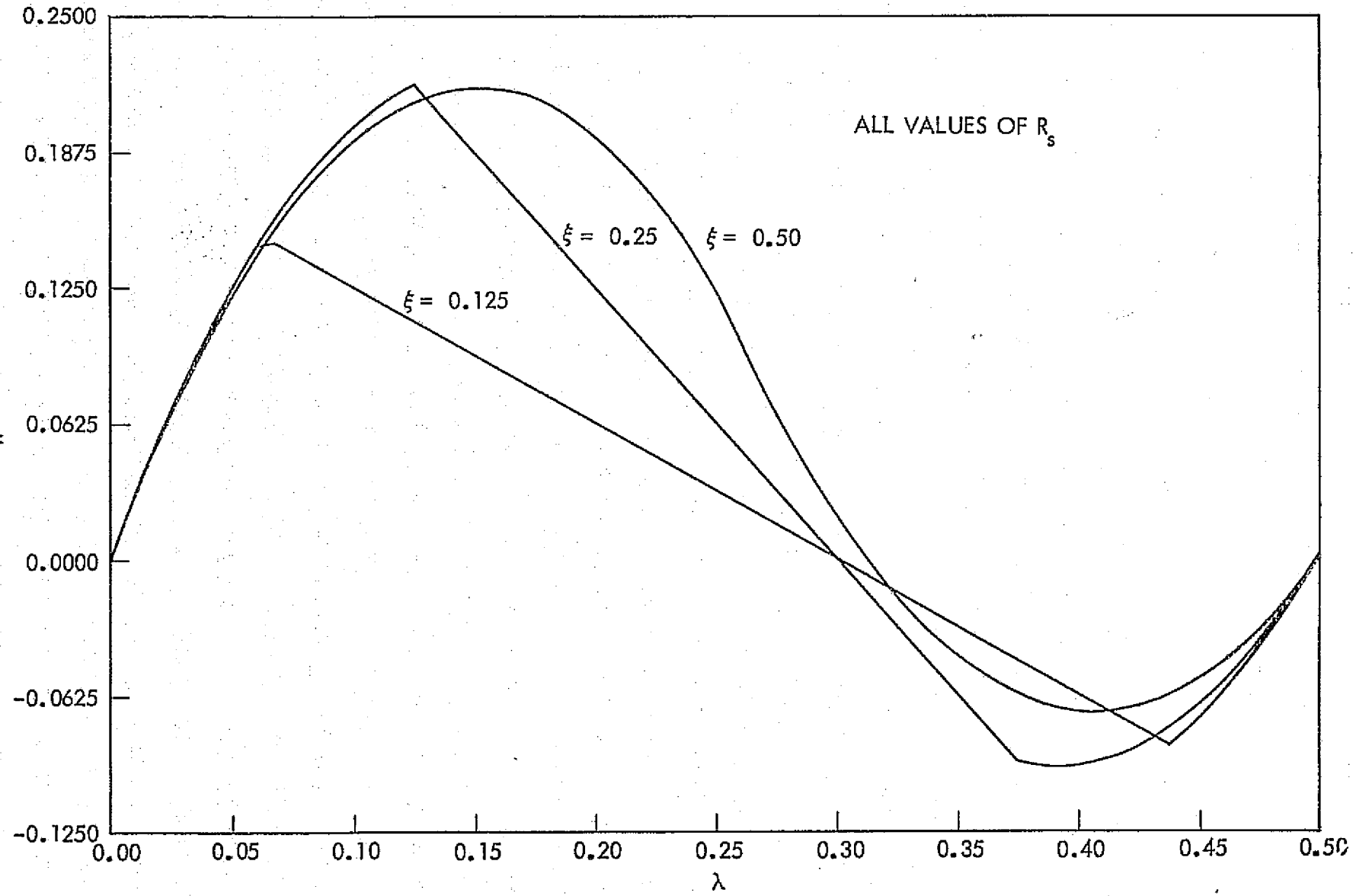

Fig. 3-16. S-Curves for Symbol Synchronizer of Fig. 3-5d; $p_t = .5$, $\xi = .125, .25, .50$, $\gamma = \gamma_{opt}$

process possessing a bounded variance [see Eq. (25)]. This resulted from the fact that we have in reality been discussing the behavior of the timing error reduced modulo T_s, or equivalently, the normalized timing error reduced modulo 1. To completely describe the $\lambda(t)$ process, one must account for the component of its variance that results from diffusion, that is, cycle slipping. The steady-state effect of cycle slipping is perhaps best described by evaluating the diffusion coefficient, that is, the rate at which the variance of the timing error is approaching infinity, or equivalently, the total average rate of cycle slips, $\bar{S}$. The cycle slipping phenomenon in symbol synchronizers is not unlike the same phenomenon in phase-locked loops. In fact, with appropriate normalizations, the expressions for $\bar{S}$ given in Ref. 1 for the phase-locked loop can be easily generated to apply to the symbol synchronizers of Fig. 3-5. In particular, it is straightforward to show that

$$\frac{\bar{S}}{W_L} = \frac{1}{\rho\int_0^{\frac{1}{2}} \exp\left[-\rho\int^{\lambda} g_{n0}(x)dx\right] d\lambda \int_0^{\frac{1}{2}} \exp\left[\rho\int^{\lambda} g_{n0}(x)dx\right] d\lambda} \tag{33}$$

where

$$g_{n0}(\lambda) \triangleq \frac{g_n(\lambda)}{K_g} \tag{34}$$

and

$$\rho \triangleq \frac{1}{2\sigma_{\lambda_{min}}} \tag{35}$$

with $\sigma^2_{\lambda_{min}}$ determined from (25). The expressions for the loop S-curves given in (14) can be integrated in closed form; however, the remaining integrals in (33) must be performed numerically on a digital computer. When this is done, one finds that for all values of $R_s \geq .1$, $\delta_s \geq 100$, $\xi \leq .5$, and $p_t \geq .05$, the normalized

average rate of cycle slipping as computed from (33) is below 10^{-10}. Thus, for most practical applications, cycle slipping will not be a problem.

3.7 Symbol Synchronizer Performance in the Presence of Clock Frequency Offset

In deriving the results given thus far, we have made the assumption that the unknown epoch, $\varepsilon(t)$, of the input symbol data stream is constant with time. Quite often in practice, $\varepsilon(t) = \varepsilon_0 + \varepsilon_1 t/T$. Under these conditions, the stochastic differential equation of (15) becomes

$$\dot{\lambda} = \varepsilon_1 - K_v F(p)[g(\lambda) + n_\lambda(t)] \tag{36}$$

and the symbol synchronizer operates in the presence of a clock frequency offset. Applying the Fokker-Planck technique to (36), we obtain a generalization of (21), namely,

$$p(\lambda) = C_2 \exp\left[\frac{2\varepsilon_1\lambda}{K_v S(0,0)} - \frac{2\int g(\lambda)d\lambda}{K_v S(0,0)}\right] \tag{37}$$

where C_2 is a normalization constant. For large $R_s\delta_s$, the mean-squared timing jitter is still given by (25); however, the stress in the loop caused by ε_1 has, as we shall see shortly, a pronounced effect on symbol error probability performance.

References for Section 3.0

1. Lindsey, W. C., and Simon, M. K., Telecommunication Systems Engineering, Englewood Cliffs, N.J., Prentice-Hall, Inc., 1973, Ch. 9.

2. Stiffler, J. J., Theory of Synchronous Communications, Prentice-Hall, Inc., Englewood Cliffs, N.J., 1971.

3. Stiffler, J. J., "Maximum Likelihood Symbol Synchronization," Jet Propulsion Laboratory, Pasadena, Calif., Rep. SPS 37-35, Vol. IV, Oct. 1965, pp. 349-357.

4. McBride, A. L., and Sage, A. P., "Optimum Estimation of Bit Synchronization," IEEE Trans. Aerosp. Electron. Syst., Vol. AES-5, pp. 525-536, May 1969.

5. Wintz, P. A., and Luecke, E. J., "Performance of Optimum and Suboptimum Synchronizers," IEEE Trans. Commun. Technol., Vol. COM-17, pp. 380-389, June, 1969.

6. Mengali, U., "A Self Bit Synchronizer Matched to the Signal Shape," IEEE Trans. Aerosp. Electron. Syst., Vol. AES-7, pp. 686-693, July, 1971.

7. Lindsey, W. C., and Tausworthe, R. C., "Digital Data-Transition Tracking Loops," Jet Propulsion Laboratory, Pasadena, Calif., Rep. SPS 37-50, Vol. III, Apr. 1968, pp. 272-276.

8. Lindsey, W. C., and Anderson, T. O., "Digital Data-Transition Tracking Loops," in Proc. Int. Telemetering Conf., Los Angeles, Calif., Oct., 1968, pp. 259-271.

9. Tausworthe, R. C., "Analysis and Design of the Symbol-Tracking Loop," Jet Propulsion Laboratory, Pasadena, Calif., Rep. SPS 35-51, Vol. II, May 1968, pp. 145-147.

10. Simon, M. K., "An Analysis of the Steady-State Phase Noise Performance of a Digital Data-Transition Tracking Loop," Jet Propulsion Laboratory, Pasadena, Calif., Rep. SPS-37-55, Vol. III, Feb. 1969, pp. 54-62.

11. Simon, M. K., "Optimization of the Performance of a Digital-Data-Transition Tracking Loop," IEEE Trans. Commun. Technol., Vol. COM-18, pp. 686-689, Oct., 1970.

12. Hurd, W. J., and Anderson, T. O., "Digital Transition Tracking Symbol Synchronizer for Low SNR Coded Systems," IEEE Trans. Commun. Technol., Vol. COM-18, pp. 141-147, Apr. 1970.

13. Simon, M. K., "Nonlinear Analysis of an Absolute Value Type of Early-Late Gate Synchronizer," IEEE Trans. Commun. Technol., Vol. COM-18, pp. 589-596, Oct. 1970.

14. Layland, J. W., "Telemetry Bit Synchronization Loop," Jet Propulsion Laboratory, Pasadena, Calif., Rep. SPS 34-46, Vol. III, pp. 204-215, July 1967.

15. McRae, D. D. and Smith, E. F., "Bit Synchronization," in Proc. Int. Telemetering Conf., Los Angeles, Calif., Oct. 1972, pp. 539-552.

16. Rey, R. D., "Symbol Synchronizer Study for Shuttle Communications," Contract No. NAS 9-13467, Axiomatix Corp., Marina del Rey, Calif., prepared for Lyndon B. Johnson Space Center, Houston, Texas, October 10, 1973.

17. Batson, B. H., Cellier, A., Lindsey, W. C., Vang, H., "An All-Digital Manchester Symbol Synchronizer for Space Shuttle," 1974 National Telecommunications Conference Record, pp. 724-733.

18. Heller, J. A., Odenwalder, J. P., and Viterbi, A. J., "Coded Spread Spectrum Digital Transmission System Design Study," Contract No. NAS 9-13733, Linkabit Corp., San Diego, Calif., prepared for Lyndon B. Johnson Space Center, Houston, Texas, May, 1974.

4.0 AVERAGE ERROR PROBABILITY PERFORMANCE OF CONVOLUTIONALLY CODED SYSTEMS IN THE PRESENCE OF IMPERFECT SYMBOL SYNC

4.1 Introduction

Digital communication systems which, by necessity, require symbol synchronization for successful operation, suffer a performance degradation due to the timing jitter associated with the symbol synchronizer. Accurate assessment of this degradation is essential in predicting overall end-to-end system bit error rate performance.

Regardless of whether the system is coded or uncoded, proper design of the symbol synchronizer loop plays an important role in reducing the degradation to a minimum. For a given symbol signal-to-noise ratio, R_s, symbol rate $\mathcal{R}_s = 1/T_s$, and loop bandwidth W_L, it is desirable to select a configuration which yields minimum mean-squared timing jitter and is commensurate with the requirements on implementation complexity. Several such configurations for Manchester coded symbols were described in the previous section.

When the system is uncoded, it is sufficient to know the probability density function, $p(\lambda)$, of the normalized timing error λ in order to analytically evaluate the error probability performance degradation due to a noisy symbol sync reference. In particular, assuming that the timing error is essentially constant over the symbol duration T_s, then the bit error probability P_b is given by

$$P_b = \int_{-\frac{1}{2}}^{\frac{1}{2}} P_E(\lambda) p(\lambda) d\lambda \qquad (1)$$

where

$$P_E(\lambda) = \tfrac{1}{2} p_t \operatorname{erfc}\left[\sqrt{R_s}(1-2|\lambda|)\right] + \tfrac{1}{2}(1-p_t)\operatorname{erfc}\left[\sqrt{R_s}(1-4|\lambda|)\right] \qquad (2)$$

and p_t is again the symbol transition density.

For convolutionally coded systems, the effect of imperfect symbol sync on bit error probability performance is, in general, more difficult to evaluate analytically and, indeed, in many cases must be determined by either simulation methods or hardware measurements. Fortunately, however, for the Shuttle S-band relay links, suitable assumptions regarding the behavior of the system can be invoked and an approximate analytical evaluation is possible. In the next part of this section, we describe such a technique and present numerical results for the Viterbi decoded K=7 rate 1/3 Shuttle code.

4.2 An Analytical Evaluation of Performance Degradation due to a Noisy Symbol Sync Reference

Generally speaking, the presence of a timing error in the symbol synchronizer causes a reduction in the signal-to-noise ratio available per symbol at the Viterbi decoder input. If the loop bandwidth is large relative to the symbol rate, so that the timing error process varies rapidly over the duration of a single symbol, then the degradation in average symbol signal-to-noise ratio is a good measure for estimating bit error rate degradation in Viterbi decoding. Unfortunately, in most practical convolutionally coded systems, the loop bandwidth of the symbol synchronizer is considerably narrower (perhaps by several order of magnitude) than the symbol rate, and thus a more direct approach, namely direct computation of the bit error rate, is required.

If we examine the symbol synchronizer configurations previously discussed, we observe that the output of the in-phase arm integrate-and-dump when passed through a soft quantizer produces the soft decisions required at the Viterbi decoder input.

For simplicity of presentation, we shall assume an infinite bit quantizer and, thus, the integrate and dump output is fed directly into the Viterbi decoder. Using previously defined terminology the integrate-and-dump output $z(t)$ at time $kT_s+\hat{\epsilon}$ is given by

$$z_k \triangleq z(kT_s+\hat{\epsilon}) = \frac{1}{T_s}\int_{(k-1)T_s+\hat{\epsilon}}^{kT+\hat{\epsilon}} y(t)p_s[t-(k-1)T-\hat{\epsilon}]dt$$

$$= \begin{cases} \sqrt{S}[a_k(1-3|\lambda|)-a_{k+1}|\lambda|] + n_k; & \lambda > 0 \\ \sqrt{S}[a_k(1-3|\lambda|)-a_{k-1}|\lambda|] + n_k; & \lambda \le 0 \end{cases} \qquad (3)$$

where

$$n_k \triangleq \frac{1}{T_s}\int_{(k-1)T_s+\hat{\epsilon}}^{kT_s+\hat{\epsilon}} n(t)p_s[t-(k-1)T-\hat{\epsilon}]\,dt \qquad (4)$$

and

$$E\{n_k\} = 0; \quad \sigma^2 \triangleq E\{n_k^2\} = \frac{N_0}{2T_s} \qquad (5)$$

Letting $k = \ell\nu+m$ ($1/\nu$ is the code rate), then a_k specifically represents the m^{th} ($m = 1, 2, \ldots \nu$) encoder output symbol corresponding to transmission of the ℓ^{th} information bit.

The Viterbi decoder, being a maximum-likelihood decoder, computes the test statistic (metric)

$$q = \sum_{k=1}^{L\nu} z_k a_k = \sum_{\ell=1}^{L}\left[\sum_{m=1}^{\nu} z_{\ell\nu+m}a_{\ell\nu+m}\right] \qquad (6)$$

for all possible sequences of encoder output symbols corresponding to the transmission of L information bits and chooses the input message that yields the largest value of q. The brackets in (6)

indicate that the computation of q is done one tree branch at a time as one sequentially steps through the L branches of the tree. By choosing the value of L to be several times the constraint length of the code, the selected path through the tree can be used to decode the first bit in the sequence of L.

Using the decoding metric of Eq. (6), a tight upper (union) bound to the average bit error probability is (Refs. 1, 2)

$$P_b \leq \sum_{j=d_{min}}^{\infty} n_j m_j P_j \tag{7}$$

where P_j denotes the probability of error in comparing the correct path to an incorrect one which differs in j symbols from it, d_{min} is the minimum free distance of the code, m_j is the number of paths at distance j (differ in j symbols from the correct path) and n_j is the number of bits each of these paths differs from the bit sequence corresponding to the correct path. In the absence of symbol sync error, P_j is given by

$$P_j = \tfrac{1}{2} \operatorname{erfc} \sqrt{jR_s} \tag{8}$$

for each of the m_j paths at distance j. When symbol sync timing error is present, the specific location of the j symbols which are in error along the incorrect path at distance j also affects the calculation of P_j. Thus, P_j is, in general, different for each of the m_j different incorrect paths at distance j. To see this, let $\{a_k^{(i)}\}_j$, $k = 1, 2, \ldots, L$, $i = 1, 2, \ldots, m_j$ denote the sequence of symbols along the i^{th} incorrect path at distance j. Such an incorrect path will be chosen if and only if its metric is larger than that of the correct path, i.e.

$$\sum_{k=1}^{L\nu} z_k a_k'^{(i)} > \sum_{k=1}^{L\nu} z_k a_k \tag{9}$$

or

$$\sum_{k=1}^{L\nu} z_k (a_k'^{(i)} - a_k) \geq 0 \tag{10}$$

Let $S_i(j)$ further denote the set of locations where $a_k'^{(i)} \neq a_k$. Clearly $S_i(j)$ contains j elements. Thus, from (10), we get that the i^{th} incorrect path will be chosen if

$$-2 \sum_{k \epsilon S_i(j)} z_k a_k > 0 \tag{11}$$

or equivalently,

$$\sum_{k \epsilon S_i(j)} z_k a_k < 0 \tag{12}$$

Substituting (3) into (12), we find that the probability of selecting the i^{th} incorrect path at distance j from the correct path is

$$P_j(i) = \Pr\left\{ \sqrt{S} \sum_{k \epsilon S_i(j)} \left[1 - 3|\lambda| - a_k a_{k\pm1} |\lambda|\right] < \sum_{k \epsilon S_i(j)} n_k a_k \right\} \tag{13}$$

where the $\pm$ is determined by the sign of λ in accordance with (3). Since, from (5) the random variable $\sum_{k \epsilon S_i(j)} n_k a_k$ is Gaussian with zero mean and variance $jN_0/2T$, we get that

$$P_j(i) = \tfrac{1}{2} \operatorname{erfc}\left[\sqrt{jR_s} \, \frac{\sum_{k \epsilon S_i(j)} \left[1 - 3|\lambda| - a_k a_{k\pm1} |\lambda|\right]}{j} \right] \tag{14}$$

Finally, then, for a given value of normalized timing error λ, the upper bound on bit error probability analogous to Eq. (7) is

$$P_b(\lambda) \leq \sum_{j=d_{min}}^{\infty} n_j \sum_{i=1}^{m_j} P_j(i) \tag{15}$$

The summation in (14) is upper and lower bounded by

$$j(1-2|\lambda|) \leq \sum_{k\epsilon S_i(j)} [1-3|\lambda|-a_k a_{k\pm1}|\lambda|] \leq j(1-4|\lambda|) \tag{16}$$

and for reasonably large j is well approximated by

$$\sum_{k\epsilon S_i(j)} [1-3|\lambda|-a_k a_{k\pm1}|\lambda|] \cong j[1-3|\lambda|-|\lambda|(1-p_t)+|\lambda|p_t]$$
$$= j[1-4|\lambda|+2|\lambda|p_t] \tag{17}$$

with the approximation improving as j increases. Since in computing the upper bound in (15), the minimum value of j is d_{min}, and since $d_{min} = 14$ for the K=7, ν=3 Shuttle code (Ref. 3), we shall use (17) in (14). When this is done $P_j(i)$ becomes independent of i and (15) simplifies to

$$P_b(\lambda) \leq \sum_{j=d_{min}}^{\infty} n_j m_j (\tfrac{1}{2}\,\mathrm{erfc}\{\sqrt{jR_s}[1-4|\lambda|+2|\lambda|p_t]\}) \tag{18}$$

which is identical to (7) (after substitution of (8)) except that $\sqrt{R_s}$ is replaced by $\sqrt{R_s}(1-4|\lambda|+2|\lambda|p_t)$. The average bit error probability P_b is then upper bounded by

$$P_b \leq \int_{-\frac{1}{2}}^{\frac{1}{2}} \sum_{j=d_{min}}^{\infty} n_j m_j \tfrac{1}{2}\,\mathrm{erfc}\{\sqrt{jR_s}[1-4|\lambda|+2|\lambda|p_t]\}p(\lambda)d\lambda \tag{19}$$

Since the union bound of (7) is very tight over a relatively wide range of bit signal-to-noise ratios $R_b = \nu R_s$ at low decoding error

rates, the polynomial curve fit to the simulation results may be used in place of $P_b(\lambda)$ of (18) by making in it the substitution $\sqrt{R_b}\,(1-4|\lambda| + 2|\lambda|p_t)$ for $\sqrt{R_b}$. Finally, then,

$$P_b \cong \int_{-\frac{1}{2}}^{\frac{1}{2}} P_b'(\lambda)p(\lambda)d\lambda \tag{20}$$

where

$$\log_{10} P_b'(\lambda) = -.1206(10 \log_{10} R_b'(\lambda))^2 - .50(10\log_{10}R_b'(\lambda)) - 1.0706 \tag{21}$$

and

$$R_b'(\lambda) \triangleq R_b(1-4|\lambda| + 2|\lambda|p_t)^2 \tag{22}$$

Using the symbol synchronizer configuration in Fig. 3-5a, Figs. 4-1 to 4-5 illustrate P_b, as determined by the numerical integration of (20), vs R_b for $p_t = .5$, $\xi = .25$, and values of normalized clock frequency offset $\Delta f/B_L = 0, .02, .04, .06,$ and $.08$. The ratio of symbol rate to loop bandwidth is a parameter on each of these curves. The limiting curves for $\delta \to \infty$ are determined from (21) with the substitution $\lambda = \Delta f/4B_L$. For all practical purposes, this limiting performance is obtained with a δ of 2000. Figs. 4-6 and 4-7 illustrate the bit error probability performance for other values of transition density and no clock frequency offset.

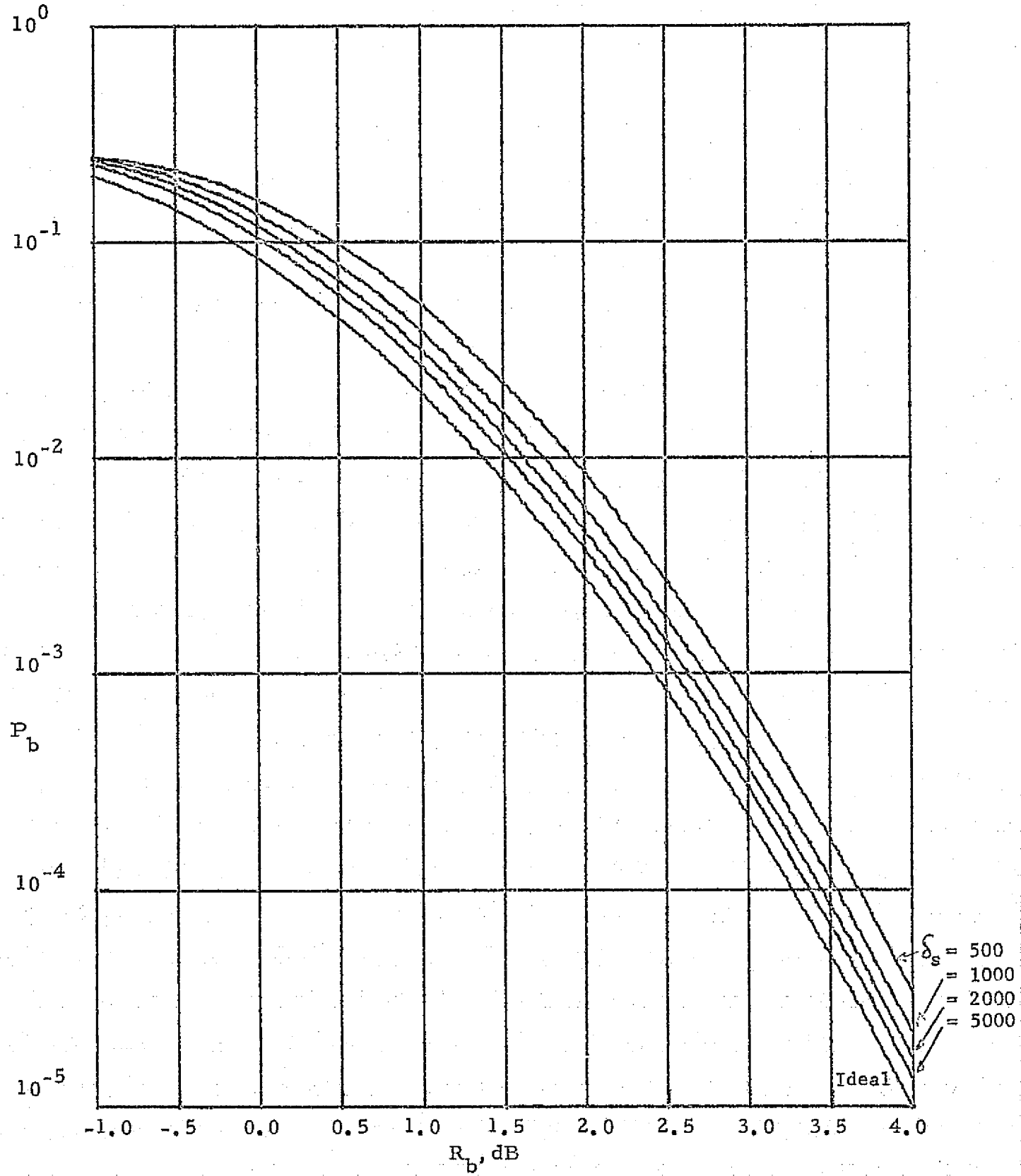

Fig.4-1. Bit Error Probability Performance for K=7, Rate 1/3 Shuttle Code in the Presence of Noisy Symbol Sync: $\xi = .25$, $p_t = .5$, $\Delta f/B_L = 0$.

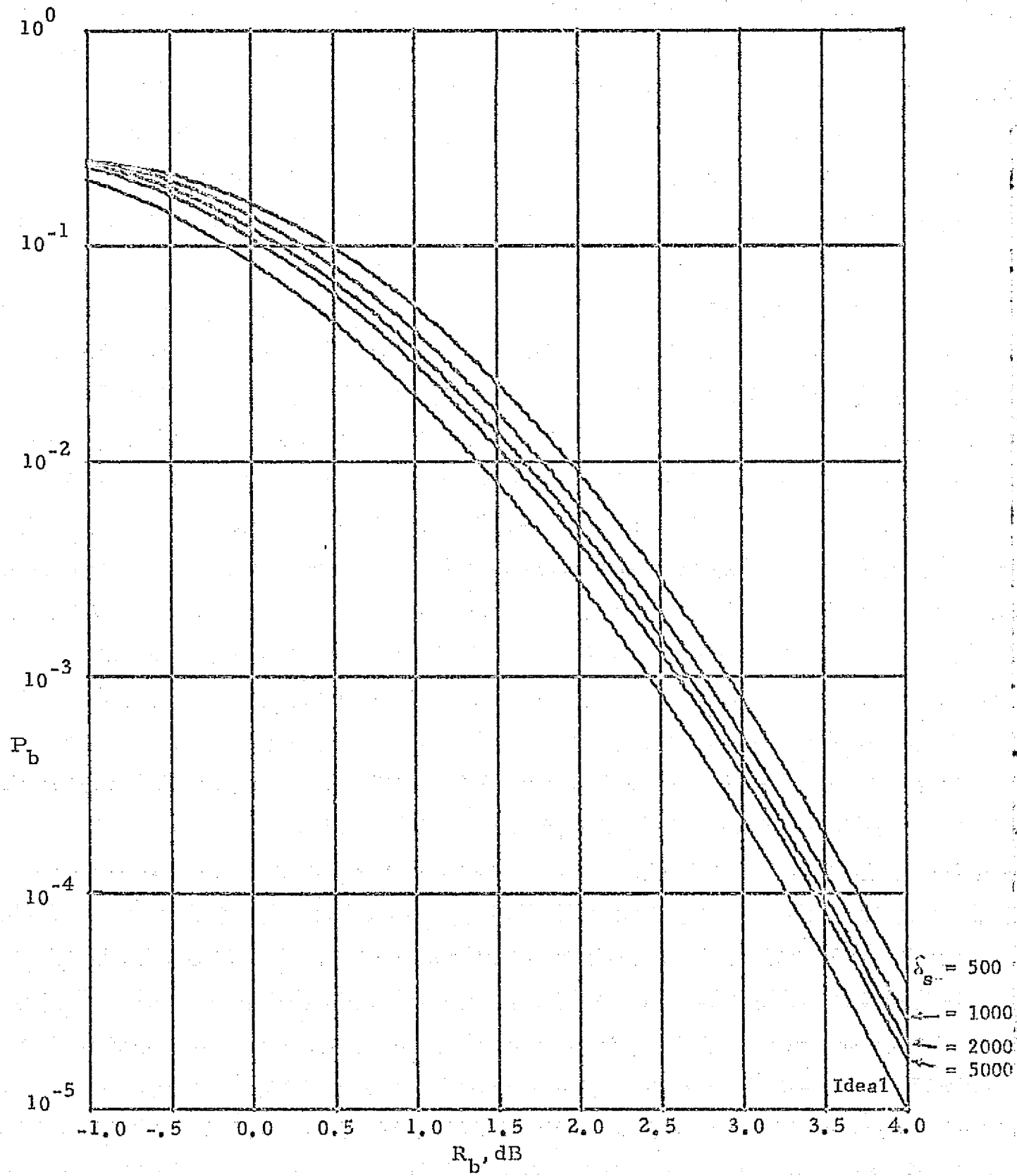

Fig. 4-2. Bit Error Probability Performance of K=7, Rate 1/3 Shuttle Code in the Presence of Noisy Symbol Sync; ζ = .25, p_t = .5, $\Delta f/B_L$ = .02.

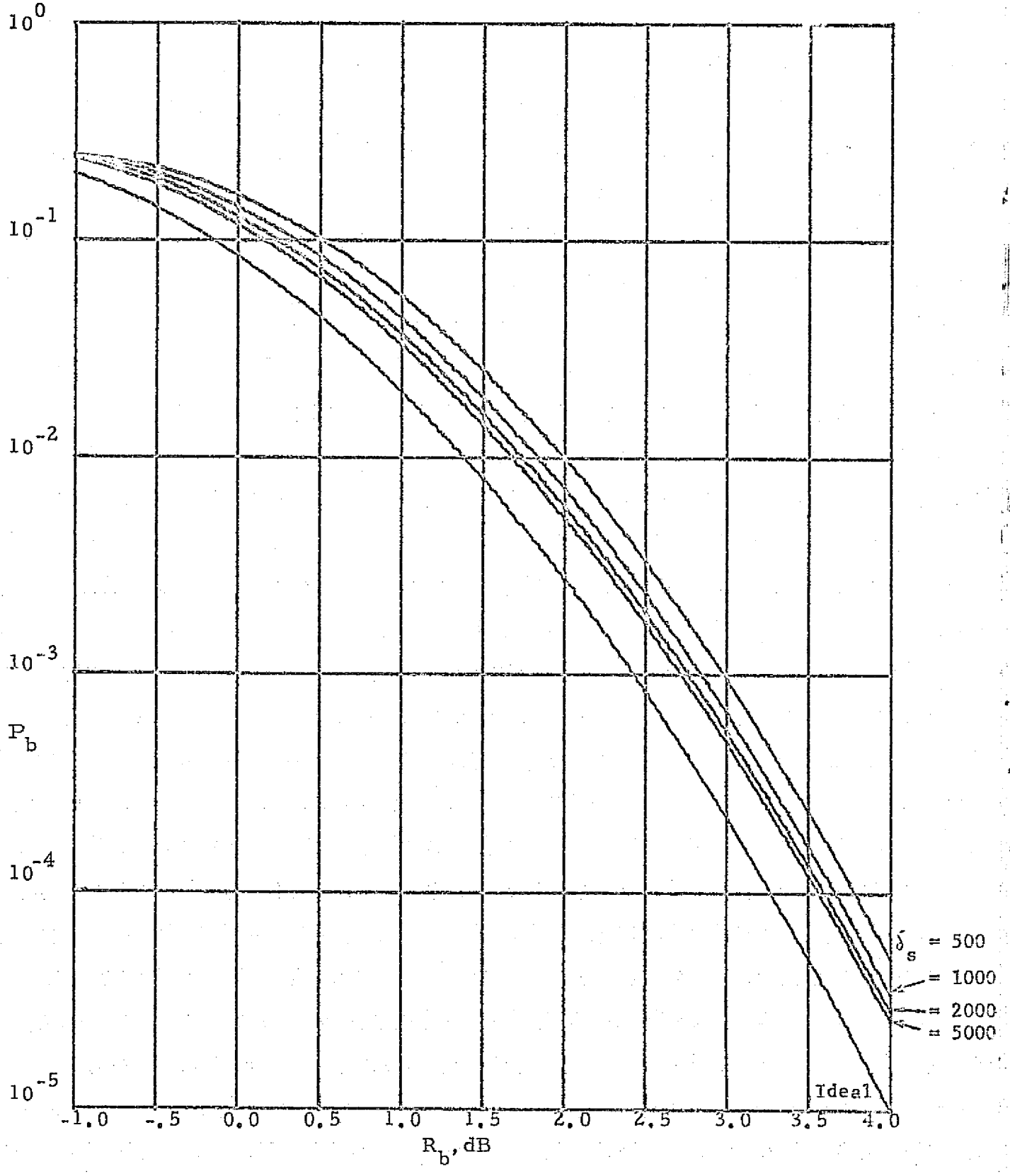

Fig. 4-3. Bit Error Probability Performance of K=7, Rate 1/3 Shuttle Code in the Presence of Noisy Symbol Sync; ζ = .25, P_t = .5, $\Delta f/B_L$ = .04.

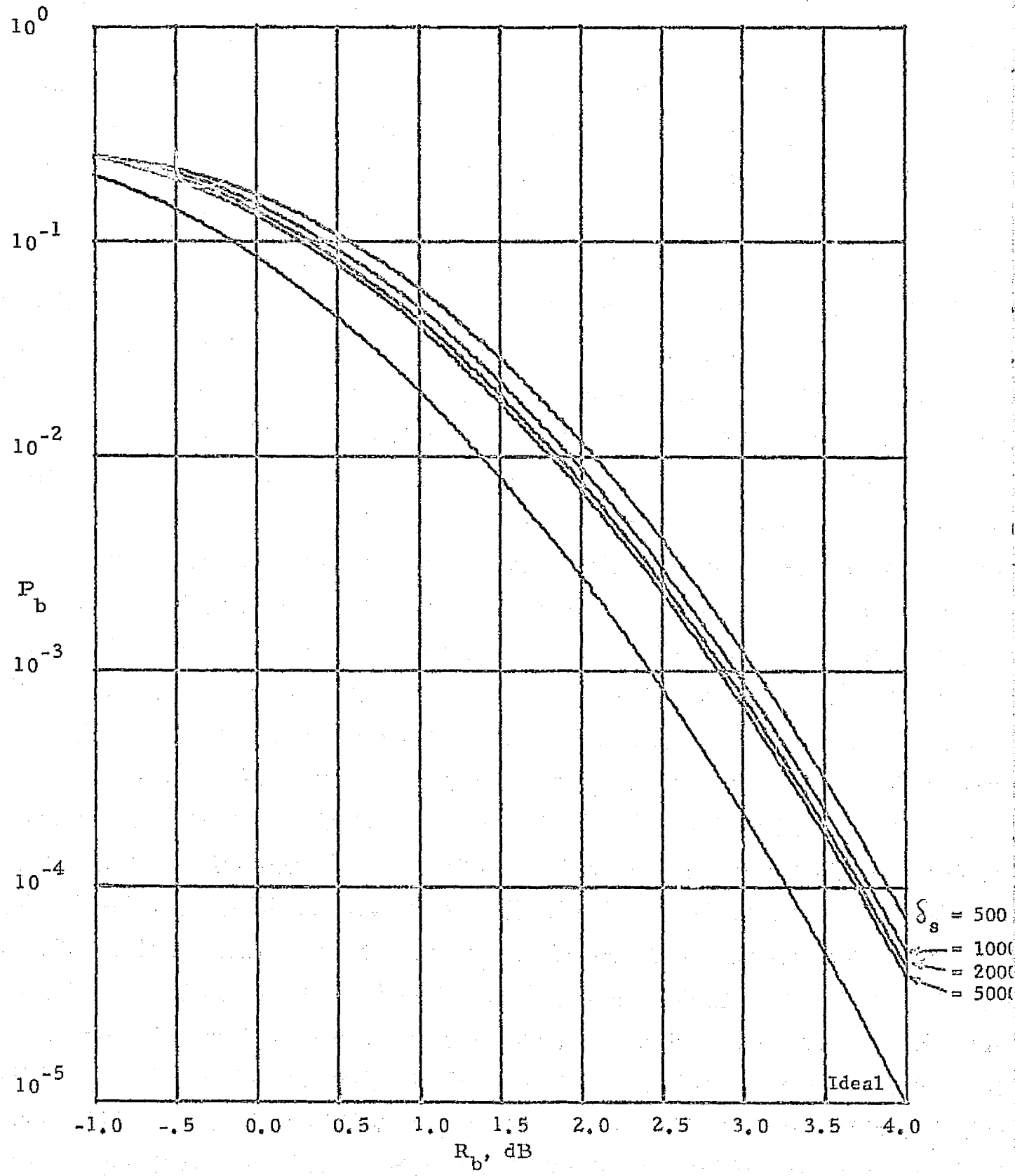

Fig. 4-4. Bit Error Probability Performance of K=7, Rate 1/3 Shuttle Code in the Presence of Noisy Symbol Sync; ζ = .25, p_t = .5, $\Delta f/B_L$ = .06.

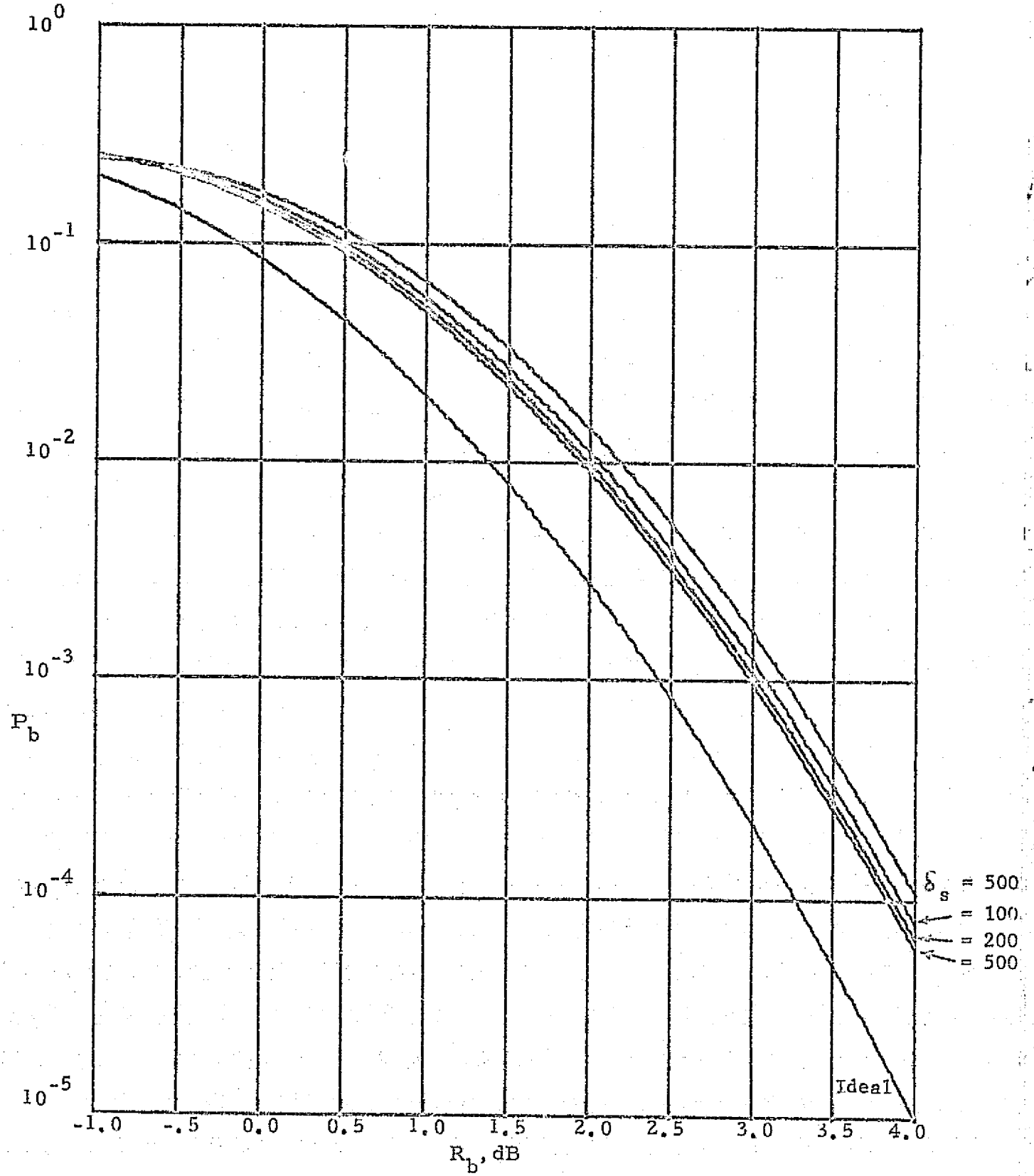

Fig. 4-5. Bit Error Probability Performance of K=7, Rate 1/3 Shuttle Code in the Presence of Noisy Symbol Sync; ζ = .25, p_t = .5, $\Delta f/B_L$ = .08.

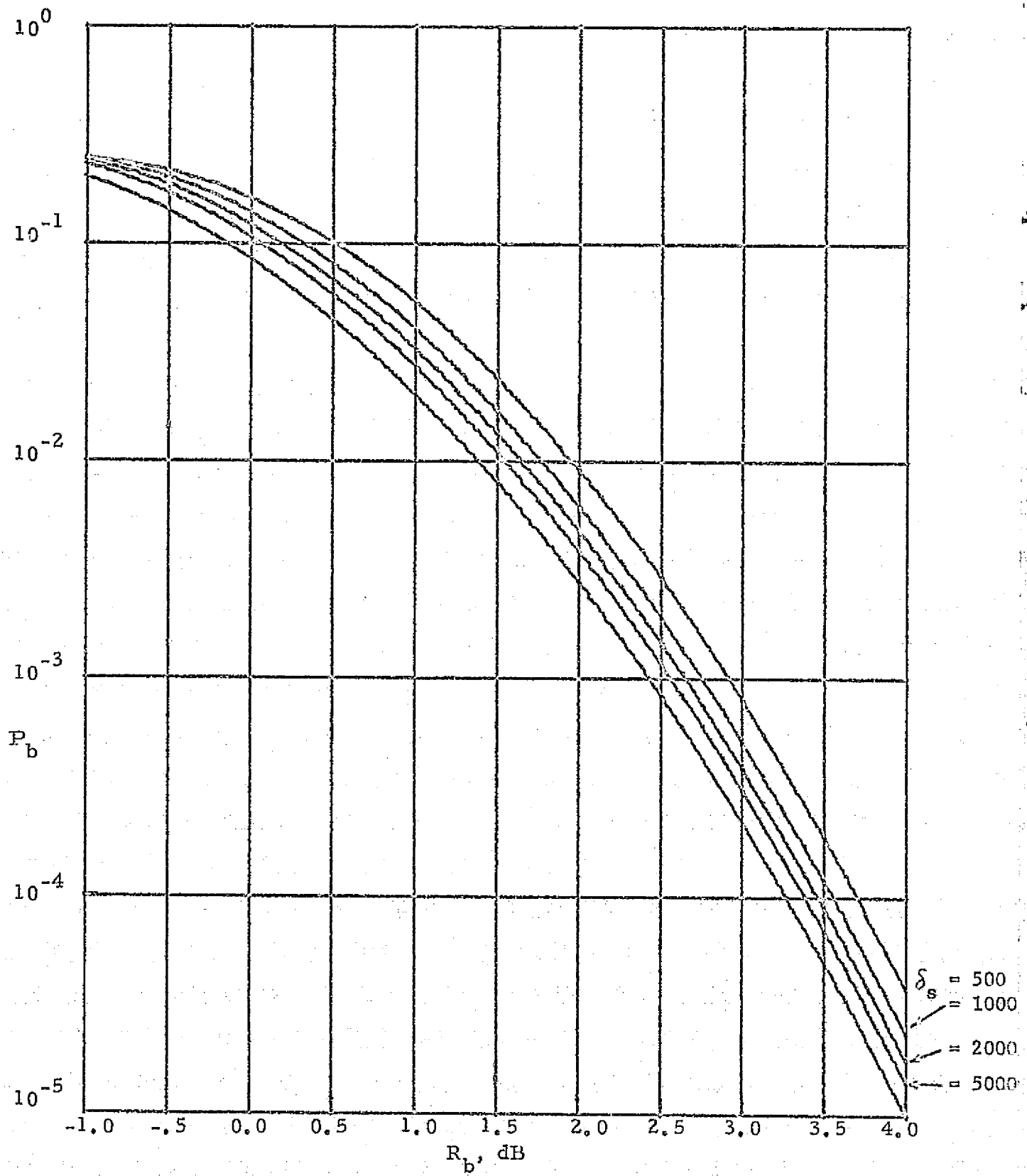

Fig. 4-6. Bit Error Probability Performance of K=7, Rate 1/3 Shuttle Code in the Presence of Noisy Symbol Sync; ζ = .25, p_t = .1, $\Delta f/B_L$ = 0.

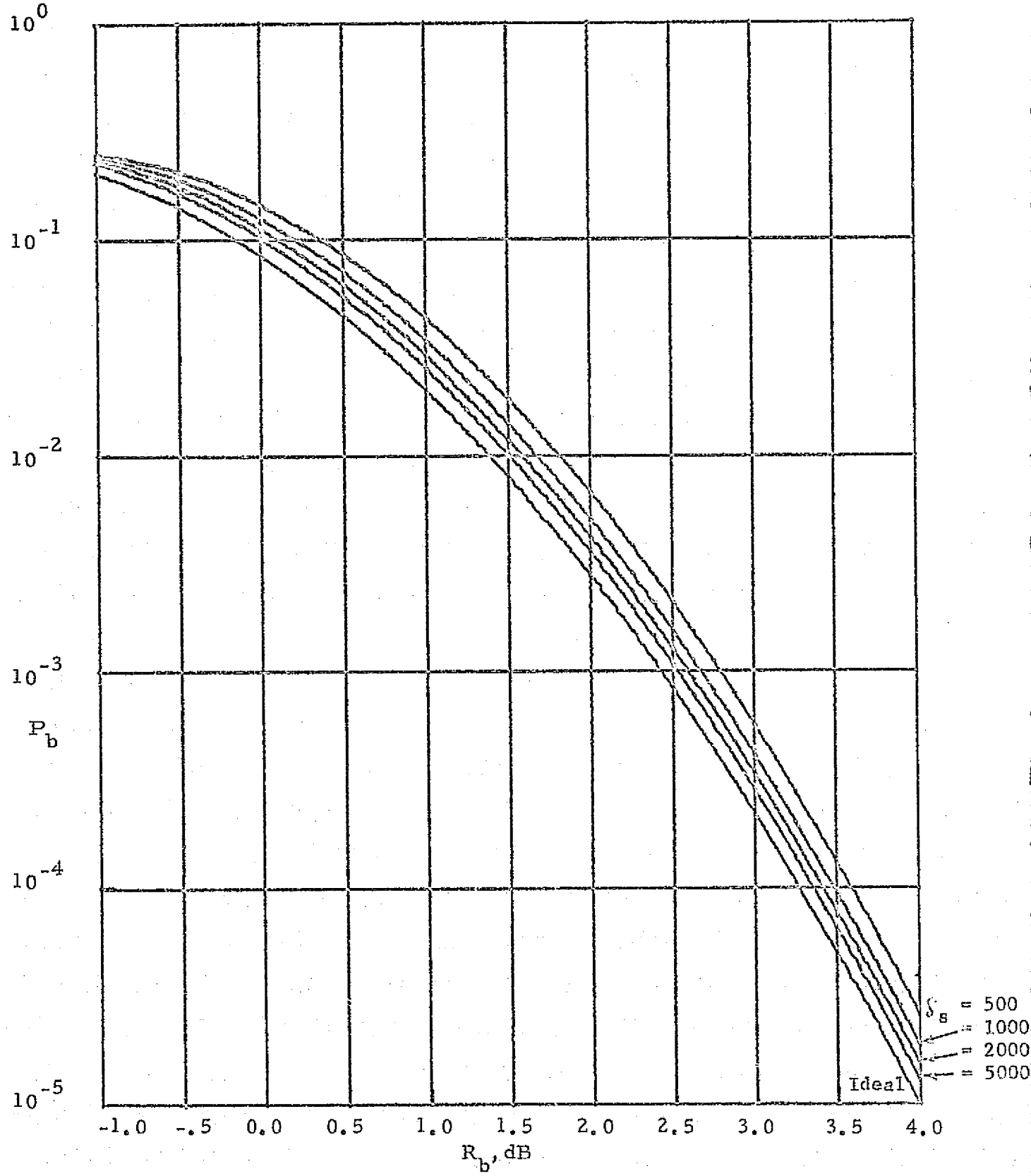

Fig. 4-7. Bit Error Probability Performance of K=7, Rate 1/3 Shuttle Code in the Presence of Noisy Symbol Sync; $\zeta = .25$ $\eta_t = .9$, $\Delta f/B_L = 0$.

References for Section 4.0

1. Viterbi, A. J., "Convolutional Codes and their Performance in Communication Systems," IEEE Transactions on Communication Technology (Special Issue on Error Correcting Codes), Vol. COM-19, No. 5 (October, 1971), pp. 751-722.

2. Lindsey, W. C., and Simon, M. K., Telecommunication Systems Engineering, Prentice-Hall, Inc., Englewood Cliffs, N. J., 1973.

3. Odenwalder, J. P., "Optimal Decoding of Convolutional Codes," Doctoral Dissertation, University of California at Los Angeles, 1970.